2014

A Systematic Transport and Thermodynamic Study of Heavy Transition Metal Oxides with Hexagonal Structure

Kamal H. Butrouna
University of Kentucky, kamal.but@uky.edu

Recommended Citation

Butrouna, Kamal H., "A Systematic Transport and Thermodynamic Study of Heavy Transition Metal Oxides with Hexagonal Structure" (2014). *Theses and Dissertations--Physics and Astronomy*. 24.
https://uknowledge.uky.edu/physastron_etds/24

STUDENT AGREEMENT:

I represent that my thesis or dissertation and abstract are my original work. Proper attribution has been given to all outside sources. I understand that I am solely responsible for obtaining any needed copyright permissions. I have obtained needed written permission statement(s) from the owner(s) of each third-party copyrighted matter to be included in my work, allowing electronic distribution (if such use is not permitted by the fair use doctrine) which will be submitted to UKnowledge as Additional File.

I hereby grant to The University of Kentucky and its agents the irrevocable, non-exclusive, and royalty-free license to archive and make accessible my work in whole or in part in all forms of media, now or hereafter known. I agree that the document mentioned above may be made available immediately for worldwide access unless an embargo applies.

I retain all other ownership rights to the copyright of my work. I also retain the right to use in future works (such as articles or books) all or part of my work. I understand that I am free to register the copyright to my work.

REVIEW, APPROVAL AND ACCEPTANCE

The document mentioned above has been reviewed and accepted by the student's advisor, on behalf of the advisory committee, and by the Director of Graduate Studies (DGS), on behalf of the program; we verify that this is the final, approved version of the student's thesis including all changes required by the advisory committee. The undersigned agree to abide by the statements above.

Kamal H. Butrouna, Student

Dr. Gang Cao, Major Professor

Dr. Tim Gorringe, Director of Graduate Studies

2014

A Systematic Transport and Thermodynamic Study of Heavy Transition Metal Oxides with Hexagonal Structure

Kamal H. Butrouna
University of Kentucky, kamal.but@uky.edu

Recommended Citation

Butrouna, Kamal H., "A Systematic Transport and Thermodynamic Study of Heavy Transition Metal Oxides with Hexagonal Structure" (2014). *Theses and Dissertations--Physics and Astronomy.* Paper 24.
http://uknowledge.uky.edu/physastron_etds/24

STUDENT AGREEMENT:

I represent that my thesis or dissertation and abstract are my original work. Proper attribution has been given to all outside sources. I understand that I am solely responsible for obtaining any needed copyright permissions. I have obtained and attached hereto needed written permission statement(s) from the owner(s) of each third-party copyrighted matter to be included in my work, allowing electronic distribution (if such use is not permitted by the fair use doctrine).

I hereby grant to The University of Kentucky and its agents the irrevocable, non-exclusive, and royalty-free license to archive and make accessible my work in whole or in part in all forms of media, now or hereafter known. I agree that the document mentioned above may be made available immediately for worldwide access unless a preapproved embargo applies. I retain all other ownership rights to the copyright of my work. I also retain the right to use in future works (such as articles or books) all or part of my work. I understand that I am free to register the copyright to my work.

REVIEW, APPROVAL AND ACCEPTANCE

The document mentioned above has been reviewed and accepted by the student's advisor, on behalf of the advisory committee, and by the Director of Graduate Studies (DGS), on behalf of the program; we verify that this is the final, approved version of the student's dissertation including all changes required by the advisory committee. The undersigned agree to abide by the statements above.

Kamal H. Butrouna, Student

Dr. Gang Cao, Major Professor

Dr. Tim Gorringe, Director of Graduate Studies

A Systematic Transport and Thermodynamic Study of Heavy Transition Metal Oxides with Hexagonal Structure

---

DISSERTATION

A dissertation submitted in partial
fulfillment of the requirements for
the degree of Doctor of Philosophy
in the College of Arts and Sciences
at the University of Kentucky

By
Kamal Butrouna
Lexington, Kentucky

Co-Directors: Dr. Gang Cao, Professor of Physics
and Dr. Lance DeLong, Professor of Physics
Lexington, Kentucky 2014

ABSTRACT OF DISSERTATION

A Systematic Transport and Thermodynamic Study of Heavy Transition Metal Oxides with Hexagonal Structure

There is no apparent, dominant interaction in heavy transition metal oxides (TMO), especially in 5d-TMO, where all relevant interactions are of comparable energy scales, and therefore strongly compete. In particular, the spin-orbit interaction (SOI) strongly competes with the electron-lattice and on-site Coulomb interaction (U). Therefore, any tool that allows one to tune the relative strengths of SOI and U is expected to offer an opportunity for the discovery and study of novel materials. $BaIrO_3$ is a magnetic insulator driven by SOI, whereas the isostructural $BaRuO_3$ is a paramagnetic metal. The contrasting ground states have been shown to result from the critical role of SOI in the iridate. This dissertation thoroughly examines a wide array of newly observed novel phenomena induced by adjusting the relative strengths of SOI and U via a systematic chemical substitution of the $\mathrm{Ru}^{4+}(4d^4)$ ions for $\mathrm{Ir}^{4+}(5d^5)$ ions in $BaIrO_3$, *i.e.*, in high quality single crystals of $BaIr_{1-x}Ru_xO_3(0.0 \leq x \leq 1.0)$. Our investigation of structural, magnetic, transport and thermal properties reveals that Ru substitution directly rebalances the competing energies so profoundly that it generates a rich phase diagram for $BaIr_{1-x}Ru_xO_3$ featuring two major effects: (1) Light Ru doping $(0 \leq x \leq 0.15)$ prompts a simultaneous and precipitous drop in both the magnetic ordering temperature T_C and the electrical resistivity, which exhibits metal-insulator transition at around T_C. (2) Heavier Ru doping $(0.41 \leq x \leq 0.82)$ induces a robust metallic and spin frustration state. For comparison and contrast, we also substituted $\mathrm{Rh}^{4+}(4d^5)$ ions for $\mathrm{Ir}^{4+}(5d^5)$ ions in $BaIrO_3$, *i.e.* in $BaIr_{1-x}Rh_xO_3(0.0 \leq x \leq 0.1)$, where Rh only reduces the SOI, but without altering the band filling. Hence, this system remains tuned at the Mott instability and is very susceptible to disorder scattering which gives rise to Anderson localization.

KEYWORDS: spin-orbit interaction, heavy transition metal oxides, barium iridate, metal-insulator transition, magnetic order

Author's signature: Kamal Butrouna

Date: July 23, 2014

A Systematic Transport and Thermodynamic Study of Heavy Transition Metal Oxides with Hexagonal Structure

By
Kamal Butrouna

Gang Cao
Co-Director of Dissertation

Lance DeLong
Co-Director of Dissertation

Tim Gorringe
Director of Graduate Studies

July 23, 2014

Dedicated to the soul of my father
Mr. Hassouna Butrouna
Allah's mercy

ACKNOWLEDGMENTS

At this moment of this accomplishment, it is a pleasure and great honor to acknowledge all the parties helped and supported me to achieve this moment. First, I acknowledge my home Libya for the generous support through my scholarship for the first five years. For my family and me, it was uneasy challenge to pursue my study here and watch what was happening there within the last three years. Also, I would like to extend my heartfelt gratitude to my family there especially, my mother, and brothers and sisters, for their endless love and emotional support during this time.

Secondly, I would like to express my thanks and appreciation to my advisor Dr. Gang Cao for his help and patience, and his professional guidance along all the phases of my learning process. Also thanks to all the professors and colleagues in the Department of Physics and Astronomy, University of Kentucky. Very special gratitude and thanks to Dr. Shujuan Yuan for her consultations and the great help through the preparation of this thesis. Any work becomes more enjoyable with nice colleagues to work with, so special greeting to all friends in Dr. Cao's group in the past and present, special thanks go to Dr. Oleksander Korneta and Dr. Tongfei Qi for the great help through different phases during my work in this group, thanks also to Dr. Li Li and Ms. Jasminka Terzic for the friendship and help. In addition, I want to thank the Graduate School of the University of Kentucky and the Huffaker Family fund for a number of travel grants I have received for academic travelling. I also want to thank my advisory committee members for their understanding and support.

Then, I would like to express my acknowledgement to my friend Dr. Mohamed El-Habbak for his help and support. Thanks to my friend Dr. Amer lahmer who passed away a few months before this work ends. Thanks to my teacher Mrs. Deanton for reviewing my English writting and many other noble things, thanks also to the staff in the writing center of University of Kentucky.

Finally, I want to acknowledge my companions in this journey, my wife Malak and my son Mohammed, for their sacrifice and endure patient along this accomplishment, and also for the endless love and encouragement.

TABLE OF CONTENTS

LIST OF FIGURES

LIST OF TABLES

Chapter 1 INTRODUCTION

Research and discovery in transition metals and transition metal oxides have long history. It goes back to the early centuries with observations on the fundamental features of reflectivity and magnetism. The recent discoveries in transition metal oxide materials, such as high temperature superconductivity, giant magneto-resistance, energy storage materials, and lately, topological insulators, are advanced steps on this journey.

1.1 Transition Metal Oxides (TMOs)

Transition metal oxides (TMOs) are compounds based on transition metals. These transition metals are located in the d-block of the periodic table and include the series of 3d, 4d, and 5d of these metals, as shown in Figure (1.1). The transition metals share the common trait that the most outer shell of the electronic configuration consists of d-orbitals. The boundaries of the series of transition metals vary in different definitions [1]. In the definition of the International Union of Pure and Applied Chemistry (IUPAC), the transition metals are elements whose atoms have incomplete d sub-shells or which can give rise to cations with incomplete d sub-shells [2]. The transition metals are mostly hard, have high melting and boiling points, conduct heat and electricity, and can form with other elements different alloys and compounds. Because of the progressive filling of the d-orbitals through the three different periods, $3d$, $4d$, and $5d$, different transition metals have different d-orbital configurations. The d-electrons of some transition elements can adopt different d-orbital configurations giving rise to different oxidation states for such elements. For example, ruthenium (Ru) has (3+, 4+, and 5+) as oxidation states for $((Ru^{3+})4d^5, (Ru^{4+})4d^4, and\ (Ru^{5+})4d^3)$, respectively.

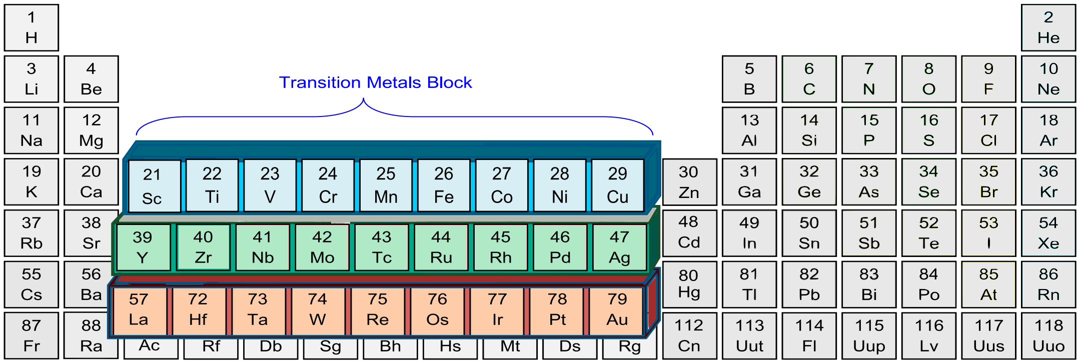

Figure 1.1: Transition metals block in the periodic table

The d-electrons within the d-orbital configurations interact with the other d-electrons in a metal. These d-electrons could be of their own configuration or other configurations of different oxidation states. When these different configurations are from the same ion, they are called mixed oxidation states. The d-electrons also interact with the surrounding electronic and crystalline host of the TMO compounds. The interesting properties and characteristics of TMOs are attributed to such interactions, and also to the interaction of the d-electrons for example with 2p-electrons of the neighboring oxygen [1]. The diverse spectrum of properties and characteristics of TMOs represent uncountable structures and compounds of these materials. These properties and characteristics have inspired and still inspire the thoughts, ideas, imagination, and inquisitiveness of scientists, engineers, and artists. The development of TMO materials represents an important contribution to technology. The big jump in applications and research of TMOs, during the last few decades, has been mostly due to the discovery of the high temperature superconductivity (HTSC) in the 3d cuprates $LaBaCuO$ [3] during the 1980s. This discovery attracted the attention of many scientists, not only physicists, but also researchers from many other disciplines. The attention raised many questions and issues involving the understanding of TMO's properties and behavior. During the past decades, most efforts in research and technology were directed toward 3d TMOs because of HTSC. 4d and 5d TMOs have attracted considerable attention only during the last decade and specifically within the more recent years. TMO materials can be in form of dielectric materials, semiconductors, superconductors, and as materials for magnetic and optical applications. As examples of TMOs, $BaTiO_3$ is a dielectric material (ferroelectric) with PM or DM magnetic response [4], ReO_3 is a PM metal [5], $SrRuO_3$ is FM with metallic state [6]. Possible examples of Weyl semi-metals with strong magnetic instability can be seen in $RE_2Ir_2O_7$ where RE means rare earth element such as Y or Nd [7]. TiO_2 is a wide gap semiconductor [8], and $YBa_2Cu_3O_7$ is HTSC [1]. Some TMOs are volatile compounds like OsO_4 [1].

The physical, magnetic, and transport properties of many TMOs are susceptible for small changes in their structure or environment (perturbation). The metal-nonmetal transition, for example, in some TMOs can be affected by pressure, chemical doping, or temperature. This transition in conductivity, in many cases, is accompanied by a variation of other physical properties, such as magnetism and/or optical properties. The understanding of these different behaviors in these TMOs is a branch of material physics known as strongly correlated electron systems.

1.2 Strongly Correlated Electron Systems (SCES)

In general, the physical properties of materials are related to their structure and constituents that form this structure. An electron in a solid has a mass (m_e) and is bound to a specific atomic site, and can be assigned three attributes: charge (e^-), spin ($s = \frac{1}{2}$), and orbital (ℓ) degrees of freedom. In electronic materials, the charge carriers, electrons or holes, could be localized or free to move or hop. An orbital is simply an electron probability density distribution and can represent the electron cloud distribution in a solid. In addition to the crystal structure environment, interplay and interactions between these degrees of freedom and quantities determine the electronic state of a system and hence, its material's properties.

The term *Strongly Correlated Electron Systems* refers to a physical system such

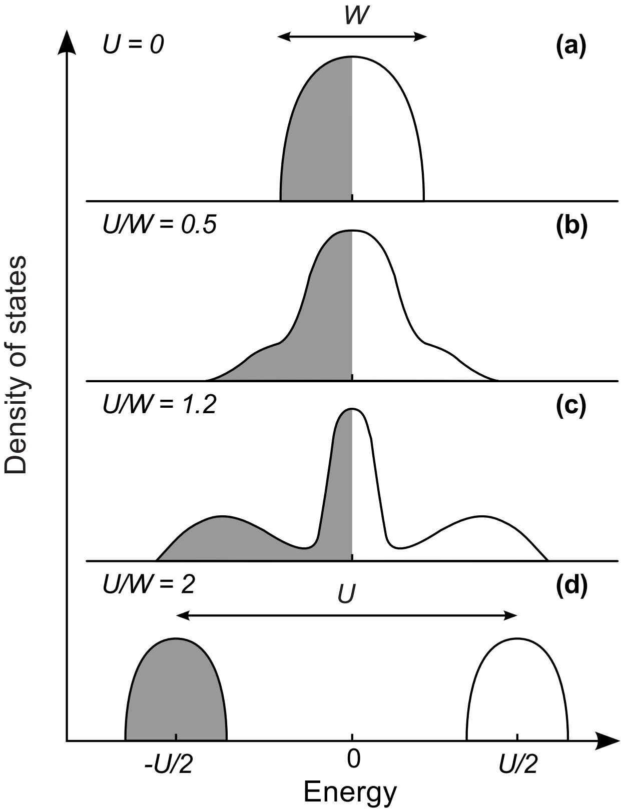

Figure 1.2: Density of states as a function of U/W ratio and band energy for electrons that are: (a) free, (b) nearly free (weakly correlated), (c) strongly correlated, and (d) localized [9]

as a solid, where the electron-electron (e-e) Coulomb repulsion interaction is fairly strong. This strong (e-e) interaction can cause the electrons to be almost localized or immobile [10]. In such case, the (e-e) interaction energy, called U, becomes comparable energy to the electrons' kinetic energy, called band width energy W [11]. The competition between U and W of electrons in atomic or molecular crystal structure is responsible for the realization of free, nearly free, correlated, or localized electrons. Figure (1.2) illustrates different distributions of the local density of states (DOS) as a function of the local Coulomb interaction energy and how the spectral features evolve with different (U/W) ratio. When $U \sim 0$, which is the case for free electrons in good metals, an appreciable overlapping occurs between the orbitals of neighboring atoms in the solid. This overlapping results in a wide band W, reflected in the peak of DOS. If the band is partially filled, Fermi level resides in the middle as shown in figure (1.2a). The other limit is $U >> W$ and describes localized states, which is the case in Mott insulators, (see section 2.5.3). In this case, a gap has opened and DOS peaks at the ionization energies and electron affinity of the atom, as illustrated in figure (1.2d). In SCES, which is an evolution between these two limits, the (e-e) interaction energy U is comparable to the kinetic energy W of electrons. The system behavior is closely related to the ratio of U to the band width W [9]. This is called the correlation phenomenon in SCES, if U < W the behavior would be close to weakly correlated materials as illustrated in figure (1.2b). The case of SCES is when the correlation is comparable to the band width ($U \sim W$), this case is shown in figure (1.2c).

In contrast to free electrons, where the electron charge is the most important attribute, in SCES the delocalized electrons -or nearly free electrons- can be manipulated by the three electron attributes -charge, spin and orbital degrees of freedom. Additionally, in many cases, there is a coupling between any two or all the three of these attributes in describing the physical state of the system. In this case, affecting one of these attributes, for example spin by an external magnetic field, can change the state of another degree of freedom, for example charge ordering, see figure (1.3). The electronic behavior of such systems cannot be described by non-interacting electron theories, because any disturbance to the electrons has a strong effect on the electronic state of the system. Single electron theories, such as Local Density Approximation (LDA), Density Functional Theory (DFT), or Hartree-Fock Theory (HF), need to be extended to account for the electron correlation effect, (e-e) interaction. Some attempts in extending these theories have resulted in a number of proposals, such as (LDA+U) where U refers to (e-e) interaction energy, Self-Interaction-Corrected LDA (SIC-LDA), and the Dynamical Mean Field Theory (DMFT), which has effectively explained many of the strongly correlated electron system behaviors [9].

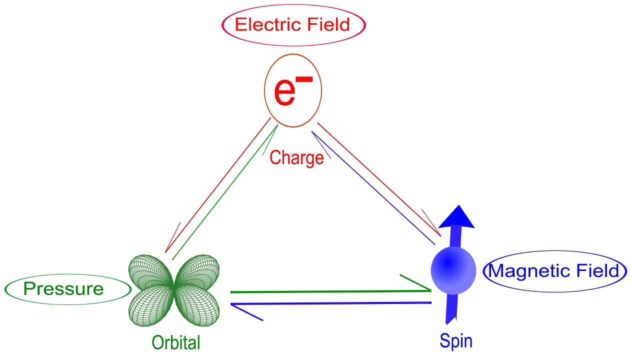

Figure 1.3: The coupling between the charge, spin, and orbital degrees of freedom in correlated system.

In a solid, when the number of covalent electrons is comparable to the number of ions, (e-e) interaction becomes stronger. Many of the TMOs are classified as SCES because the anisotropic shaped d-orbital electrons experience this strong (e-e) interaction [11]. This interaction is a driving force for electron localization. NiO, as a simple TMO example, is expected to be a metallic oxide because of the partially filled 3d-orbitals of

$Ni(3d^8)$. Becuase the Coulomb repulsion,(e-e) interaction, is strong enough, NiO is a wide band-gap insulator [1]. Other common examples of TMOs as SCES systems are HTSC and Mott insulators, Metal-Insulator transition (MIT) materials, and colossal magnetoresistance systems [11]. The subtle coupling between electron, lattice, orbital, and spin degrees of freedom are important interaction mechanisms of SCES of TMOs [1]. For example, the orbital degree of freedom occasionally plays an important role in these phenomena, and its correlation and order-disorder transition cause a variety of phenomena through strong coupling with charge, spin, and lattice dynamics. The electronic correlation can cause striking many-particle effects and observations, such as electronic localization, magnetism, and charge ordering [11]. These interactions could result in the emergence of novel ground state or exotic phase transitions. The interplay of internal degrees of freedom, spin, charge, and orbital momentum of the d-orbital electrons, makes these systems extremely interesting. These systems exhibit a sensitive response to small external perturbations such as temperature, pressure, doping, or electric/magnetic field. In many cases, such response can be a huge change in some property or an unexpected switch to a different state. The interactions are the key point in understanding the ground state of a wide class of TMO materials.

1.3 Interaction Energies in TMOs

The interactions that occur in TMOs are the main concept in understanding many TMOs properties and behavior. In the next chapter, I will talk more about these different interactions. The interactions can be classified into two groups: Fundamental interactions, those interactions that occur within and between transition metal atoms, environmental interactions due to crystalline host structure and neighboring atoms. There is always a crossover between the two categories, and tuning one of them may affect another interaction. As fundamental atomic interactions, we can list the following interactions:

- (e-e) interaction [12]: As defined in section (1.2), this is the Coulomb repulsion interaction between d-orbital electrons. This interaction becomes stronger because of the confined spatial distribution of d-orbitals. In addition, it reflects the Pauli Exclusion Principle, which states that no more than a single electron can occupy any quantum state. The (e-e) interaction is an important theme in understanding a class of TMOs known as Mott insulators. This interaction is a dominant interaction in 3d TMOs but becomes relatively weaker in 4d and 5d TMOs.

- (spin-spin) interactions [13]: These interactions also are referred to as the magnetic interactions. These interactions include direct-exchange, super-exchange, and indirect-exchange interactions. The direct exchange occurs between two magnetic ions; super-exchange occurs between two magnetic ions via nonmagnetic legend such as oxygen. The indirect exchange is the dominant one in metallic compounds and is controlled by itinerant electrons of the magnetic ions. The anisotropic exchange is a cooperation between the relativistic spin-orbit interaction and the super-exchange interaction. These interactions utilize the cooperative collective behavior to serve as the basis for a long range magnetic ordering in magnetic TMOs materials.

- Hund's rules interactions [12]: These are three empirical rules that state the spin favorable configuration of a subshell such as d-orbitals of an atomic electronic configuration. In many cases, these rules are satisfied in the TMOs, but other interaction energies can affect and tune the Hund's rules' validity and strength. These rules are based on the Pauli Exclusion Principle.
- Spin-Orbit interaction (SOI) [13]: This is a relativistic effect that originates due to the orbiting of an electron through the electric/magnetic field of a nucleus. The SOI energy is proportional to the number of nucleus charge, *i.e.*, $\lambda\vec{S}\cdot\vec{L} \propto Z^4$ where Z is the atomic number. Therefore, this interaction initiates a balance energy comparable to the (e-e) interaction in the 5d TMOs.

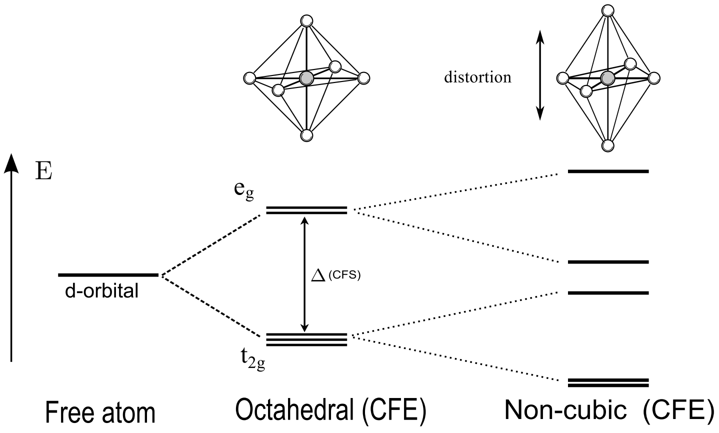

Figure 1.4: Crystal field effect of octahedral arrangement and the non-cubic crystal field (John-Teller) effect due to distortion [14].

The second category is the environmental interactions, and the most common interactions are:

- Crystal Field Effect (CFE) [1]: This effect reflects the interaction between ions and their surrounding neighbors in a crystalline structure. The direct influence of CFE is the degeneracy lifting of the atomic d-orbitals, which results in the formation of two subsets of d-orbitals e_g and t_{2g} (see figure 2.6). These two subsets are separated by a gap known as the *Crystal Field Splitting* Δ. The ideal case of an octahedral arrangement is illustrated in figure (1.4). In addition, there is another less strong effect known as a non-cubic crystal field effect that is responsible for lifting the e_g and t_{2g} degeneracy. This effect in many cases results from different mechanisms, such as mixed valence, some crystal defects or distortion (see figure 1.4), or an external applied pressure. This non-cubic CFE effect is referred to as Jahn-Teller (JT) effect.

- d-p hybridization [15]: This interaction is the overlapping between the transition metal d-orbitals and the surrounding oxygen p-orbitals. In most cases, this interaction tends to delocalize the d-electrons. In some cases, it enhances the localization effect, depending on the nature of the crystal environment and orbitals engaged. Chemically, this interaction serves as a covalent bond in these compounds.
- Thermal excitations: These include the well-known phonon-phonon interactions as well as the phonon-electron interactions that result from the lattice vibrations.

The rebalance, cooperation, and competition between these interactions in many cases reflect the lattice-electronic degrees of freedom coupling in the behavior and properties of TMOs.

1.4 Heavy TMOs

TMOs with composition based on 5d transition metals are referred to as heavy oxides. Iridates are a good example of 5d heavy TMOs. The iridium (Ir) has the atomic number $Z = 77$, and the mass number $A = 192$, which is three times larger than that of copper (Cu), the 3d transition metal. The atomic electronic configuration of iridium is $[Xe]4f^{14}5d^{7}6s^{2}$ and the common oxidation states of its ionic form are $Ir^{4+}(5d^{5})$, $Ir^{5+}(5d^{4})$ and $Ir^{6+}(5d^{3})$. The iridium metal has the FCC crystal structure. TMO Iridates can show a number of different crystal structures; the represented iridate in this work, $BaIrO_3$, has a hexagonal perovskite structure [16]. The archetype strontium iridium oxide Sr_2IrO_4 and other members of the strontium iridium series, $SrIrO_3$ and $Sr_3Ir_2O_7$, also show layered perovskite structures [17] [18] [19]. Sr_4IrO_6 is a different layered structure [20]. Other iridates can possess other different structures such as pyrochlore [21], kagome, or honeycomb structure [22]. The general layered perovskite structure in iridates can be described by the $Ruddlesden - Popper\ Series\ (RP)$ model. This series has the general formula $A_{n+1}B_nO_{3n+1}$ [23], where A and B are two cations, O is the oxygen and n is the number of layers of octahedra within the crystal unit cell. This definition is illustrated in figure (1.5). RP is an effective model in studying the chemical doping in perovskite layered structures. The cations A and B occupy different distinct sites through the crystal structure, and the substitution of A cation prominently affects the c-axis stacking and structure as well as the material's properties along this direction. The substitution of cation B mainly changes the ab-plane structure and properties . Another observation is that most of the real layered perovskite structures in this series experience a structure distortion because of the different sizes and natures of the A and B cations. Such distortion may reflect in the Jahn-Teller (JT) effect. The JT effect is a common phenomenon in heavy TMOs with layered structures. Other iridates that can be described by the RP series include $Sr_{n+1}Ir_nO_{3n+1}, Ca_{n+1}Ir_nO_{3n+1}$ and $Ba_nIr_{n+1}O_{3n+1}$, with n usually having

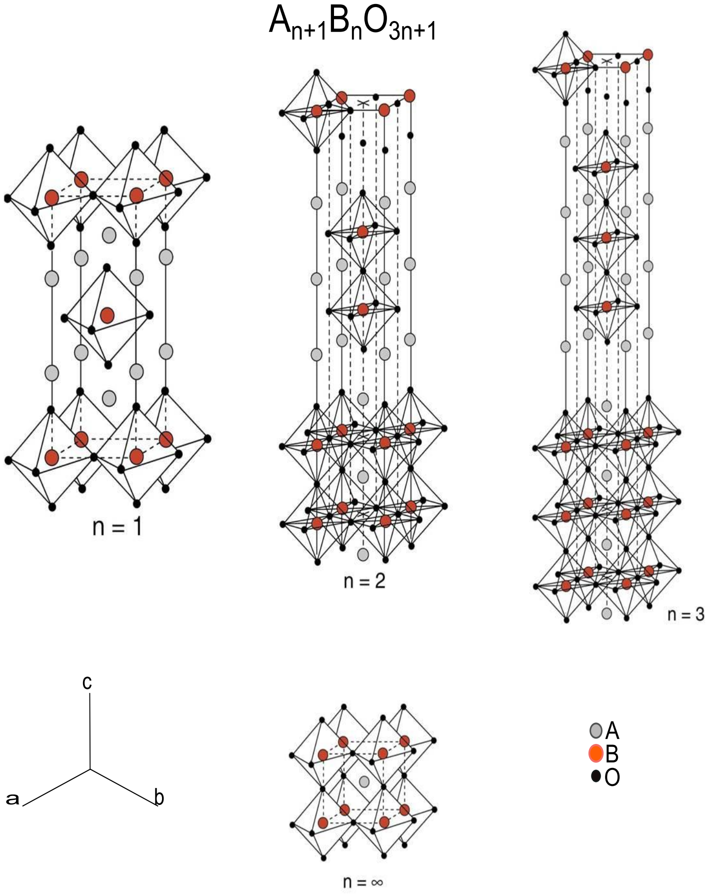

Figure 1.5: Ruddlesden-Popper series of perovskite layered structure [14].

the (1, 2, 3 or ∞) values.

Iridates do not support the conventional picture of strongly correlated electron systems. This picture suggests that 4d and 5d TMOs should be more metallic and non-magnetic materials because of their naturally more extended orbitals. Figure (1.6) shows a comparison between 3d, 4d and 5d transition metals' charge density as a function of the ionic radius. The more extended orbitals are supposed to minimize (e-e) interaction as the electrons are further apart. This argument contradicts the observations, because as the extended orbitals minimize the in-site Coulomb repulsion, they enhance the overlap between d-orbitals and p-orbitals of oxygen, which is known as d-p hybridization. Another aspect of the heavy TMO iridates is the strong spin-orbit interaction; because of the high atomic number $Z = 77$, the SOI becomes a comparable interaction energy to other competing energies. These competing energies include the (e-e) Coulomb interaction, Hund's rules, and the non-cubic crystal field effect (CFE). This new balance of competing energies is the key to understanding many exotic properties in iridates [24]. The balance of these energies is also highly susceptible to small perturbations and changes –for example, chemical doping, application of pressure and/or external magnetic field, and even temperature change. These perturbations are relatively weak from the energy scale point of view, but are capable of influencing the balance of these energies [25]. Table (1.1) shows a brief comparison of these interaction energies between 3d, 4d TMOs and iridates.

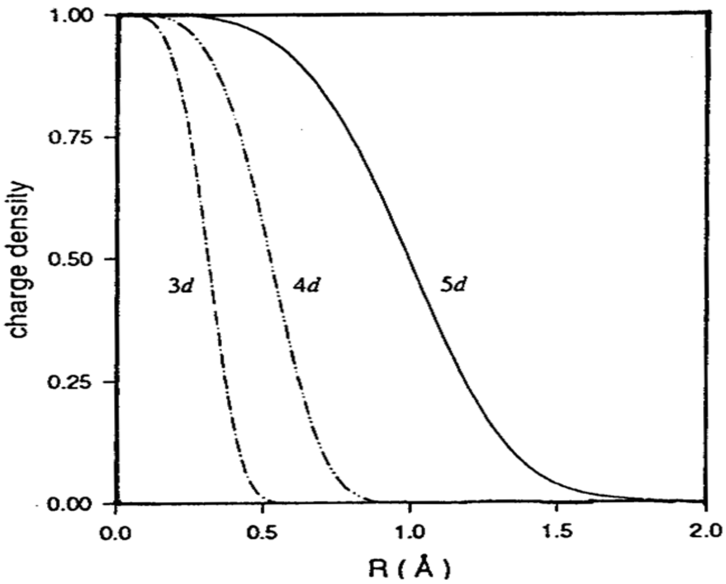

Figure 1.6: Charge density as a function of the ionic radius for the three different series of transition metals 3d, 4d and 5d [15].

Table 1.1: A comparison of interaction energies between 3d, 4d TMOs and iridates [25].

TMOs	U (eV)	SOC (eV)	interactions (eV)	Phenomena
$3d$	5-7	0.01-0.1	U $>$ CF $> \lambda_{SO}$	HTSC/CMR
$4d$	0.5-3	0.1-0.3	U $\sim CF \ > \lambda_{SO}$	magnetism, p-wave SC
$5d$ Iridates	0.4-2.0	0.1-1.0	U$\sim$ CF $\sim \lambda_{SO}$	novel insulating state

1.5 The Merits of Single-Crystals

The simple definition of crystal consists of two parts: First, the lattice, which is an infinite periodic arrangement generally in three dimensions; and second, specific formula units called *bases*, atoms or molecules, to fill the space of the lattice periodical arrangement on certain sites called *lattice points* [26]. In mathematical form, we can simplify this definition as:

$$Crystal \;=\; Lattice \;+\; Bases$$

Based on this definition, single crystals are the ideal example to satisfy these requirements. Unlike the other forms of solid-state materials, such as polycrystalline or quasi-crystalline materials and amorphous materials, single crystals usually possess the natural shape of the crystal structure. Additionally, having a high quality single crystal is of considerable necessity in both research as well as technology. Working with single-crystal samples is favorable for the following advantages [27]:

- Single–Crystal samples make it easy to define the basic crystallographic directions $a,\ b,\ and\ c$ and measures these and the other lattice parameters with a high degree of accuracy using a single-crystal x-ray diffractometer.
- Usually the samples represent a pure form of the desired phase.
- Single-Crystal samples have no grain boundaries issues and domain limitations.
- These samples have the lowest minimum values of lattice point-like defects, disorder, and imperfections.
- Single crystals are the perfect samples for research and studying the intrinsic properties of novel materials and to distinguish the anisotropic features along the different directions of the crystallographic axes a, b, and c.

Single-crystal synthesis and growth is a subject that combines three efforts: science, technology and some experience skills. There are a number of techniques and methods developed for single-crystal growth. Some of the techniques are applicable for laboratory research tasks and others are more suited to technology and industry demands. These different procedures can be classified into four categories:

- Solid growth: Here, the crystals are grown through a solid-solid phase transition, and the crystals are formed within a temperature range below the melting temperature.
- Melt growth: This is the most popular and simplest procedure where crystals are grown by normal or controlled cooling from the molten medium.
- Vapor growth: This procedure includes growth of the crystals by condensation/solidification from the gaseous phase as well as sublimation.
- Solution growth: This includes the growth from chemical solvent solutions or flux mixture for high temperature molten medium.

The single crystals of this work were synthesized using a technique known as the self-flux method, which is a melt growth technique. In this technique, crystals are grown from molten salts and/or pure metals solvents at high temperature. The addition of flux salts has the advantage of lowering the melting temperature of the precursors and hence pushes the metastable phase of crystal growth below the liquid phase. In addition, single-crystals synthesized by this technique are formed with higher quality in terms of purity, homogeneity, and with fewer defects. Another important aspect of this technique is that it is applicable for congruent as well as incongruent materials with the possibility of working effectively with high vapor pressure materials. For this technique to be more effective, it needs a careful consideration of the choice of the proper fluxes and the precise ratio of the mixture. There are a number of factors that should be taken into account:

- The solubility degree of the precursors' materials in the fluxes should be moderate with no stable intermediate phase formation between the flux and solute.
- Low viscosity, low melting point, and low volatility of the molten flux at the highest growth temperature.
- There should be compatibility between the fluxes and the crucible materials as well as with the furnace material.

Chapter 2 THEORETICAL BACKGROUND

2.1 Crystal Structure

Knowledge of the crystal structure, including lattice parameters, symmetry, and the set of atomic coordinates, is fundamental to the study of the physics and chemistry of crystalline materials. The crystal structure is a consequence of the existence of ordering or the periodic arrangement of the constituents of a crystalline material. The hard sphere model of atoms or ions, the basic constituents of any material, can explain a number of simple crystal structures. By packing such hard spheres together, we can construct different arrangements that can be conceptualized as the basic unit for long-range periodic arrangement. The two basic and simple choices of hard spheres packing are: the close-packed hexagonal or honeycomb arrangement, and the square arrangement, as shown in figure (2.1). The close-packed hexagonal arrangement is the most compact packing for atoms in a single layer, while the square packing allows for larger interstices in between atoms. Stacking these different packing layers in specific orders results in the formation of different three dimensional crystal structures. For example, the simple hexagonal structure results from stacking the layers in the close-packed hexagonal arrangement in such a way as to place the atom centers directly above one another. The common hexagonal close-packed (hcp) structure results from stacking the layers in such a way that the atoms of the second layer sit above the interstices of the first layer. The atoms of the third layer sit directly above the atoms of the first layer. The fourth layer sits directly above atoms of the second layer. The alternation sequence of such stacking is described as an $ABAB$ sequence. On the other hand, if the third layer atoms, sit directly over the unoccupied interstices of the first layer, and those of the fourth layer sit directly on the atoms of the first layer,

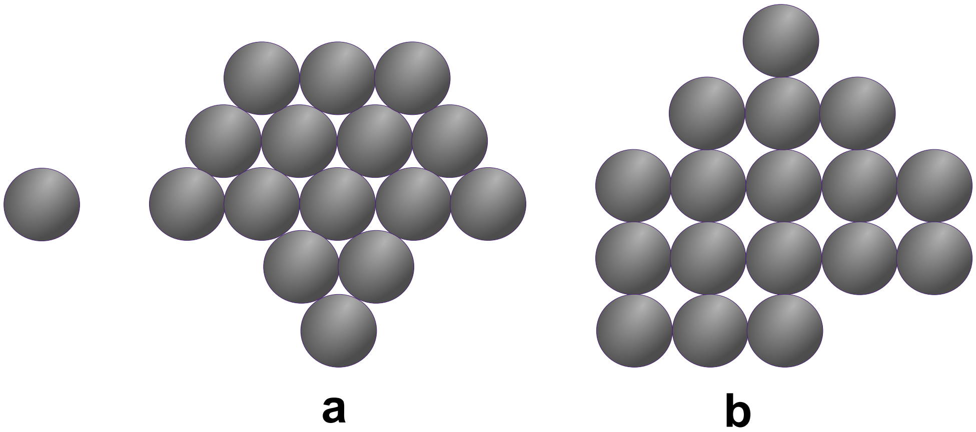

Figure 2.1: hard spheres packing: (a) the close-packed hexagonal or honeycomb arrangement, and (b) the square arrangement.

the sequence alternates as $ABCABC$, and the resultant structure is the cubic close-packed (ccp) structure. Many materials show combinations of these two sequences. For example, the lanthanide elements Pr, Nd, and Sm have the stacking sequence of $ABACABAC$. This is a four-layer periodicity, which is essentially a combination of an hcp and a ccp stacking sequence. Different stacking sequences for close-packed hexagonal arrangements and square arrangements result in different unit cell and symmetries for different crystal structures.

Interstitial structures; These structures include crystal structures consisting of atoms that are different in size. An ideal example of an interstitial structure is the case when small atoms or ions occupy the interstices between the larger atoms in hcp or ccp structures. Another distinction for the interstitial structures is the ways in which the small atoms or ions distribute themselves in between these interstices. In the ccp structure, there are two different interstices between the close-packed layers, where smaller different atoms or ions can be accommodated. These two interstices

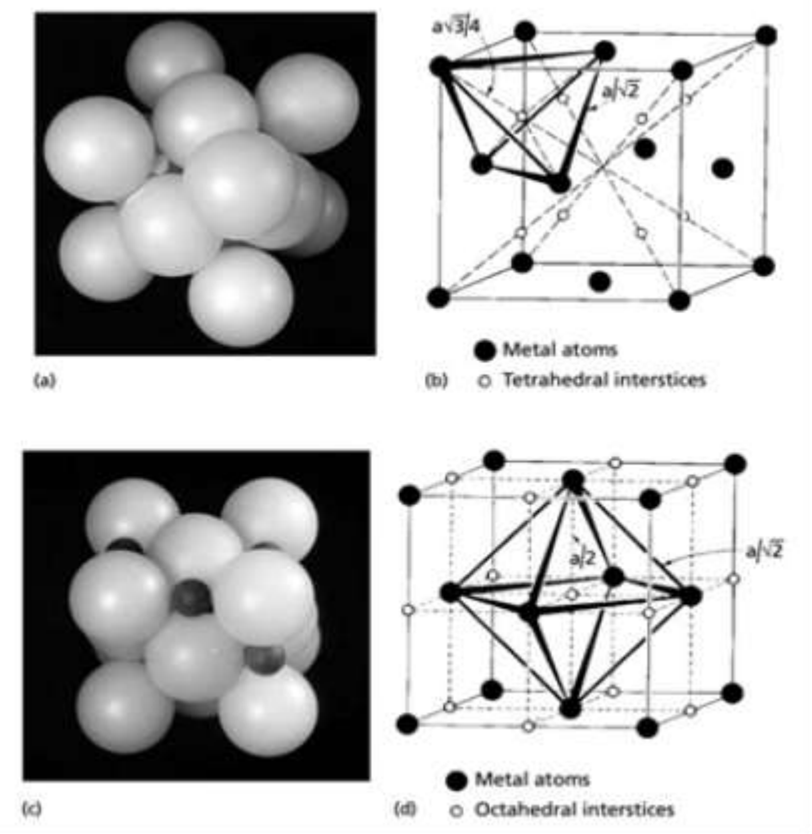

Figure 2.2: Interstitial structure; (a) tetrahedral interstitial site of ccp unit cell. (b) geometry of tetrahedral site showing the dimensions in terms of the unit cell length a. (c) octahedral interstitial site of ccp unit cell. (d) geometry of octahedral site showing the dimensions in terms of the unit cell length a [28].

have different sizes and shapes. The first one is known as a tetrahedral interstitial site, in which the smaller ion or atom is coordinated by four larger atoms, one from the layer B atoms and three from the layer A atoms, at equal distance from the smaller atom. These four atoms construct the shape of a tetrahedron. The other interstice is larger than the tetrahedral interstitial site. The smaller ion that can fit in there is coordinated by six large atoms, three from the layer B atoms and three from the layer A atoms. These six large atoms construct the shape of an octahedron and is therefore known as an octahedral interstitial site. The positions of the tetrahedral interstitial sites and the octahedral interstitial sites in the ccp unit cell are shown in figure (2.2) The size of the smaller atom or ion that is able to occupy any of these two interstitial sites can be calculated in terms of the radius ratio $\frac{R_x}{R_A}$, where R_x is the radius of a smaller atom and R_A is the radius of the large atom in A or B layers. In the ccp structure, $\frac{R_x}{R_A}$ for the tetrahedral sites is 0.225, and that for the octahedral sites is 0.414. In oxides and other compounds though, the metal atoms (cations) are smaller than the oxygen, chlorine, etc. atoms (anions), the radius ratio $\frac{R_x}{R_A}$ is not enough to describe their crystal structure. In these compounds, other interactions between the constituents are very important in understanding the crystal structure.

2.2 X-ray Crystallography

Shortly after the discovery of x-rays by Röntgen in 1895, a new branch of science emerged known as x-ray crystallography. von Laue and his colleagues established the first concepts of x-ray crystallography in 1912. X-ray crystallography is a powerful tool used to study the structure of crystalline materials. It is based on a diffraction phenomenon, or diffracting the x-ray radiation by the parallel atomic planes of a crystal. It is referred to as x-ray diffraction (XRD). The fundamental principle is that XRD occurs because the inter-planar distances of a crystal are comparable to the x-ray wavelength, which is on the order of an ångström (10^{-8} cm) [28]. XRD has become a widely popular technique to use in research and technology because of two important features: first, it is a non-destructive test, and second, it can be a fingerprint to identify different forms of materials. In general, two common different techniques incorporate XRD: powder XRD and single-crystal XRD. When an x-ray beam is incident on a crystal, a diffraction pattern consisting of constructive and destructive interference can be recorded. Bragg's law, an equation (2.2) derived in 1913, is applicable to study the geometry of the constructive spots. The geometry of Bragg's law is illustrated in figure (2.3), which shows a simple crystal with one atom at each lattice point. The path difference between the waves scattered by atoms from adjacent (hkl) lattice planes set of spacing d_{hkl} is given by [28]:

$$(A+B) = d_{hkl}\sin\theta + d_{hkl}\sin\theta = 2d_{hkl}\sin\theta \tag{2.1}$$

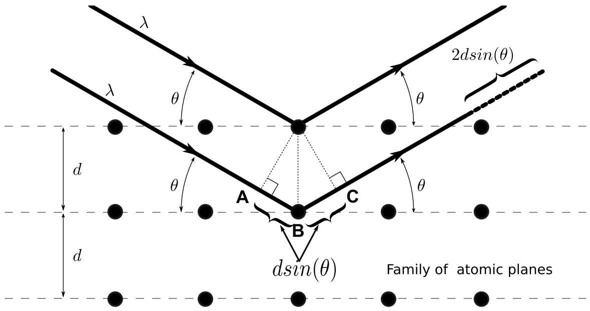

Figure 2.3: The geometry of Bragg's law for XRD

Hence, for constructive interference, this path difference should be equal to an integer number of wavelengths of the x-ray.

$$n\lambda = 2d_{hkl}\sin\theta \tag{2.2}$$

Here, n is an integer called the diffraction order, λ is the x-ray wavelength, d_{hkl} is the interplanar distance between the crystal planes where hkl are the Miller indices, and θ is the incident angle of the x-rays. The integer n normally is incorporated into the lattice plane symbol, and Bragg's law becomes:

$$\lambda = 2(\frac{d_{hkl}}{n})\sin\theta = 2d_{nhnknl}\sin\theta \tag{2.3}$$

The indices nh nk nl are called Laue indices for the reflecting planes of spacing $\frac{d_{hkl}}{n}$. Bragg's law states that constructive interference will be satisfied only if the difference in path of the diffracted x-ray waves, from a particular set of crystal planes, is an integer multiple of the x-ray wavelength λ. Every set of crystal planes will satisfy this condition at a particular incident angle θ. Bragg's law applies regardless of the positions of the atoms in the planes. Instead, the spacing between the crystal planes is the important factor in applying the law. This is obvious as the path difference between the waves scattered by atoms in the same plane is always zero. The sets of crystal planes are limited by the crystal structure properties and the symmetry restrictions. The resultant diffraction will have a discrete spatial distribution of diffracted intensities. This distribution can be mapped into diffraction intensity peaks as a function of the diffracted angle 2θ, which is the angle between the incident and diffracted x-ray paths.

In XRD, the electronic charge density is an important factor in determining the intensity and distribution of diffracted peaks. This can be seen from expression (2.4), which gives the diffracted intensity (I) as a function of (2θ), and was derived by John William Strutt [28].

$$I(2\theta) = I_0(\frac{ne^4}{2r^2m^2c^4})(\frac{1+\cos^2(2\theta)}{2}) \tag{2.4}$$

Here, I_0 is the intensity of a non-polarized incident beam, e is the electron charge, c is the speed of light, n is the number of scattering sources, m is the mass of scattering source, r is the distance from the scattering source to the detector, and 2θ is the angle between the incident and scattered waves. This expression relates the intensity of scattering waves to the physical properties of the source of scattering. It shows that the scattered intensity is inversely proportional to the squared mass of the particle that causes the diffraction of the x-ray radiation. According to this proportionality, the scattering by the atomic nuclei is negligible compared to the scattering by the electrons. To account for the total scattered amplitude of all the electrons in all the atoms in the crystal, we need to sum over all these electrons for the scattering amplitude of a single electron as a function of the scattering angle. The scattering amplitude of an atom (with the atomic number Z) is determined by summing over the contributions from all Z electrons in the atom, taking into account the path or phase differences between all the Z scattered waves. For this, we define the atomic scattering factor f, which is the ratio of the scattering amplitude of the atom divided by the scattering amplitude of a single electron:

$$f = \frac{amplitude\ scattered\ by\ an\ atom}{amplitude\ scattered\ by\ a\ single\ electron}$$

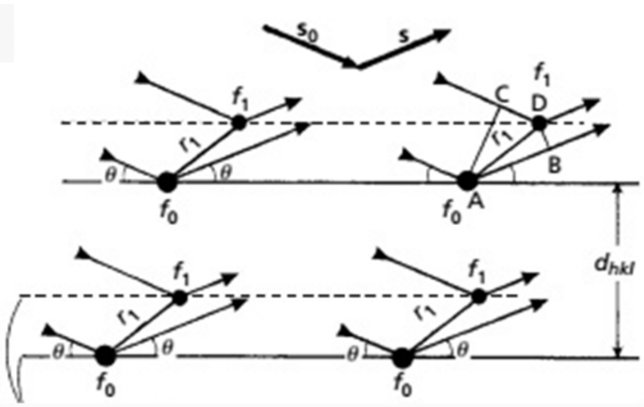

$(hx_1+ky_1+lz_1)d_{hkl}$ = component of r_1 perpendicular to reflecting planes

Figure 2.4: A crystal lattice with one atom with atomic scattering factor f_0, situated at each lattice point, and another atom with atomic scattering factorf_1 defined by position vector$\vec{r_1}$. A particular set of (hkl) planes through the lattice points is shown. Incident/reflected beams at the Bragg angle θ to these planes are indicated by the arrows. The path difference (shown for simplicity for one motif) is given by (AB – CD),$\vec{s}$ and $\vec{s_0}$ are unit vectors along the reflected and incident beam directions and the component of $\vec{r_1}$ perpendicular to the (hkl) planes is also indicated [28].

At zero scattering angle, all the scattered waves are in phase and the scattered amplitude is the sum of all Z electrons, and f is just equal to the atomic number Z, $(f = Z)$.

As the scattering angle increases, f falls below Z because of the increasingly destructive interference effects between the Z scattered waves from the other electrons. The scattering amplitude of a unit cell is determined by summing the atomic scattering amplitudes, f, from all the atoms in the unit cell. This scattering amplitude is defined by a dimensionless factor called the structure factor F_{hkl}:

$$F_{hkl} = \frac{amplitude\ scattered\ by\ all\ the\ atom\ in\ a\ unit\ cell}{amplitude\ scattered\ by\ a\ single\ electron}$$

F_{hkl} is not just a dimensionless number, like f, it is a complex number. As a simple example, consider a crystal with bases consisting of two atoms, one at the origin with atomic scattering factor f_0 and another one with atomic scattering factor f at a distance from the origin defined by the position vector $\vec{r}$, which is defined along the unit cell vectors $\vec{a}, \vec{b}$, and $\vec{c}$. Then:

$$\vec{r_1} = x_1\vec{a} + y_1\vec{b} + z_1\vec{c} \tag{2.5}$$

It is similar to a lattice vector $r_{\vec{uvw}} = u\vec{a} + v\vec{b} + w\vec{c}$. The difference being that the components x_1, y_1, andz_1 are fractions of the cell edge lengths, whereas the components u, v, and w of a lattice vector $r_{\vec{uvw}}$ are integers. If two x-ray waves are being scattered by these two atoms, the path difference $(P.D.)$ between these two waves is by:

$$P.D. = AB - CD = \vec{r_1} \cdot \hat{s} - \vec{r_1} \cdot \hat{s_0} = \vec{r_1} \cdot (\hat{s} - \hat{s_0}) \tag{2.6}$$

Where $\hat{s}, \hat{s_0}$ are unit vectors along the direction of the reflected and incident beams, respectively. If the position vector $\vec{r_1}$ is defined in terms of its components $x, y, and z$, and Bragg's law applied for the path difference then the difference vector $(\hat{s} - \hat{s_0})$ can be expressed in terms of λ and d_{hkl}.

$$(\hat{s} - \hat{s_0}) = \lambda \vec{d^*_{hkl}} = \lambda(h\vec{a^*} + k\vec{b^*} + l\vec{c^*}) \tag{2.7}$$

$\vec{a^*}, \vec{b^*}$, and $\vec{c^*}$ are the unit cell vectors of the reciprocal lattice, and $\vec{d^*_{hkl}}$ is a lattice vector in the reciprocal space. Then, equation (2.6) becomes:

$$P.D. = \lambda(x_1\vec{a} + y_1\vec{b} + z_1\vec{c}) \cdot (h\vec{a^*} + k\vec{b^*} + l\vec{c^*}) \tag{2.8}$$

Using the complex multiplication identities $a \cdot a^* = 1$, etc., and $a \cdot b^* = 0$, etc.. then:

$$P.D. = \lambda(hx_1 + ky_1 + lz_1) \tag{2.9}$$

The number $(hx_1 + ky_1 + lz_1)$ is a real number that represents the component of $\vec{r_1}$ perpendicular to the lattice planes as a fraction of the interplanar spacing,d_{hkl}, see figure (2.4). For example, when $(hx_1 + ky_1 + lz_1) = 0$, the two atoms lying within the hkl planes, the diffracted waves result in complete constructive interference. When $(hx_1 + ky_1 + lz_1) = \frac{1}{2}$, the second atom lying halfway between the hkl planes, the interference between the diffracted waves is destructive interference, and if $f = f_1$ the destructive interference is complete.

The determination of a correct crystal structure consists of two tasks. First, straightforward calculation of the lattice parameters, the axes, angles, volume, and lattice type, using the diffraction spot positional information collected from a diffraction pattern. Secondly, distribution determination of the atoms in the structure. These calculations depend on the relative intensities of the diffraction spots in the diffraction pattern. The second task is not a straightforward calculation because the relative recorded intensities are proportional to the squares of the amplitudes. These amplitudes express just one component of the complex structure factors F_{hkl}. When a complex number is squared, the result is a real number and hence all information about the phase angles of the diffracted beams is lost. The recovery of such phase information is a challenge in crystal structure determination. Solution of the phase problem needs a deep understanding and intuition for mathematical and crystallographic knowledge.

In general, the practical diffracted intensity in XRD can be described by the expression (2.10)[29]

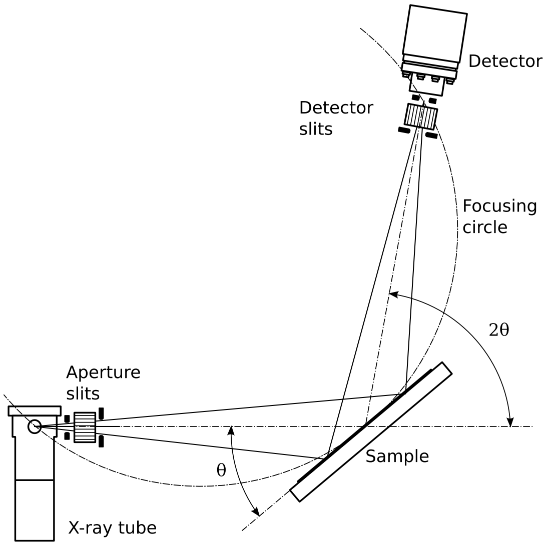

Figure 2.5: Schematic diagram of Bragg-Brentano diffraction geometry for powder XRD in $\theta - 2\theta$ configuration [30].

$$I = k|F_{hkl}^2|[\frac{1+\cos^2(2\theta)\cos^2(2\alpha)}{\sin^2(\theta)\cos(\theta)(1+\cos^2(3\alpha))}]P \cdot A(\theta) \cdot e^{(\frac{-2B\sin^2(\theta)}{\lambda^2})} \tag{2.10}$$

Here, k is just a scaling factor; F_{hkl} is the structure factor; the expression inside the square parentheses relates to the Lorentz polarization factor, which is a function of the geometry of the diffractometer; P is the multiplicity of the diffracting plane. The term $A(\theta)$ is the absorption correction parameter, and the exponent term is a temperature dependence factor accounting for thermal vibrations. The structure factor F_{hkl} is also a function of the spatial atomic distribution and the atomic number.

The extracted information from the single-crystal XRD helps in determining, with a high degree of accuracy, the unit cell, and its lattice constants - atomic coordinates, bonds' angles, and bonds' length. In powder XRD, the samples are polycrystalline materials or micro-single-crystal samples. In such samples, there are all the possible sets of the crystal planes families oriented randomly in space, and the incident x-rays will diffract constructively by the appropriate set of planes. The goniometer in most of the powder XRD instruments is simpler than those of single-crystal XRD systems. The most common design is Bragg-Brentano para-focusing geometry shown in figure(2.5). This design allows a high resolution and high intensity diffracted x-rays. In this design, the x-ray tube and the detector are mounted on the two arms of a goniometer. This goniometer rotates around a common axis where the sample holder is centered and parallel to the sample plane. Powder XRD measurements serve as a fingerprint for the studied materials. In addition, some other valuable information can be obtained from powder XRD, such as grain's size and preferred orientation.

2.3 Electronic Configuration Interactions

This section presents a brief description about the relevant interactions and energies that relate to the electronic and magnetic configuration of many TMOs.

2.3.1 Crystal Field Effect

The crystal field effect (CFE) reflects the interaction between the ions and their surrounding neighbors as they hold together in a crystalline structure. For a free atom or ion, the five d-orbital configurations are energetically equal and degenerate. When the atom or ion becomes close to, or is surrounded by a non-spherical electrostatic environment, the five d-orbital configurations split into two subsets. CFE is responsible in lifting the degeneracy of the atomic d-orbitals to form the two subsets of molecular d-orbitals, e_g and t_{2g}. As shown in figure (2.6), the two subsets of these d-orbitals have two different configurations for the angular distribution, or charge probability-density distribution. In a Cartesian frame, the e_g subset has an angular distributions point along the coordinate axes and the t_{2g} subset orbitals point in between these axes. The strength and nature of the CFE depend mainly on the symmetry of the surrounding environment. CFE is different for different environments, such as oxygen (O^{-2}), Chlorine (Cl^{-1}), or any other halogens or chalcogens.

In TMOs, the most common environmental symmetries are the octahedral coordination and the tetrahedral coordination. Manganese oxide MnO is a good example for the octahedral coordination, where the Mn^{2+} cation is coordinated by six anions of O^{2-}. In the octahedral coordination, the electrons of orbitals $d_{x^2} - y^2$ and d_{z^2} experience more repulsion energy than that of the electrons of d_{xy}, d_{yz}, d_{xz} orbitals. This difference in the repulsion interaction causes the d-orbitals to be split by an energy difference of Δ_{oct}. Because of this splitting, the e_g subset will be a higher energy band and the subset t_{2g} will have lower energy, see figure (2.7).

In tetrahedral environment symmetry, the splitting flips the two sets' configuration. In this symmetry, there are four oxygen anions at the cube corners in an alternative

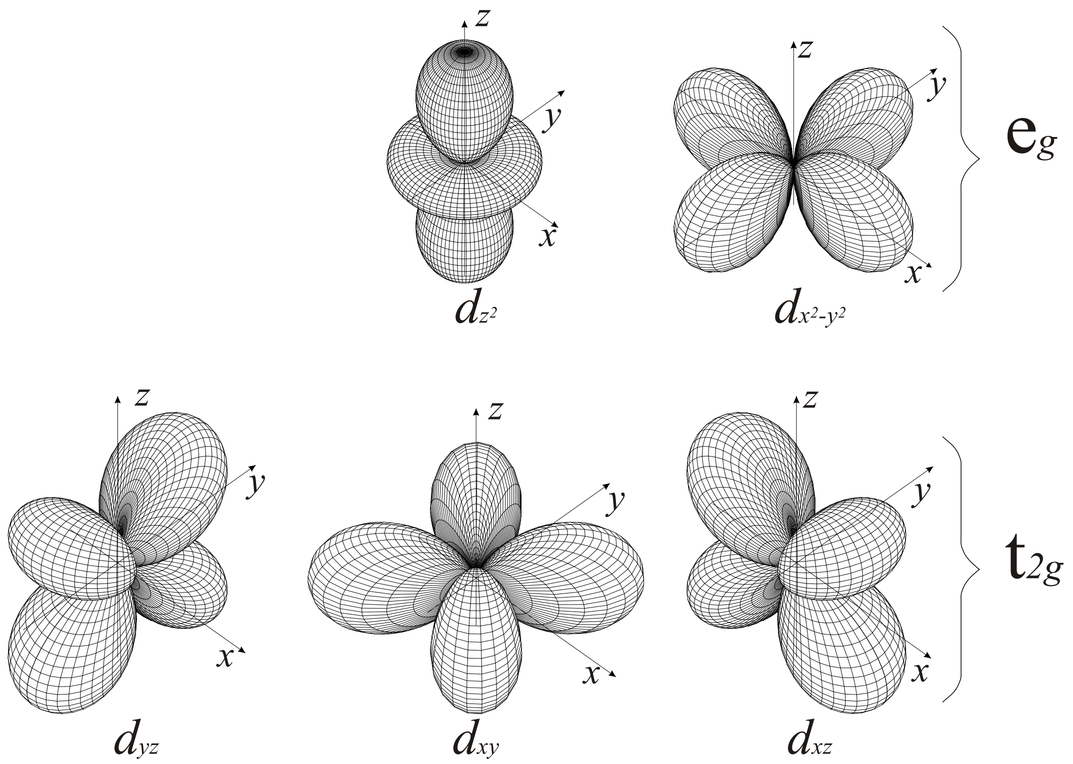

Figure 2.6: The radial distribution of the two subsets e_g and t_{2g} of d-orbitals. [14].

arrangement. In this case, the t_{2g} subset has higher energy as the d_{xy}, d_{yz}, d_{xz} orbitals point toward the center of the cube edges. The $d_{x^2} - y^2$ and d_{z^2} orbitals of the e_g subset point toward the center of the cube faces. Hence the order of splitting in a tetrahedral environment Δ_{tetr} is opposite to that of the octahedral environment as illustrated in figure (2.7). In the tetrahedral environment symmetry or the octahedral environment symmetry, the non-degenerate d-orbitals of t_{2g} and e_g subsets will have an internal ordering. Two different situations emerge when filling these ordered orbitals. In one case, known as the strong-field case, the CFE splitting energy Δ is higher than the energy required to pair the electrons. In this case, the filling will finish double occupancy for the low energy orbitals before starting the ones with higher energy. The electronic configuration in this case called low spin state. The second case is the weak-field case, the CFE splitting energy Δ is smaller than the pairing energy, and the filling will occupy all the orbitals with a single electron before double occupancy starts. This electronic configuration gives a rise of high spin state. The low and high spin states are related to the Hund's rules.

2.3.2 Jahn-Teller Effect

The crystal structure in many TMOs does not possess a perfect symmetric CFE. This is usually because of lattice defects, intrinsic mixed valence, or some external perturbation. This distortion in a crystal environment is referred to as the Jahn-Teller

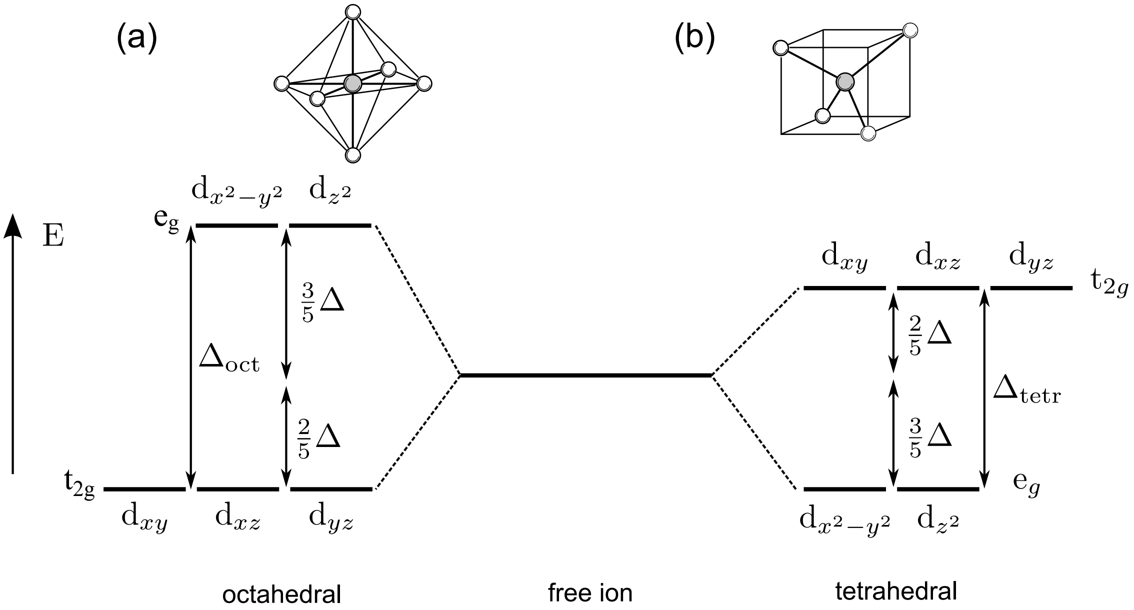

Figure 2.7: The CFE and splitting for (a) octahedral and (b) tetrahedral environments [14].

(JT) effect. It results in a further degeneracy lifting for the two subsets, t_{2g} and e_g. As an example of JT effect distortion, suppose that a symmetric octahedra has elongated along the z-axis (see figure 1.4). In this case, the d_{z^2} orbitals become lower energy as the repulsion interaction between d-electrons and the p-orbitals electrons becomes weaker, so the t_{2g} degeneracy is lifted. The JT effect is exhibited by TMOs with an octahedral environment of high spin state and have d^4 transition metal cations like Cr^{2+} or Mn^{3+} with the electronic configuration $t_{2g}^3 e_g^1$. The JT effect can be classified into three categories. The first is the static JT effect; this is a spontaneous distortion that occurs within the octahedral environment structure. This type of distortion occurs in particular axis, and it is a static distortion. The second category is the dynamic JT effect. Here,there is a coupling between a particular vibrational mode and electronic motion; the distortion in this case is extended to affect another different axis, and may be accompanied by translation. The dynamic JT effect is a temperature dependent effect. The third category is the cooperative JT effect; this distortion is also temperature dependent and spontaneously translates through the whole crystal space.

2.3.3 d-p Hybridization

The d-p hybridization is the overlap between the transition metal d-orbitals and the surrounding oxygen p-orbitals. In the Ligand theory explanation, this overlapping is the interaction that is responsible for the orbital ordering and the coordination complexes in TMOs. The term "hybridization" refers to the fact that the bonding is not the result of pure atomic orbitals, or the pure orbitals of the Schrödinger equation

solution, rather there is a mixing from other types of orbitals. The narrow d-band lies within the sp-band, and hence hybridizes it at the crossing. A quantum mechanical approach perceived in constructing a molecular wavefunction by combining the atomic wavefunctions to give a new hybrid wavefunction. When a d-electron has promoted to the outermost shell, then $(n-1)d$, ns and np electrons will have a good chance to hybridize. This hybridization is denoted as $d^x s^y p^z$ hybrid, where x, y, and z indicate the number of electrons involved. Another possibility can occur if s and p orbitals are promoted to vacant d-orbitals in the same shell, this will involve hybridization of ns, np and nd electrons and is denoted as $s^x p^y d^z$ hybrid. The common configurations in many TMO crystals are d^2sp^3 and sp^3d^2 hybrids; those cause bonds to direct toward the corners of a regular octahedron. For example, in the superconductor ruthenates Sr_2RuO_4 the $Ru4d_{xy,yz,xz}, O2p$ hybridization is favorable [31].
In many cases, the d-p hybridization affects or couples the magnetic and transport properties of TMO system. Practically, the d-p hybridization can be enhanced by decreasing the inter-distance between the structure's ions, which alters the lattice parameters. This is possible by applying pressure or inducing a distortion via a chemical doping in the system. The enhancement in d-p hybridization reflects in a stronger spin-spin interaction, exchange interaction and, in turn, affects the magnetic and transport properties.

2.3.4 Spin-Orbit Interaction (SOI)

Spin-Orbit interaction is a relativistic effect. This relativistic effect originates from the orbiting of the electron through the electric/magnetic field of the nucleus, or vice versa as seen by the electron rest frame, see figure (2.8). SOI is another effect that involves an interaction between the three degrees of freedom; charge, spin and orbital. This interaction is an important mechanism in affecting the electronic and magnetic properties and the transitions in many compounds that are based on a transition metal of a high atomic number (Z). In iridates, SOI is a driven interaction that introduces an additional interaction term to the energy scale. SOI causes a lifting of degeneracy of the atomic energy levels and hence competes with other interaction energies. To understand the physics of SOI, we start by expressing the magnetic field $\vec{B}$ at the origin that results from orbiting nucleus and can be expressed as:

$$\vec{B} = \frac{\vec{E} \times \vec{v}}{c^2} \tag{2.11}$$

where,

$$\vec{E} = -\vec{\nabla} V(r) = -\frac{\vec{r}}{r}\frac{dV(r)}{dr} \tag{2.12}$$

is the electric field at the electron position r, $V(r)$ is the corresponding potential energy. This magnetic field interacts with the electron spin and we can write the Hamiltonian contribution H_{SO} because of SOI as:

$$H_{SO} = -\frac{1}{2}\vec{\mu} \cdot \vec{B} \tag{2.13}$$

With the relations:

$$\hbar\vec{L} = m\vec{r} \times \vec{v} \quad \text{and} \qquad \vec{\mu} = \frac{ge\hbar}{2m}$$

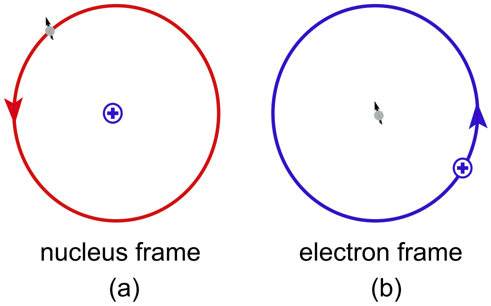

Figure 2.8: The intrinsic spin-orbit Interaction: (a) in the frame of the nucleus the electron orbits the nucleus and (b), in the inertial frame of the electron, it is the nucleus which is orbiting

we can rewrite the Hamiltonian equation as:

$$H_{SO} = \frac{e\hbar^2}{2m^2c^2}(\frac{1}{r}\frac{dV(r)}{dr})\vec{S} \cdot \vec{L}. \tag{2.14}$$

The Coulomb field for one-electron atom can be written as:

$$(\frac{1}{r}\frac{dV(r)}{dr}) = \frac{Ze}{4\pi\epsilon_0 r^3}$$

For a quantum electronic state with n and l as good quantum numbers, the expectation value is given as:

$$\langle r^{-3}\rangle = \frac{Z^3}{a_0^3 n^3 l(l+\frac{1}{2})(1+1)}. \tag{2.15}$$

The $\vec{L}$ and $\vec{S}$ are no longer good quantum numbers to describe the system. Now we have the total angular momentum $\vec{J} = \vec{L} + \vec{S}$ as a good quantum number, hence we can find an expression for $\vec{L}.\vec{S}$:

$$\vec{L}.\vec{S} = \frac{1}{2}(J^2 - L^2 - S^2) \tag{2.16}$$

L^2 and S^2 are still good quantum numbers as well as J^2, therefore the $(\vec{L}.\vec{S}\ )$ eigenvalues are:

$$\frac{\hbar}{2}[j(j+1) - l(l+1) - s(s+1)] \tag{2.17}$$

For $s = \frac{1}{2}$ state, the energy splitting due to this interaction (SOI) is given as:

$$\varepsilon_{SO} = \langle H_{SO} \rangle = \frac{e^2 Z^4}{8\pi\epsilon_0 m^2 c^2} \{ \frac{\frac{\hbar}{2}[j(j+1) - l(l+1) - s(s+1)]}{l(l+\frac{1}{2})(l+1)n^3 a^3} \} \tag{2.18}$$

This approximation is applicable under the condition of small fields, when the applied field is smaller than the internal field. The energy splitting is proportional to the fourth power of the atomic number Z.

2.4 Magnetic Interactions

These interactions are the backbone of the field of magnetism in condensed matter and have given rise to hot topics in the level of fundamental research such as spin liquid, ferromagnetism, and low dimensional magnetic materials [13]. Magnetism phenomenon is a collective behavior resulting from the mutual interaction between the magnetic moments of the material constituents. In a non-relativistic limit, the Hamiltonian for an electron interacting with an external static magnetic field ($\vec{B} = \vec{\nabla} \times \vec{A}$) and electric field ($\vec{E} = -\vec{\nabla}\phi$), can be set as [32]:

$$\hat{H} = \hat{H}_0 + \hat{H}_S + \hat{H}_{SO} + V(r) \tag{2.19}$$

Here $\hat{H}_0$ is the Hamiltonian of a spinless orbiting particle in a magnetic field, $\hat{H}_S$ is the spin Hamiltonian, $\hat{H}_{SO}$ is the SOI contribution and $V(r)$ is an electrostatic potential. There are another two contributions from the perturbed spinless particle due to a magnetic field:

$$\Delta\hat{H} = \hat{H}_L + \hat{H}_D \tag{2.20}$$

$\hat{H}_L$ is related to the angular momentum contribution and is a paramagnetic response of magnetism. $\hat{H}_D$ is a weaker contribution and it is a diamagnetic response.
The long-range order in magnetic materials is an evidence of creating a net magnetic moment because of the competition between two interactions; thermal excitations, vibrations, cause random orientations to the spins, and exchange interactions tend to align the spins. As the temperature goes down, the thermal excitations settle down and a spontaneous cooperative magnetic order is established. The most relevant interaction mechanisms in magnetism are listed below.

2.4.1 Hund's Rules

These are three empirical rules that state the spin and orbital favorable configuration of a partially filled subshell. Many other interaction energies can affect, or invalidate Hund's rules, and limit their application.

- **Hund's first rule:** For an atom or ion with l *and* s as good quantum numbers, there are $2(2l+1)$ total allowed states for electronic configurations in a partially filled shell. n electrons occupy the electronic states of lowest energy first in such a way to have a maximum spin S for the atom. The total spin of less than half-filled occupation will have maximum spin given by:

$$S = \frac{1}{2}(n) \tag{2.21}$$

When $n = 2l + 1$, S will have maximum $S = l + \frac{1}{2}$ and any additional electron causes S to be reduced.

- **Hund's second rule:** The lowest-lying energy states should have the maximum total orbital angular momentum L. This condition is consistent with Hund's first rule and the Pauli exclusion principle. This maximum L should be the maximum value that L_z can attain. In filling these states, the first electron will have l, the maximum value for l_z, and the second one will have the value $(l-1)$, and so on until the occupancy has $\frac{n}{2} - 1$ electrons. When a next electron is added, all the possible values of l_z have been considered and the total orbital angular momentum should equal to zero ($L = 0$). The filling of the second half of the allowed states starts with the maximum value of l_z again, because the next $\frac{n}{2} + 1$ electrons now have opposite spins with respect to the first half of electrons.

- **Hund's third rule:** The total angular momentum is $\vec{J} = \vec{L} + \vec{S}$ and the total number of allowed states is $(2L + 1)(2S + 1)$. J can take any integer value between $|L - S|$ and $L + S$. The SOI lifts the degeneracy of these states, and the Hamiltonian contribution is $\lambda(\vec{L}.\vec{S})$. Maximum J (L *parallel to* S) will have a negative parameter λ, while minimum J when (L *antiparallel to* S) gives a positive λ. The J values in the lowest energy states are assumed as:

$$J = |L - S|, \quad \Rightarrow n \leq (2l + 1), \quad \text{and} \quad J = L + S, \quad \Rightarrow n \geq (2l + 1) \tag{2.22}$$

2.4.2 Exchange Interaction

The spin-spin interaction is a quantum concept that explains the existence of a long-range order in the magnetic materials. For a two-electron system, the total spin can be expressed depending on the singlet-triplet energy splitting, ($S = 0$) for singlet and ($S = 1$) for triplet. The singlet state energy differs from that of the triplet state ($\varepsilon_s \neq \varepsilon_t$). The energy difference between the singlet and triplet states of the combined system is given by:

$$\Delta\varepsilon = 2K - 4St \tag{2.23}$$

$2K$ represents a potential exchange part of the interaction and $4St$ is a kinetic exchange part. The term $2K$ arises from the Pauli principle and leads to Hund's rules which in turn gives a high-spin ground state. In this case, the ground state is ferromagnetically aligned. The kinetic exchange term, $4St$, involves the overlap integral S of the two orbitals and the resonance integral t between those orbitals. The energy difference $\Delta\varepsilon$ becomes negative when the second term is larger. A negative energy difference indicates an antiferromagnetic interaction. The antiferromagnetic interaction is characterized by a stable magnetic configuration. The kinetic exchange term is an antiferromagnetic coupling indicator.

Orthogonality rule This rule states that the exchange interaction will be dominated by the potential part if the orbitals of two different ions are orthogonal, see part (a) of figure (2.9). The result is ferromagnetic coupling between these ions. In the other case, part (b) of figure (2.9), the coupling is antiferromagnetic if there is a substantial overlap between the orbitals. The kinetic exchange term is the dominant factor in this case. The orthogonality rule is easy to check by flipping, or reflecting, the whole system configuration along the line joining the two ions: the bond. The result of this operation is one of two possibilities:

- If the individual orbitals' sign flips, then the system is orthogonal.
- If the sign remains the same, then the system is non-orthogonal.

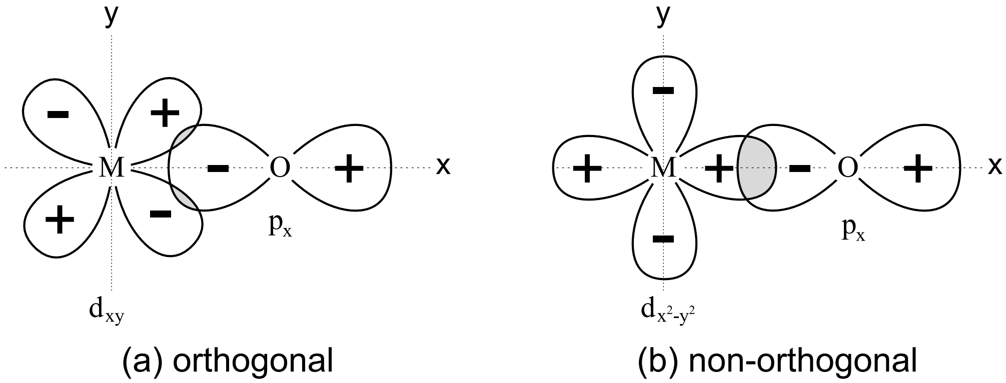

(a) orthogonal (b) non-orthogonal

Figure 2.9: Illustration of orthogonality rule for p- and d-orbitals of metal-oxygen bonds: (a) Orthogonal orbitals, (b) non-orthogonal orbitals [14].

In quantum mechanics description [13], two electronic states of two electrons can be described by two wavefunctions $\psi_a(r_1)$, $\psi_b(r_2)$. To form the compositional wavefunction, that preserves the symmetry and exchange, the resultant wavefunction is the product of the symmetric and the antisymmetric parts of the spin wavefunction of the original states. The total wavefunction of singlet state ($S = 0$) and triplet state ($S = 1$) can be expressed as:

$$\Psi_S = \frac{1}{\sqrt{2}}[\psi_a(r_1)\psi_b(r_2) + \psi_a(r_2)\psi_b(r_1)]\chi_S \tag{2.24}$$

$$\Psi_T = \frac{1}{\sqrt{2}}[\psi_a(r_1)\psi_b(r_2) - \psi_a(r_2)\psi_b(r_1)]\chi_T \tag{2.25}$$

The corresponding energies -ε_S for singlet and ε_T for triplet- are given as:

$$\varepsilon_S = \int \Psi_S^* \hat{H} \Psi_S dr_1 dr_2 \tag{2.26}$$

$$\varepsilon_T = \int \Psi_T^* \hat{H} \Psi_T dr_1 dr_2 \tag{2.27}$$

and the energy difference is defined as:

$$\varepsilon_S - \varepsilon_T = 2 \int \psi_a(r_1)\psi_b(r_2)\hat{H}\psi_a(r_2)\psi_b(r_1) dr_1 dr_2 \tag{2.28}$$

here we assumed that the spin wave functions are normalized, if we define the exchange constant -exchange integral- J from equation (2.29) as:

$$J = \frac{\varepsilon_S - \varepsilon_T}{2} = \int \psi_a(r_1)\psi_b(r_2)\hat{H}\psi_a(r_2)\psi_b(r_1) dr_1 dr_2 \tag{2.29}$$

then, we can express the effective Hamiltonian of nearest-neighbour interaction between magnetic moments in the form:

$$\hat{H}^{spin} = -2J\vec{S_1} \cdot \vec{S_2} \tag{2.30}$$

From this equation, there are two different cases related to the exchange constant J:

- If $J > 0(\varepsilon_S > \varepsilon_T) \Rightarrow$ high spin state (ferromagnetic coupling)
- If $J < 0(\varepsilon_T > \varepsilon_S) \Rightarrow$ low spin state (antiferromagnetic coupling)

This model successfully explains the magnetism of localized narrow-band insulators of covalent non-molecular solids. The different quantum mechanical coupling between the spins in different configurations can be summarized by the chart shown in figure (2.10). As illustrated, the Pauli exclusion principle is the basis of all exchange forces that yield the exchange interaction.

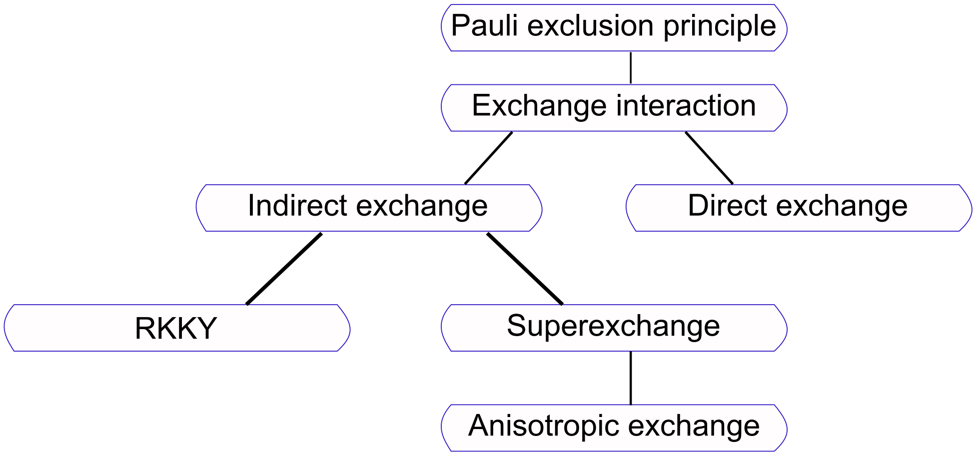

Figure 2.10: Exchange interaction hierarchy [14]

2.4.3 Direct Exchange

In direct exchange interaction, the spins of two magnetic ions, sharing a chemical bond, interact directly and their two wavefunctions overlap. Direct exchange originates from the Coulomb electrostatic interaction because of the spatial arrangement of charges in space. This interaction is a very weak interaction, and would not be able to create long-range order through the system.

2.4.4 Superexchange

Superexchange describes the magnetic interaction between two magnetic ions via a nonmagnetic mediator, such as an oxygen anion. This interaction was first proposed by Kramers [33], and it originates from the overlapping of a cation excited state with an anion ground state to form a mixed state. The cation excited state results from accepting an electron from the anion in which it fills an empty -or half filled- d-orbital. In superexchange interaction, there are three different mechanisms [34]:
Anderson's Mechanism In this interaction model, the involved electrons are from an oxygen p-orbital and a magnetic ion d-orbital. The interaction is strongest if the bond angle between the magnetic ion-oxygen-magnetic ion is 180^0. In this case, two factors affect the coupling strength between the magnetic moments. One is the J exchange constant, and the other is the sign of the bond connecting the two orbitals. The bond sign depends on the occupancy of d-orbitals, it is negative if the orbital is less than half-filled and it is positive if the orbital is more than half-filled. As a general trend for the superexchange interaction coupling, it is antiferromagnetic coupling if the two cations are identical, and it is ferromagnetic coupling if the interaction involves cations with a different population.
Slater's Mechanism In this interaction model, the polarization of the electronic cloud around the anions is important. The resultant superexchange sign in this model is the product of three factors; two are the two simultaneous polarization signs, and multiplied by the third factor, (-1), arise from the Pauli exclusion principle.
Goodenough's Mechanism This model is similar to that of Slater but with an additional feature effect, which is partial bond formation on both sides of anions. The sign of this model coupling is the same as that in Slater's mechanism [35].

2.5 Metal-Insulator Transition (MIT)

The electron correlated systems are a class of materials (introduced in section 1.2) shows a transition from metallic behavior to insulating behavior, or vice versa, under the effect of changing a certain condition. This change could be in the temperature, pressure, or in the crystal parameters via doping. The subject of MIT, in the electron correlated systems, emerged more than half a century ago [36]. Later, the discovery of HTSC has furnished another revision for this subject [37]. Band theory has explained how the overlapping of the electronic orbitals forms large bandwidth W bands ($W >> U$). The shared electrons in this wide band are responsible for making these materials conductors [12]. The conventional pictures could not explain why there is such MIT in the electron correlated materials. The MIT reflects the degree of competition between those energies tend to localize the electrons against the energies trying to delocalize them. The ratio between W and U as a function of bands splitting are sketched in figure (1.2).

In many instances, MIT is coupled to another degree of freedom, for example lattice symmetry or magnetic ordering. The MIT mechanisms describing the different cases of perturbation have been studied in more detail in [15]. The three common MIT mechanisms that have been proposed and observed in many TMOs are listed below.

2.5.1 Disorder Induced MIT

The scattering of charge carriers by defects and impurities in a conductor is a common mechanism behind the drop of electrical conductivity. When these charge carriers have a higher kinetic energy, compared to a scattering potential, which is the case of a good metal, this contribution is really small to the electrical resistivity (ρ). The (ρ) as a function of temperature (T) is a monotonically increasing function and is given by:

$$\rho(T) \simeq \rho_0 + AT^n \tag{2.31}$$

Here, A is a positive quantity and n is a real number. Both are determined by the scattering process, and ρ_0 is the elastic scattering part. In the case of a bad conductor, the impurities' potential is enough to alter Fermi energy and causes electron localization at low temperatures. At low temperatures, the MIT is characterized by a continuous change. The basic description of this behavior was introduced by Anderson [38]. The Anderson MIT can be observed in the case of doping a system with charge carriers, electron or hole, which alters the Fermi level. In this MIT, the states that are most susceptible to the localization, are those close to the band edge. Another aspect for Anderson MIT is the electron hopping between two localized states, technically known as variable range hopping [39].

2.5.2 Slater Insulator

The band theory gives a detailed answer for why a gap opens at the Fermi surface as a result of redistribution of the charge carriers within the band states. Slater examined this band insulator case and another case of electron-lattice interaction insulator, known as *Peierls Insulator*, and he was able to explain and predict another case of an insulating state [40]. This new state rises from electron-electron interaction, not electron-lattice interaction. In this interaction, a periodic modulation of the charge/spin spatial distribution is created within the lattice. These features are described as charge density wave (CDW), or spin density wave (SDW), and are responsible for the origin of an insulating state. Below the Slater MIT temperature T_{MI}, the spins are antiferromagnetically ordered with an opposite periodic potential through the nearest neighbors [41].

2.5.3 Mott Insulator

Mott and Hubbard model explains the existence of an insulating state in high temperature magnetic materials, above the Néel temperature[36]. This persistent insulating state is a consequence of the strong (e-e) Coulomb interaction between the electrons occupying the same orbital [42]. As a simple model, Mott considered a single electronic orbital sitting on each site of a lattice. The band accompanying the electronic orbital can be filled with two electrons, one with spin up and the other with spin down. Because of the (e-e) Coulomb interaction, this band will split into two bands separated by a gap. As an ideal example of such a model, consider a hydrogen lattice which has a lattice constant (a) and (L) sites. If all the sites were filled, then $N = L$ electrons and the band is half filled [41]. The electrons can hop between the neighboring sites with a probability t which is proportional to their kinetic energy W. This kinetic energy should overcome the energy $U = I - A$, which is the difference between the ionization and the electron affinity energies. The hopping electrons should have $W > U$, otherwise, a gap E_g opens at the single electron excitation spectrum and the size of this gap is comparable to the difference $E_g = U - W$. For $W >> U$ the single electron band is half-filled and gapless at the excitation spectrum. The charge excitation of an energy U and the removal spectrum of a charge from half-filled system results in what is called the upper Hubbard band (UHB) and lower Hubbard band (LHB) as illustrated in figure (2.11). These bands result from (e-e) correlation and are responsible for Mott MIT, which is different from the conventional band crossing.

Based on Mott's picture, the magnetic moment magnitude should not change much

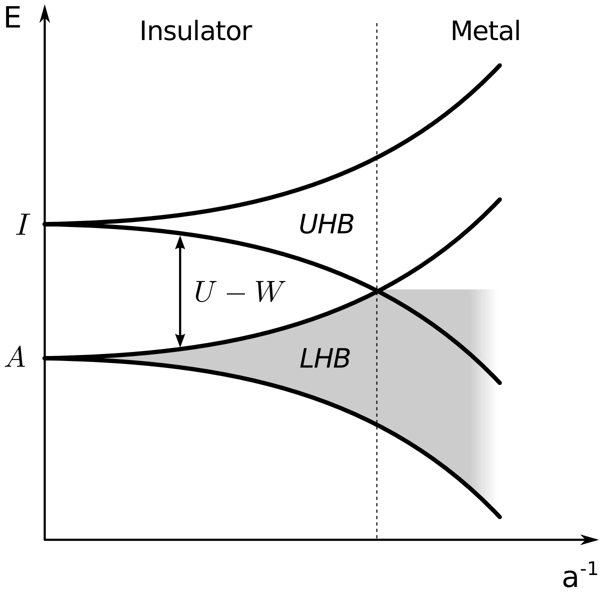

Figure 2.11: Illustration for Hubbard bands for Mott insulator as a function of the reciprocal interatomic distance a [14].

as the ordering temperature changes. This feature is counted as a distinguish between

Mott insulators and Slater insulators. Recently, some 5d TMOs, specifically iridates, have demonstrated another version of Mott insulator materials, this class of materials are identified as spin-orbit gap related Mott insulators, which describes the insulating state in the parent compound of this study.

2.6 Thermoelectric Effect

When there is a temperature difference ΔT between two points A and B in a normal conductor (see figure 2.12), the electrons diffuse from the hot region A to the cold region B. As these electrons flow, an electric current is created and eventually an electric potential difference ΔV_{BA} is established between these points, as schematically simplified in figure (2.12). In other words, the temperature difference ΔT has coupled to an electrical phenomenon and an electric potential difference ΔV_{BA} build up between the two points A and B. This coupling between the thermal and electrical phenomena is known as the $Thermoelectric\ Effect$ (TEE). There are three similar identified observations which belong to the TEE phenomenon:

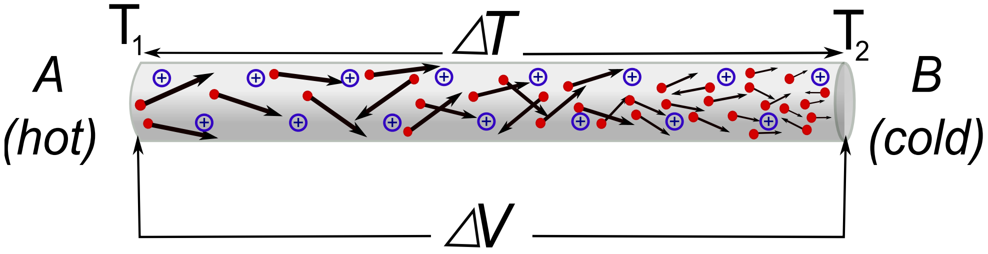

Figure 2.12: The thermoelectric phenomenon.

a) The Seebeck Effect: Seebeck effect was named in honor of the German physicist Thomas Johann Seebeck (1770-1831) who discovered the TEE in 1821. In such an effect, a temperature gradient along a conducting material creates a proportional potential difference.
b) Peltier Effect: which is the reverse of Seebeck effect, when an electrical current passes through a junction that connects two materials a heat emission or absorption occurs at the junction. This heat emission or absorption is a way to balance the chemical potential difference between the two materials.
c) Thomson Effect: in this case, a thermal current is generated because of the presence of a temperature gradient ∇T and an external electric current.

2.6.1 The Seebeck Effect

Consider a segment of a conducting material AB, as is shown in figure (2.12). The left side is at temperature T_1 and the right side is at temperature T_2 where $T_1 > T_2$. The Seebeck effect is the phenomenon in which an electric field $(\vec{E} = -\vec{\nabla} V)$ is induced in proportion to the temperature gradient $\vec{\nabla}T$; mathematically, this effect can be stated as [43, Volume1]

$$\vec{\nabla}V = S(-\vec{\nabla}T) \tag{2.32}$$

where S is called $Seebeck\ coefficient$ or alternatively $Thermoelectric\ Power$ (TEP). Because the side A at higher temperature T_1, the electrons in this end will be more energetic. The average velocity of the electrons υ_e is larger in this end, so these electrons start to diffuse toward the other end B of the temperature T_2. As a result, the end A eventually becomes positively charged and the migrated electrons accumulate at the end B, which then becomes negatively charged. This migration continues until a potential difference between the two ends A and B $(\varDelta V_{BA})$ is able to stop the electrons migration. In steady state, the energy per electron will be same at any point within the conductor, and as the total energy is conserved the energy per electron at the two ends A and B is given by:

$$\varepsilon(T_1) + eV(T_1) = \varepsilon(T_2) + eV(T_2) \tag{2.33}$$

$\varepsilon(T)$ is the electron energy at temperature T and $e = -1.6 \times 10^{-19}C$ is the electron charge. As $T_1 \to T_2$ and from equations (2.32) and (2.33) the Seebeck coefficient S can be expressed as:

$$S = -\frac{dV}{dT} \quad OR \quad S = \frac{1}{e}(\frac{d\varepsilon}{dT}) \tag{2.34}$$

where $\frac{d\varepsilon}{dT}$ is known as the specific heat per carrier. So, the Seebeck coefficient is the *entropy per electron.*

From equation (2.34) and as the entropy is always positive, the Seebeck coefficient sign is the same as the charge carriers sign, negative if the charge carriers electrons and positive if the holes are the carriers. The transport Boltzmann equations should be considered in order to understand the physics of Seebeck coefficient. For the electrical current density $\vec{j}$ and the thermal current density $\vec{q}$ these equations can be written as[43, Volume1]:

$$\vec{j} = e^2\hat{K_0}\vec{E} + \frac{e}{T}\hat{K_1}(-\vec{\nabla}T) \tag{2.35}$$

$$\vec{q} = e\hat{K_1}\vec{E} + \frac{1}{T}\hat{K_2}(-\vec{\nabla}T) \tag{2.36}$$

Where $\hat{K_n}$ is a second rank tensor coefficient defined as:

$$\hat{K_n} = \frac{1}{4\pi^3}\int(-\frac{\partial f_0}{\partial\varepsilon}) \mid_{\varepsilon-\varepsilon_k} \vec{v}_{\vec{k}}\vec{v}_{\vec{k}}\tau(\varepsilon_k - \mu)^n d^3k \tag{2.37}$$

here, $f_0 = \dfrac{1}{\exp[\dfrac{\varepsilon_k - \mu}{k_BT}] + 1}$ is the Fermi-Dirac distribution function at equilibrium, ε_k is the eigen energy of the momentum vector $\vec{k}$, $\vec{v}_{\vec{k}}$ is the group velocity operator($\vec{v}_{\vec{k}} = \frac{1}{\hbar}\nabla_{\vec{k}\varepsilon\vec{k}}$), μ is the chemical potential, τ is the scattering time (time scale of the dissipation of the system), and k_B is Boltzmann constant.

In case of a simple system, such as a cubic crystal, all the parameters reduce to scalar quantities and the physical quantities are given by:

$$S = \frac{1}{eT}\frac{K_1}{K_0}, \tag{2.38}$$

$$\sigma = e^2 K_0, \tag{2.39}$$

$$\kappa^{\backprime} = \frac{K_2}{T}. \tag{2.40}$$

Here, σ is the electrical conductivity, and $\kappa^{\backprime}$ the thermal conductivity in absence of an electric field $\vec{E}$.
For the open circuit condition of ($\vec{j} = 0$) and the absence of an electric field $\vec{E}$, which is the case when measuring the electron thermal conductivity, the thermal current density $\vec{q}$ of equation (2.36) becomes:

$$\vec{q} = S^2\sigma T\vec{\nabla}T - \kappa^{\backprime}\vec{\nabla}T = \kappa^{\backprime}(1 - \frac{S^2\sigma}{\kappa^{\backprime}})(-\vec{\nabla}T) \tag{2.41}$$

From this equation it is clear that the Seebeck coefficient is a quantity that is related to the electrical conductivity σ and the thermal conductivity $\kappa^{\backprime}$. In a real experiment the conduction electron thermal conductivity κ is described as:

$$\kappa = \kappa^{\backprime}(1 - \frac{S^2\sigma}{\kappa^{\backprime}}) \tag{2.42}$$

The second term $\frac{S^2\sigma}{\kappa^{\backprime}} \ll 1$ and can be neglected for conventional materials and set $\kappa = \kappa^{\backprime}$, but for the TEE materials this term is important as it is related to what is called *The figure of merit.*

Chapter 3 EXPERIMENTAL TECHNIQUES

In this study, we applied a number of experimental techniques to study the properties of the systems. These properties include structure and composition, magnetic, transport and thermal properties. The instruments and facilities used for this task and the methods implemented are introduced in the subsequent sections of this chapter. Most of these facilities are available in the laboratory of Professor Gang Cao, the novel electronic materials lab in the Department of Physics and Astronomy at University of Kentucky. This lab is one of the few labs in U.S. in which the materials synthesis capabilities and characterization facilities are under the same roof. To the best of our knowledge, no previous systematic studies have been made to characterize the physical properties of the systems $BaIr_{1-x}Ru_xO_3, (0 \leq x \leq 1)$ and $BaIr_{1-x}Rh_xO_3$, in form of bulk single crystals.

3.1 Samples Synthesis

The synthesis of high quality single-crystals is of great importance for material science research, as well as for advanced technology and application. There are a number of modern methods and techniques that are applicable on an industrial scale for materials production, and others that are used for small-scale synthesis in different areas of materials research. In general, the control of optimized synthesis of novel materials is coupled to the discovery and control of their new properties. For crystal growth in this lab, there are two different approaches; (a) the floating zone method and (b) the self-flux method of crystal growth. The latter is primarily used for the sample synthesis in this study.

Self-Flux Method: The Flux method is a common technique in the field of single-crystal growth. In this technique, the single-crystal growth starts at temperature range below the melting temperature of the raw materials. The advantage of using fluxes in addition to the raw salts is to form a molten at lower melting temperature that provides homogeneous medium for the crystal growth process. Because the growth starts at a temperature well below the limit of a solute phase temperature, the flux method is of a great preference over many other methods of single-crystal growth. In the molten flux, the growth process starts by forming tiny nuclei that become the seeds for the single-crystal growth. The resultant single crystals seem to be free of defects and growth strains and are of a high quality. Another advantage for the flux method technique is that it is not complicated and does not require sophisticated machinery. The basic and important part in this technique is a furnace with stable and homogeneous temperature control which can provide precise temperature gradient. This means that the technique can be implemented in any level of research and at the least available space in a small lab .

The phase diagram shown in figure (3.1) illustrates the crystalline temperature ranges as a function of the solute concentrations for fluxed melts. This phase diagram summarizes the optimum conditions that help maintain continuous desirable

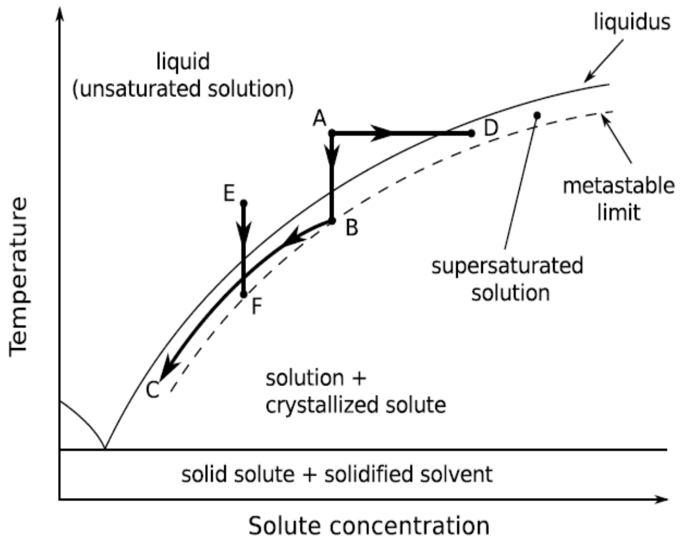

Figure 3.1: The binary phase diagram for solid-solution equilibrium and optimum conditions for achieving continuous crystallization rates from fluxed melts by: ABC – slow cooling, AD – evaporation, EF – temperature gradient transport [27].

growth rates, and the importance of the equilibrium within the solution in terms of the solubility level. The liquidus line, on the binary phase diagram, represents the solubility limits to be considered. This process describes the equilibrium between the solid and the solution within the solubility limits:

$$A_{solid} \rightleftarrows A_{solution} \tag{3.1}$$

where A is the desired process of solution-solid reaction.
The solid line in the phase diagram, liquidus line, divides the temperature range into two regions; saturated region below the line and unsaturated region above it. The solute starts to nucleate spontaneously through the medium or on the crucible's wall surface. As a result, the solution becomes less saturated locally, which switches the reaction to the other side of the equilibrium boundary. For constant and continuous crystallization growth, the system needs to be kept within the narrow region of metastable phase. The narrow region is bounded between the liquidus line, solid line, and the minimum saturated level, dashed line, as shown in the phase diagram figure (3.1). Path ABC, which is a slow cooling path, is the most common mechanism that applies to satisfy the metastable condition. If the system follows the path BC, which is within the metastable region, the tiny formed nucleus starts to attract other small clusters. As a result, the crystallization growth process is established. The path

BC is characterized by continuous slow cooling and supersaturating concentration decrease. Therefore, it is preferable a path for crystal growth to obtain large-size crystals.

For this study, the single crystals of the hexagonal perovskite systems, $BaMO_3$, (M = Ir and Ru), were grown using self-flux techniques. The raw materials for the systems are off-stoichiometric quantities of $BaCO_3$ and MO_2, (M = Ir or Ru), in addition to $BaCl_2$ as a flux agent . In the case of $BaIrO_3$, after grinding the raw materials using pestle and mortar, the samples were synthesized at temperature of 1280^0C followed by slow cooling rate of $3^0C/h$ [16]. For $BaRuO_3$, the ground materials were put in Pt crucibles and heated up to 1480^0C for 25 h, then cooled slowly to 1350^0C followed by rapid cooling to room temperature [6]. The single crystals of the doped studied systems, $BaIr_{1-x}Ru_xO_3$ and $BaIr_{1-x}Rh_xO_3$, were grown also from off-stoichiometric quantities of IrO_2, RuO_2 or RhO_2, $BaCO_3$, and $BaCl_2$ using self-flux techniques. The ground mixtures of powders were melted at 1470 ^{o}C in partially capped platinum (Pt) crucibles. The melt was left at the latter temperature for more than 20 hours and then left to cool down slowly at 2 ^{o}C/h to reach 1400 ^{o}C. At this point, the crucible was brought to room temperature through a rapid cooling at a rate of $\sim$ 100 ^{o}C/hour. The resultant samples are high-quality large-sized ($1 \times 1 \times 0.5\ mm^3$) single crystals, which possess well distinguishable crystallographic features with the c-axis along the shortest dimension.

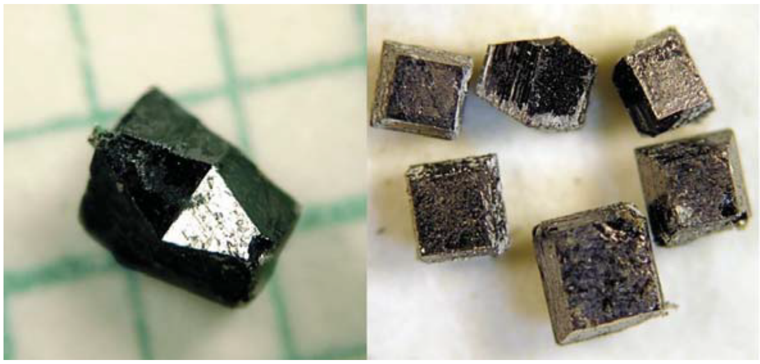

Figure 3.2: Examples of single crystals grown by self-flux technique, ($1\times1\times0.5\ mm^3$).

3.2 Sample Characterization (X-ray and EDX)

Structure determination and chemical composition analysis are the first analyses to be done after the synthesis and growth of single crystals, for the reason that the results obtained from these analyses are the direct confirmation of whether a desired phase was made or not. XRD, for structure determination, and energy dispersive x-ray (EDX) spectroscopy, for the chemical composition analysis, are the techniques were used to perform the assessment. Powder (XRD) was run on a ground small piece of the single crystal to check the accuracy of phase. A more detailed study for the crystal structure was performed using single-crystal XRD. The latter provides information about the changes of the crystal structure parameters such as lattice parameters, bond length and angles, and allows an assessment of the uniformity of stoichiometric distribution of doping elements.

Powder XRD study:

In Cao's lab, we use a high resolution diffractometer from Scintilla X1 (USA), in which the x-ray tube generates Cu Kα x-ray of wavelength ($\lambda = 1.5418 \mathring{A}$) and the detection unit is a liquid-nitrogen cooled germanium solid state detector element [30]. The goniometer in this system designed as $\theta - 2\theta$ configuration in the horizontal plane. In this design, the x-ray tube remains stationary and the incident angle of the x-ray beam is scanned by rotating the sample itself, whereas the sample holder rotates around the same axis as the detector unit. The sample holder rotation is coupled to the detector rotation through a mechanical set-up in which the angular motion of the detector is twice the sample holder rotation, as shown in figure (2.5) where the two coaxial rotation motions are illustrated. For powder XRD measurements, the sample which is a tiny piece of polycrystalline material or single-crystal fragment is ground in form of fine powder. The fine powder is then stuck to the surface of a single-crystal quartz plate, on the sample holder stage, by a drop of ethanol. The single-crystal quartz plates are designed to have a zero background scattering. After specifying the scan parameters, which include the tube power, the slit size, the angles range, the increment step, the time per step, and scan function, the scan is run then the collected data is saved for post analysis. Figure (3.3) shows a photograph of the powder XRD measurement stage with the tube, detector, goniometer and the sample holder. To identify the phase, the collected scan data can be compared with the phase identification database from the International Centre for Diffraction Data (ICDD) [44].

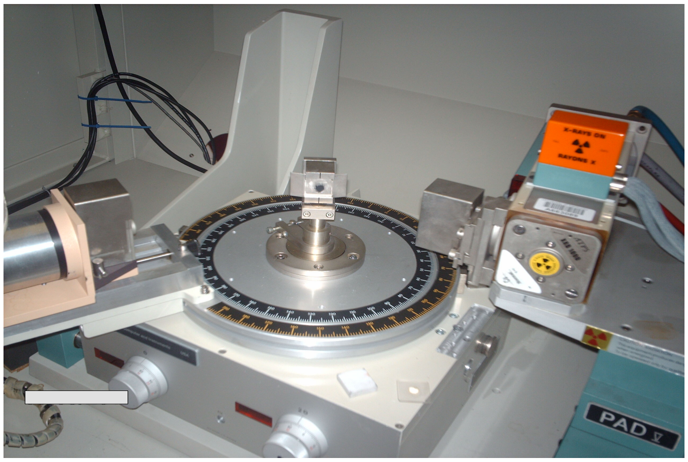

Figure 3.3: Powder XRD diffractometer stage with the tube (right), detector (left), and the goniometer and sample holder (middle).

Single-Crystal XRD study:

Single-crystal XRD is very important, especially when working with new compounds, it provides more details to identify the material crystal structure. The x-ray facility of the Department of Chemistry offers a number x-ray systems for different purposes. In this work, we utilized the single-crystal Kappa CCD diffractometer manufactured by Nonius (Delft, The Netherlands). It uses the Kα emission of a Mo-based x-ray source and a four circle Kappa goniometer, which is different from the classic four circle goniometer design. The machine occupied with temperature control option and measurements can be run within a wide range of temperatures from 90 K up to 400 K. The crystal structure of $BaIr_{1-x}Ru_xO_3$ single-crystal samples was determined using this diffractometer. The preferred single-crystal XRD samples should be of a regular shape and with distinct directions. The proper size of such samples should be of the range of 50 - 100 μm, but it depends on the chemical composition of the sample. The important interactions that should be considered, when choosing the needed sample size, are the absorption of x-ray photons by the sample composition and the scattering intensity because of diffraction. After choosing the proper size and shape, the sample is mounted on the tip of very thin plain old glass fiber using a sticky drop of organic oil. For our measurements, polyisobutene oil was used as the sticky oil. This oil has the desired requirements; it has low optical distortion during x-ray diffraction measurement, becomes amorphous material after solidification at low temperature, and it should behave as a low scattering power material [45] [46]. Then, the sample on the thin fiber is attached tightly to a copper mounting pin that is designed in certain shape to fit in with a magnet on a micro-goniometer head. The micro-goniometer head has adjustable screws, in all directions, x, y and z, for the proper positioning for the sample. There is a video camera attached to the goniometer stage to monitor the sample position and perform any post adjustments after rotating the goniometer about different axes. During single-crystal XRD data collection session, the x-ray beam spot directed toward the sample and a number of reflections are recorded by the detector unit. The goniometer axes rotate with a specified increment, through the three angles χ, κ and ω, within the selected range. In each step, the different reflections from the sample is recorded and saved. The pattern of x-ray reflections from the sample are captured through the Charge-Coupled Device (CCD) image sensor. The extracted information from the reflection pattern, in addition to the XRD knowledge, diffractometer geometry and the sample chemical information, are used as inputs for structure solution procedure to find out the atomic coordinates and their composition, etc.. Then a crystal structure refinement is performed by full-matrix least squares calculations using SHELX-97 software package [47]. During refinement calculation, user has to specify and determine many of the crystal structure information, including atom coordinates, sites occupancy, and crystal structure coordinates, etc. The occupancy factor of oxygen site is another important piece of information to check the uniformity of structure and stoichiometry of a compound.

Scanning Electron Microscope and Energy-Dispersive X-ray (SEM/EDX) study:

Scanning electron microscope (SEM) and energy-dispersive x-ray (EDX) spectroscopy are powerful tools for material characterization that become more popular during the last few decades. The SEM was used to check the shape details and dimensions of the single-crystal samples. The principle mechanism in EDX is based on detection of characteristic x-ray photons from an excited small spot of the studied materials using an energetic electron beam. These electronic transitions between the different electronic levels are quantized in nature. A specific transition from an excited state to ground state is accompanied by emission of characterized photons in the range of x-ray spectrum. This emitted characterized radiation is an identifying feature of the element being involved in the interaction. The radiation energy is related to the energy difference between an excited state and ground state. This difference is a function of the atomic number Z. Moseley's relation, given by equation (3.2), describes the dependence of the characterized emitted wavelength, or energy, on the atomic number Z.

$$\lambda = \frac{B}{Z - C^2} \tag{3.2}$$

Here B and C are constants and are different for different set of emissions. Plotting this relation for different sets of transitions helps in construct a qualitative understanding for different elements (different Z's).

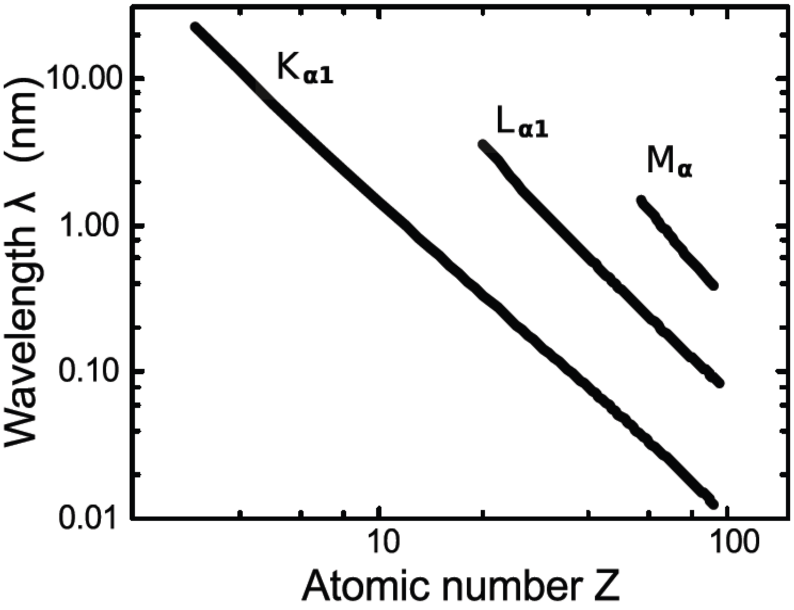

Figure 3.4: Moseley's relation between λ and Z for the $K_{\alpha 1}$, $L_{\alpha 1}$ and M_{α} characteristic x-ray lines [49].

EDX test was run to confirm the 1:1 ratio of Ba to Ir, or Ba to Ir+Ru(Rh) and the uniformity of stoichiometric distribution. The EDX chemical composition analysis of single crystals of the hexagonal perovskites, or the $BaIr_{1-x}Ru_xO_3$ and $BaIr_{1-x}Rh_xO_3$ systems, were performed using a combined unit of Hitachi/Oxford SwiftED 3000. It is a compact design of TEM/EDX unit. The EDX system uses a silicon drift detector (SDD) with an integrated Peltier element, which are free cryogenic liquid cooling detectors. These detectors have high precision and more sensitive. They can operate at very high-count rates for energy dispersive x-ray (EDX) spectroscopy. These EDX tests confirmed the desired stoichiometric compositions of the samples.

3.3 Magnetization Measurement

The magnetic properties measurements for the studied systems were performed using the Magnetic Property Measurement System (MPMS), from Quantum Design (California, USA). The MPMS is designed to utilize the flux magnetometer method. In this system, a high sensitive probe is used to detect the magnetic field lines "flux" and its change from magnetic material. The probing unit in the MPMS® is a high sensitive device known as *SQUID, Superconducting QUantum Interference Device*. Robert Jaklevic and his colleagues at Ford Research Labs invented this technique in 1964. The MPMS® detection system is schematically illustrated in figure (3.5). The illustration shows the main components of the system; the sensing coils, a radio frequency interference (RFI) shielded superconducting transformer and a SQUID sensor[50]. The set of pick-up, sensing, coils is the unit that detects the change in the magnetic flux due to a sample motion, up and down, through the chamber. These coils are sensitive and are calibrated to detect the sample magnetic flux and exclude any other external, from the surrounding environment or background, uniform magnetic fluxes. To enhance the signal from the sample, an external magnetic field produced by the superconducting magnet was applied to magnetize the sample. In the RF-transformer, switching between superconducting and normal states is executed during all magnet charging procedures and at the beginning of sample

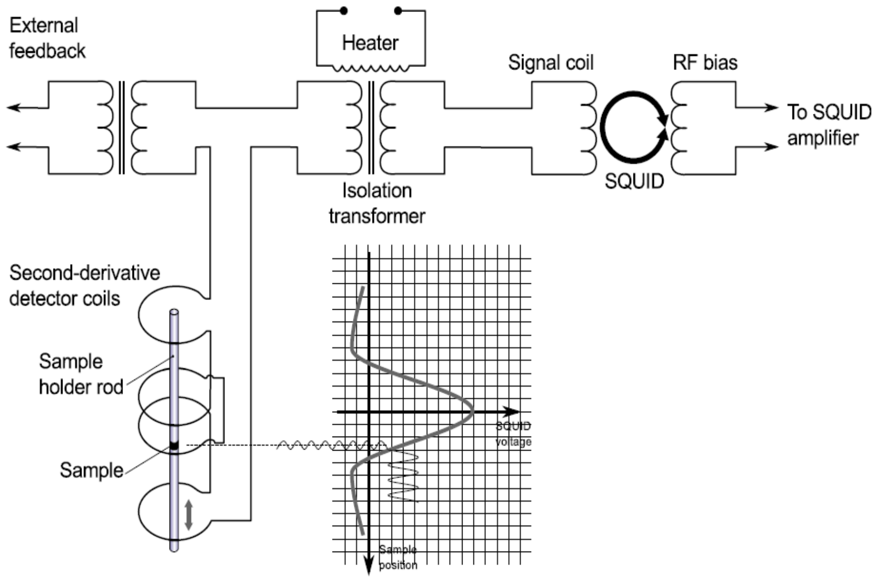

Figure 3.5: Schematics of SQUID magnetometer with longitudinal pick-up coils [51].

initialization [51]. The SQUID sensitivity, in principle, is based on a phenomenon known as Josephson effect. The phenomenon reflects the phase coherence behavior of Cooper pairs as they tunnel an insulating barrier (the Josephson junction), between two superconductors. The $AC\ Josephson\ effect$ makes the Josephson junction acts as an ideal voltage-to-frequency converter [52, 53]. Schematic illustration of DC-SQUID is illustrated in (3.6).

Figure (3.7) shows a schematic illustration of the sample chamber location inside the $MPMS^{®}$ dewar. The chamber is enclosed by the surrounding superconducting magnet which is located inside the central part of the dewar. The superconductor magnet is submerged in a liquid helium bath, see figure (3.7). The liquid helium has two roles. First, it is the coolant medium for the superconductor magnet to function properly. Second, it is the temperature transmission medium during the operation. The flow of the liquid helium, around the sample space, serves as the temperature control mechanism of the sample chamber. In addition, there is a set of built-in heaters and thermometers for more accurate and precise temperature control. The temperature control units are able to sweep the sample temperature within a wide range of temperatures, from 1.7 K up to 400 K. The temperature range can reach 800 K using an optional high-temperature insert. The superconductor magnet can provide highly precise magnetic fields within the range of -7 Tesla up to 7 Tesla and increment steps as small as 0.005 T/min [54].

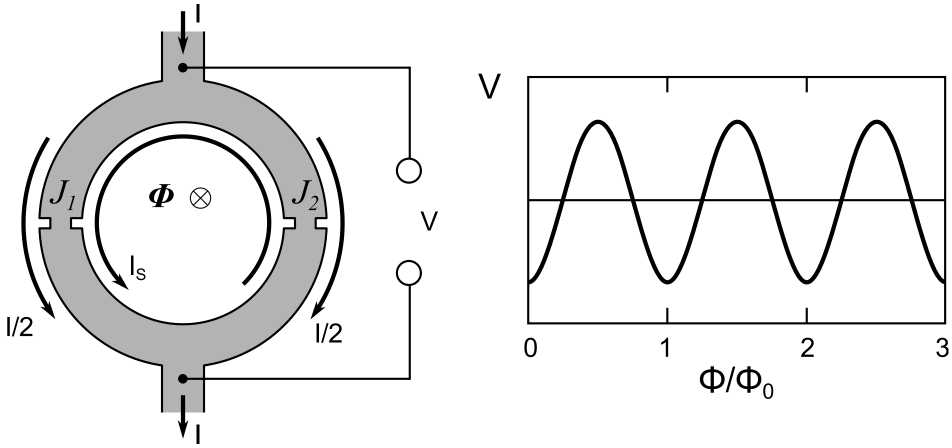

Figure 3.6: Illustration of DC-SQUID and V($\frac{\Phi}{\Phi_0}$) for constant bias current I. Here I_s screening current, V voltage across SQUID, Φ external magnetic flux, Φ_0 magnetic flux quantum.[51].

In conventional magnetization measurements procedure, a single-crystal sample was mounted at the middle of a tin uniform quartz rod. This quartz rod is a nonmagnetic material (SiO_2, is weakly diamagnetic material) [55] that is charactrized by dimensions of about 1 mm in diameter and 12 cm in length, which assures uniformity and cancellation of any magnetic background while the sample passing though the pick-up coils. The mounting material of the sample to the quartz rod should be a nonmagnetic material too. The best choice to serve this task, and commercially available,

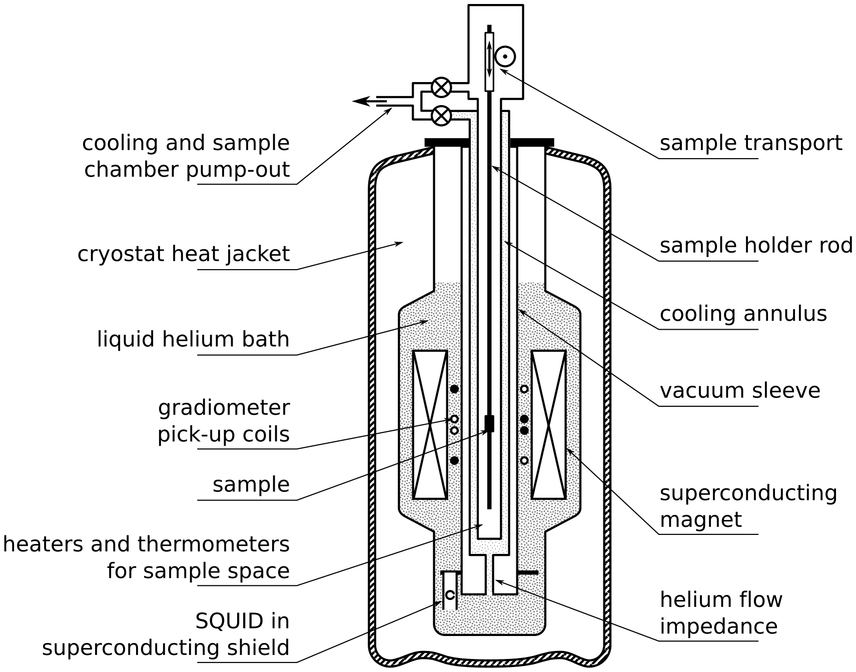

Figure 3.7: Longitudinal cross-section of $MPMS^{®}$ Dewar [51].

is the thermoconducting varnish VGE-7031 [56]. The mounting of the sample to the quartz rod should perform with respect to one of the crystallographic axes of the single-crystal sample. The mounting of polycrystalline sample would be different. In this case, the sample, which is a fragment of polycrystalline pellet, is packaged inside a gelatin capsule or wrapped in a piece of clear plastic. Then, the capsule is secured in the middle of a long clear plastic (polypropylene) drinking straw. The straw should be also of nonmagnetic material [51]. To insert the sample, with the quartz rod or straw, inside the MPMS dewar, it was attached to the end of the MPMS drive rod that leads the sample into the sample chamber. Before running the measurement, the transport option of SQUID system was initiated and the sample was centered within the pick-up coils.

3.4 Electrical Resistivity Measurement

Both AC- and DC-current resistivity measurement techniques can provide detailed information about the charge carrier's behavior inside the material. The widely used method in such measurements is the 4-wire configuration, or four-point probe method. In this method, both current and voltage meters are used and the two pairs of contact wires are attached to the surface of the sample using fine gold leads. Schematic illustration of the equivalent circuit is shown in figure (3.8). First, the sample need to position in the most temperature stable region of a cryostat for low temperature measurements (or a furnace for high-temperature measurements). These requirements cause an increase in the length of the connecting wires and in turn increase their resistance in the measured response of the sample. In certain cases, the contacts resistance may dominate and obscure the measured response of the sample itself, especially for variable temperature conditions. The four-point probe technique helps to overcome most of the afore mentioned problems. As shown in figure (3.8), the circuit configuration is a series loop; therefore, the electric current is the same through all elements. The voltmeter's impedance is sufficiently high and a negligible current passes along its wires. Thus, the resistance of the wire leads and contacts is excluded during the potential difference measurements. The resistivity of the sample was calculated using the measured resistance value (R) and geometrical dimensions of the sample; the cross-section area A and the length L.

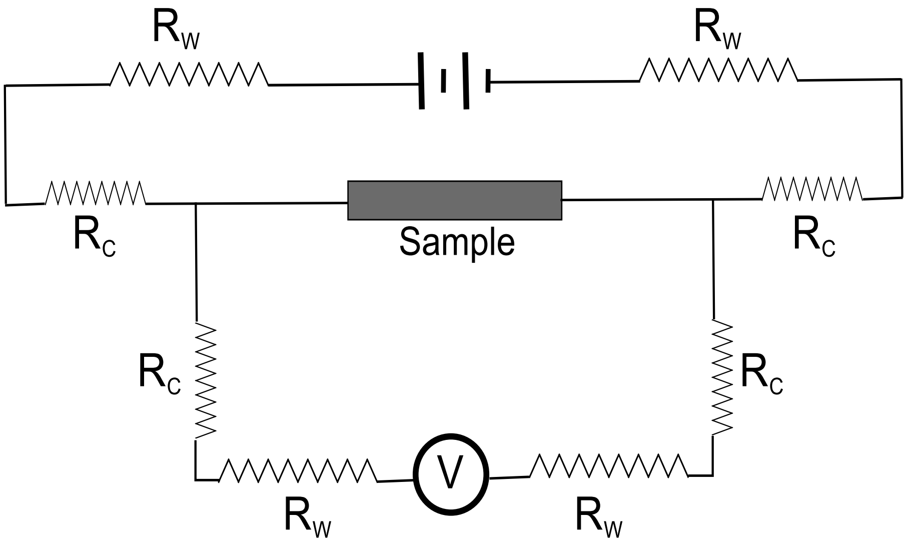

Figure 3.8: The equivalent circuit of the four-point probe technique for electric resistivity measurements; R$_W$ stands for the connecting wire resistance, R$_C$ stands for contact point resistance.

$$\rho = \frac{R \cdot A}{L} \tag{3.3}$$

Certain technical requirements have to be considered in order to have a clean reasonable response. Among these requirements are the bonding material between the leads and the sample, the leads shape and size, and the environment where the measurement is performed. For most of electrical resistivity measurements in our lab, one of two typical compounds are used for electrical leads attachment. One is a two-component solid silver-filled epoxy EPO-TEK® H20E, from Epoxy Technology Inc.[57]. The other is carbon paint Dotite XC-12 from Fujikura Kasei Co. [58]. The electrical lead is a gold wire of diameter 0.001" that attached to the sample and connected to the sensing wires of the instrument. The sample was mounted on a sample holder using highly thermoconducting adhesives, such as phenolic varnish VGE-7031 from General Electric [56] for low temperature measurement, or an aluminum nitride ceramic adhesive Ceramabond™ 865 from Aremco Products Inc. for the higher temperature range; up to 900 K [59]. For AC-resistivity measurements, LR-700 resistivity bridge from Linear Research Inc. was used. This setting is adequate to cover resistances measurements ranging from few $n\Omega$ (nano ohms) up to 2 $M\Omega$ (mega ohms) [60]. The LR-700 bridge can be set to generate a very small excitation current, of nano ampere range, and at very low frequency of 16 Hz [60]. The low-current and low-frequency setting has the advantage of minimizing the dissipated power and eliminates self-heating problems within the sample. Second, for DC-resistivity measurements, we used a setting of highly sensitive nano-voltmeters, model 2182, and a DC-current source, model 2400 source meter or the model 6220 current source [61], from Keithley Instruments (USA). The current source generates a square wave of excitation signal that oscillates three times between I_{max} and $-I_{max}$ per single data point. The average resistance at a given point is calculated according to formula (3.4).

$$\langle R \rangle = \frac{(V_1 - 2V_2 + V_3)}{4I_{max}} \tag{3.4}$$

V_n is the voltmeter reading at each peak current value I_{max} for three cycles at each data point [61]. As mentioned earlier, the resistivity measurements in our lab can be extended within a broad range of temperatures. A custom transport measurement probe for the standard Quantum Design MPMS® cryostat serves for the sub-ambient temperature range of 1.7-400 K and external applied magnetic field up to 7 Tesla [51]. A wider temperature range of 10-900 K was covered using a custom design, the Displex pneumatic closed cycle cryocooler (DE202), from Advanced Research Systems (Macungie, Pennsylvania), equipped with high-temperature interface [62].

3.5 Thermoelectric Power Measurement

In this study, we utilized the high temperature option installed in a closed cycle cryocooler from Advanced Research Systems, inc. (ARS- Allentown, PA USA), to measure the thermoelectric power of the studied samples. This design, as shown in figure (3.9), employs the dynamic two-point method. The sample was clamped between two copper pins mounted on the sample holder stage. The pins are mounted on the stage using electrically insulating, heat conducting cement. The temperature gradient along one dimension of the sample was created using a resistive heater made out of Manganin wire and is wound around one of the copper pins. The thermoelectric potential was measured using two golden fine wires attached to the copper pins. The temperature difference was measured using a type E (chromel-constantan) differential thermocouple connected to the copper pins at closest point to the sample's ends, see figure ((3.9 b)). The sample holder was installed inside the chamber of the closed cycle cryocooler that occupied with the high-temperature option. The chamber was kept at high vacuum during the running of measurement. The tin-foil shield around the cold core and the sample holder stage is to eliminate any parasitic radiative heat from the surrounded environment. There is a number of control units connected to the setup of measurement as shown in figure(3.9a). The Model 2400 source meter from Keithley Instruments was used as the current source to power the Manganin

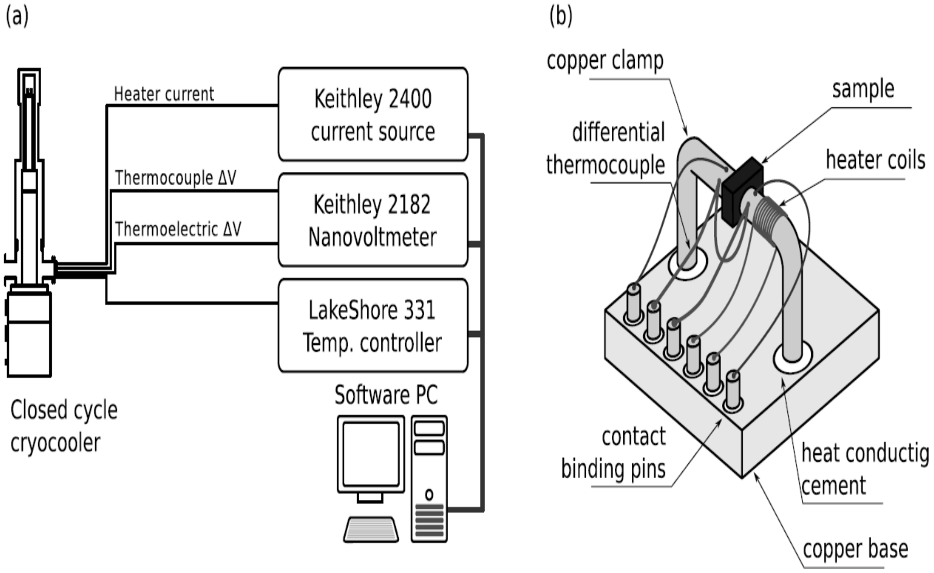

Figure 3.9: (a) Illustration of the thermoelectric power (TEP) measurement setup and the instruments; (b) schematic drawing of sample holder design [14].

pulse heater. The double-channel Model 2182 nano voltmeter, also from Keithley Instruments, measures the thermocouple signal and the thermoelectric potential difference simultaneously. The optimum values of the current I and the duration time τ to generate temperature gradient ΔT that is reliable to acquire reasonable response were determined empirically. The Model 331 temperature controller from Lake Shore Cryotronics [63] was the main unit for controlling the temperature of the system. The data acquisition and instrument control are coupled via a LabView program for automated run. The combination of the cryocooler and high temperature interface helps the setup in running TEP measurement within a wide range of temperatures from 12 K up to 650 K.

3.6 Heat Capacity Measurement

In this study, the heat capacity option of the Quantum Design PPMS® was used to measure heat capacity at constant pressure. This PPMS option can measure the sample heat capacity within a temperature range of 1.7 K up to 400 K. Also, we can apply a magnetic field up to 9 Tesla [64]. The heat capacity measurement using the PPMS option implements the relaxation time concept. This concept is common in many other techniques of heat capacity measurements. The technique involves a controlled mechanism of applying a heating signal to the sample and measure the change in the sample temperature as a function of time. A schematic representation of the

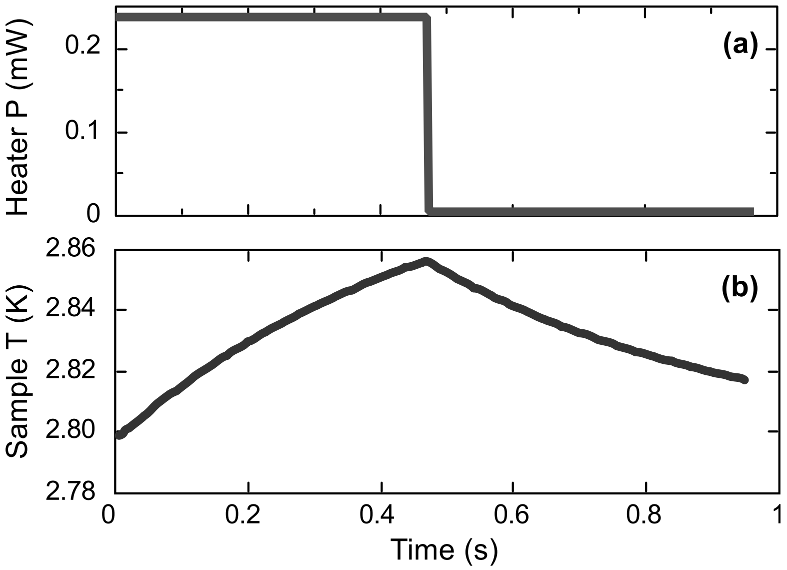

Figure 3.10: The change of sample temperature in a micro calorimeter, (a) due to a pulse of heat applied (b) as a function of time. The warming and cooling stages of the process of approximately equal duration are clearly distinguishable [64].

heating and cooling process as a function of time is shown in figure (3.10). The measured sample sets on the sample stage and surrounded by a spot of thermal grease. The stage connected to the system via four pairs of fine wires; two for the heater and two for the thermocouple, as illustrated in figure (3.11 b). Such configuration has the advantage of giving the sample-platform combination a large enough relaxation time (time-constant) to attain thermal equilibrium state. The sample space was maintained at high vacuum state of $\sim 10^{-6}$ Torr. The vacuum state ensures that thermal conductance between the sample platform and the rest of the sample puck is only through the metal wires. A mathematical model called two-tau model [64] [65], fits the heating-cooling process of the sample at each data point. This model stimulates the response of the sample for heat flowing between the sample and the sample platform. Equation 3.5 defines the two-tau model form and the related parameters.

$$c_p \frac{dT_p}{dt} = P(t) - \lambda_g (T_p(t) - T_s(t)) - \lambda_w (T_p(t) - T_0(t)) \tag{3.5}$$

$$c_s \frac{dT_s}{dt} = -\lambda_g (T_s(t) - T_p(t)) \tag{3.6}$$

Here c_p and c_s are the heat capacities of the platform and the sample respectively, $T_p(t)$ and T_s are the temperatures of the platform and the sample respectively. λ_g is the thermal conductivity between the two due to the grease. λ_w is the thermal conductance of the four pairs of the fine wires supporting the platform. A simpler model, defined by equation (3.7), is used to compare the results of the two-tau model with its results. The simple model assumes an ideal thermal contact between the

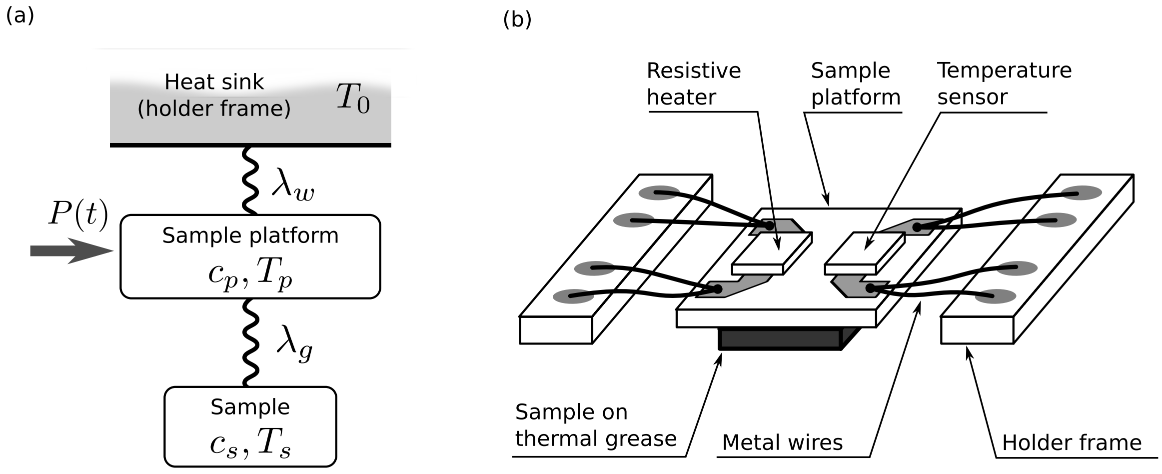

Figure 3.11: (a) Illustration of two-tau model for sample and sample holder; (b) schematic drawing of microcalorimeter sample holder design [14].

sample and the platform [64]. In some cases, the two-tau fitting fails to gives a correct result for the heat capacity measurement. These cases include the following; if the contact between the platform and the sample is very poor, if the thermal conductance of the sample is poor, or if the weight of the sample is very small compared to the platform, this is the most common to occur.

$$c_{tot}\frac{dT_s}{dt} = P(t) - \lambda_w(T_s(t) - T_0(t)) \tag{3.7}$$

In case of failure, the software of the heat capacity option considers the simple model result in order to overcome the fitting failure. In this case, the platform-sample coupling coefficient is considered 100 percent.
The heat capacity measurement, using the PPMS option, consists of two steps; First the user needs to measure what is called addenda data. The addenda are to measure the heat capacity of the system without the sample. In the addenda measurement, a small amount of thermal conducting grease is put on the surface of the sample platform. For room temperature and lower ranges, the type of grease used was vacuum grease Apiezon type N [66].The Apiezon type H [67] was used for higher temperatures range, up to 400 K. The small weigh issue of some samples can be overcome by installing several pieces of the same compound in the grease spot. This idea helps to achieve the needed overall weight and hence to have good thermal contact and adhesion with the platform. For a regular cleaning of the sample platform from used grease, toluene solvent was used as a degreaser [64].

Chapter 4 Magnetic, Transport, and Thermodynamic Properties of $\mathbf{BaIr_{1\text{-}x}Ru_xO_3}$ $(0 \leq x \leq 1)$

The first attempts to study the Ba based $4d$ and $5d$ TMOs started back in the 1950's and 1960's [68] [69]. Early on in these studies, it was noticed that $BaIrO_3$ and $BaRuO_3$ are both isostructural compounds of 9R perovskites [70]. The two compounds possess similar crystal structure, which is hexagonal perovskite, but with different lower symmetries due to the different distortions. Recent studies have confirmed that $BaIrO_3$ is a weak ferromagnet insulator with an ordering temperature of 183 K, while $BaRuO_3$ shows metallic-like behavior with unusual magnetic properties [6]. A number of studies have investigated different chemical substitutions for the $A-$ or $B-$ site in both of these compounds. These studies have shown that these systems are very susceptible for such substitutions and the magnetic and transport properties may change dramatically. This work modifies the composition of the $BaIrO_3$ compound under a systematic chemical substitution by Ru to gradually change the composition toward the other end, $BaRuO_3$, which can be expressed as $BaIr_{1-x}Ru_xO_3$ with $0 \leq x \leq 1$. The structure, magnetic, transport, and thermodynamic properties of the system have been investigated and the evolution of the ground state from one end to the other is analyzed. As a comparison, the Ru substitution was replaced by Rh substitution in the $BaIr_{1-x}Rh_xO_3$ system for a low level of doping (x $<$ 0.10).

4.1 Motivation for This Work

Iridates are a new class of magnetic insulators referred to as spin-orbit interaction induced Mott insulators [71]; $BaIrO_3$ is a good example of such materials. The spin-orbit interaction (SOI) is stronger in these materials, and the SOI energy becomes a comparable energy to the conventional (e-e) interaction. At the same time, (e-e) interaction is reduced in iridates because of the extended nature of d-orbitals, (see table 1.1). The reasonable explanation for the insulating behavior that was observed in many 5d iridates was first introduced by B. J. Kim et al [71]. This explanation can be simplified using the illustrations in figure (4.1). Based on the conventional band theory, 5d TMOs should behave like wide t_{2g} band metals as shown in part (a) of figure (4.1). The experimental observations contradict this picture and show an insulating behavior in many examples of these systems [17]. To open an insulating gap in the conventional picture, as pictured in part (b) of figure (4.1), requires a large (e-e) interaction energy $U \gg W$, which would not be realistic in the case of iridates. Part (c) shows that the introduction of considerable SOI in this model, about 0.4 eV in iridates [71], is able to split the degenerate t_{2g} into two bands; a fully filled $J_{eff} = \frac{3}{2}$ band, of lower energy, and a half-filled $J_{eff} = \frac{1}{2}$ band, with higher energy. Fermi level μ resides through the $J_{eff} = \frac{1}{2}$ band. This band is a narrow band and even the reduced (e-e) energy is able to open the Mott insulating gap, this is illustrated in part (d) of figure (4.1). In 5d iridates, SOI, Coulomb interactions U, tetragonal CEF and Hund's coupling become comparable interaction energies that vigorously compete

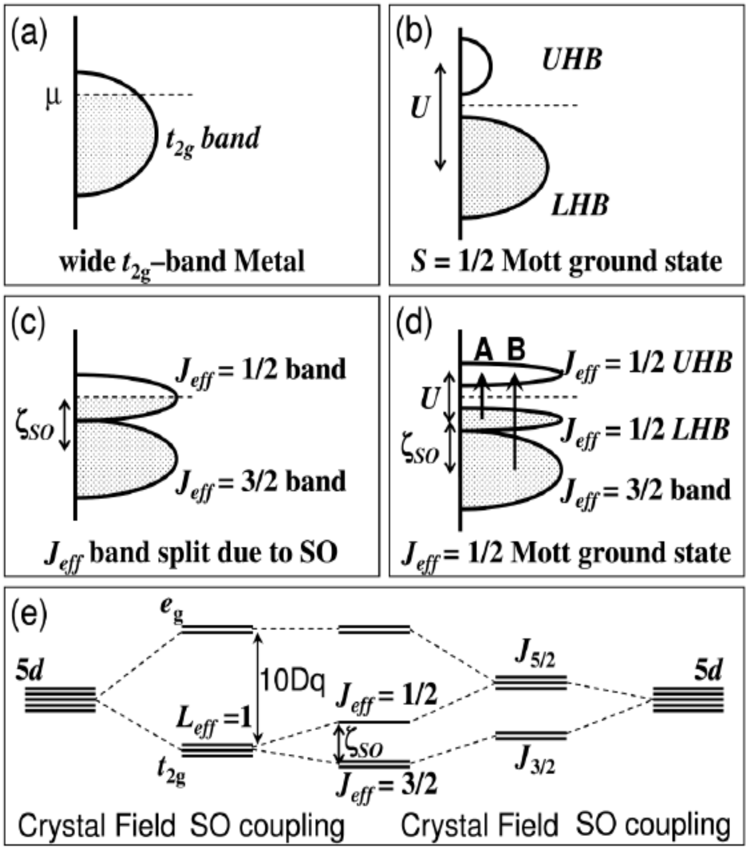

Figure 4.1: Schematic illustration for the electronic energy configuration of 5d-orbitals as they split because of CFE and SOI; (a) conventional band theory picture, without SOI and U, (b) splitting due unrealistically large U and without SOI, (c) introducing SOI as comparable interaction, and (d) introducing both interactions SOI and U, and (e) 5d energy levels splitting by CFE and SOI. [71]

with each other, and in turn, set a new balance between the relevant energies that can drive new exotic states. $BaIrO_3$ is a representative example of these 5d iridates; it is a weak ferromagnetic insulator that orders at 183 K. The Ir^{4+} ($5d^5$) ion has five 5d-electrons, four of them fill the lower $J_{eff} = \frac{3}{2}$ band, and one electron partially fills the $J_{eff} = \frac{1}{2}$ band. Nevertheless, the larger the SOI and the narrower the band is, the smaller U is needed for a SOI-related insulating state. In contrast, the $4d$ based $BaRuO_3$ shows a metallic-like behavior over a wide range of temperatures. The Ru^{4+} ($4d^4$) ion has four $4d$ electrons. It also experiences weaker SOI ($\sim 0.16\ eV$) because it has a smaller atomic number; $Z = 44$. The splitting due to SOI between $J_{eff} = \frac{1}{2}$ and $J_{eff} = \frac{3}{2}$ bands is smaller, hence, the electron filling should be more evenly distributed by the four 4d-electrons. The reduced SOI and more effectively screened Coulomb interaction (e-e) between $O - 2p$ and $Ru - 4d$ electrons are expected to give rise to such a metallic-like state. In addition, the compounds $BaIrO_3$

and $BaRuO_3$ share another important feature. Both of them are classified as 9L hexagonal perovskite materials [70]. $BaIrO_3$ has a $9M$ hexagonal layered structure and the crystal unit cell has the space-group $C2/m$ symmetry. $BaRuO_3$ has a $9R$ hexagonal layered structure with a unit cell shows the space-group $R\bar{3}m$ symmetry. The difference in their space-group symmetry is due to a difference in distortion of the $IrO6$ - or $RuO6$-octahedral within the unit cell. Because of the distorted structure in both compounds and eventually the difference in lower symmetries, both $BaIrO_3$ and $BaRuO_3$ have a larger unit cell as compared to an undistorted unit cell. This comparison reveals that the impact of the SOI strongly depends on other degrees of interaction and freedom, such as the Coulomb interactions and the lattice distortions and also related to the detailed band structure around the Fermi surface E_F [72] [73].

The clear contrast between these two compounds, in terms of their physical properties, emphasizes the critical role of SOI as an important driven interaction in heavy TMOs, such as $BaIrO_3$, $BaRuO_3$, and many other iridates. This contrast was the main motivation behind conducting this work. The first obvious notice here is the number of $d-$electrons; in the $Ru^{4+}(4d^4)$ ion there are four $4d$ electrons, whereas

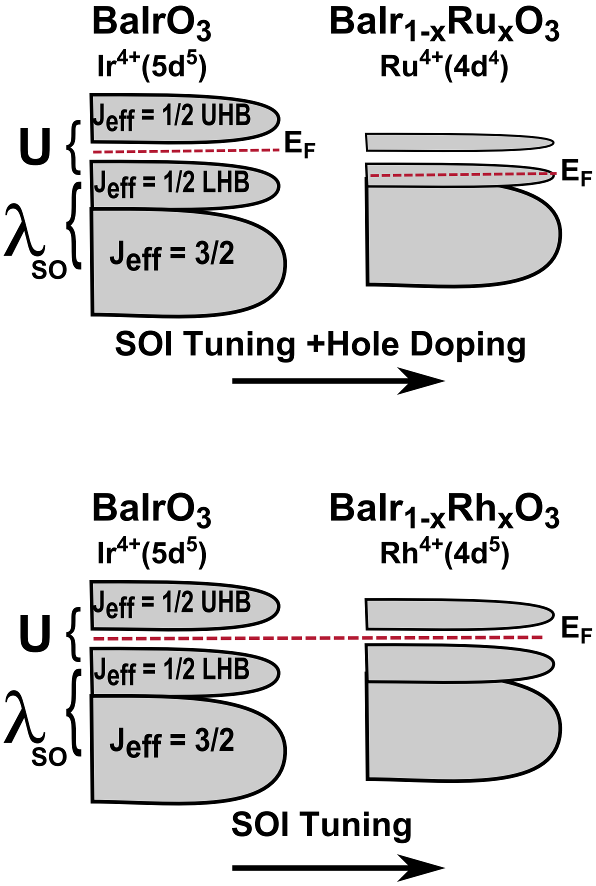

Figure 4.2: A schematic illustration for the effects of Ru and Rh doping on the splitting of $J_{eff} = \frac{1}{2}$ and $J_{eff} = \frac{3}{2}$ bands in iridates.

the $Ir^{4+}(5d^5)$ ion has five $5d$ electrons. Therefore, in addition to weakened SOI, the Ru doping is actually hole doping to the t_{2g} band. The $Rh^{4+}(4d^5)$ ion has the same number of d-electrons as the $Ir^{4+}(5d^5)$ ion (d^5); the Rh doping will just weaken the SOI in the system. In this work, the ground state of $BaIrO_3$ is manipulated via SOI reduction plus simultaneous hole doping. This manipulation is done by substituting $Ru^{4+}(4d^4)$ for $Ir^{4+}(5d^5)$ in single-crystal samples of $BaIr_{1-x}Ru_xO_3$ system, with $(0 \leq x \leq 1)$. An illustration of Ru substitution effect on the $J_{eff} = \frac{1}{2}$ and $J_{eff} = \frac{3}{2}$ bands splitting is shown schematically in figure (4.2). The Ru substitution with a weaker SOI clearly reduces its role and minimizes the splitting between the $J_{eff} = \frac{1}{2}$ and $J_{eff} = \frac{3}{2}$ bands. At the same time, the hole doping of Ru substitution in t_{2g} bands lowers E_F, and as a result the system moves away from the instability of the Mott insulating state. Ru doping systematically drives the system to a robust metallic state. The doping profoundly alters the balance between the competing local energies, namely, the SOI is weakened, while the tetragonal CFE and the Hund's coupling are enhanced. On the other hand, the $4d$ Rh substitution, in the $BaIr_{1-x}Rh_xO_3$ system, also weakened the SOI. The $4d$ electrons become more susceptible to perturbations but without changing the band structure and population. The anticipated underlying effects of Rh doping on the $J_{eff} = \frac{1}{2}$ and $J_{eff} = \frac{3}{2}$ bands are also schematically illustrated in figure (4.2). In the case of Rh doping, the mismatch in energy between the Ir ion sites and the Rh ion sites creates a disorder state in the system [74]. Therefore, the disorder scattering becomes the dominant mechanism as Ir/Rh substitution increases, and the disorder gives rise to a localization. In turn, it preserves the insulating behavior and the system is still tuned at the Mott instability.

Former systematic studies of $A-site$ substitution in the parent compound $BaIrO_3$ have also been conducted in our group. These studies investigated systems that are represented by $Ba_{1-x}A_xIrO_3$ composition, with $A = Sr$, or rare earth element (Gd or Eu) [75]. The concluding result from these studies is that a dilute substitution, x = 0.12 for Sr, x= 0.04 for Gd, and x = 0.02 for Eu,can recover a partial metallic state in these systems. A full paramagnet metallic state is observed at higher concentrations. The substitution of the smaller sizes of these cations has drastic impact on the system magnetic and transport behavior, within a wide range of temperatures. This trend identifies that $BaIrO_3$ is an example of material that lives on the borderline of metal-insulator transition state. This state is very sensitive to crystal structure perturbations, such as contraction or deformation [16].

4.2 BaIrO$_3$ System

4.2.1 Crystal Structure

At room temperature $BaIrO_3$ is a $9M$ hexagonal perovskite with a monoclinic distortion. The unit cell of this phase has a symmetry of the space-group $C2/m$. The monoclinic distortion within the unit cell features the formation of Ir_3O_{12} trimers along c-axis, as shown in figure (4.3 a). The single trimer consists of three face-sharing IrO_6 octahedra. The trimers are connected by their top and bottom corner-sharing IrO_6 octahedra along the c-axis, see figure (4.3b). This shape gives $BaIrO_3$ a quasi one-dimensional ($1D$) chain structure along the c-axis. The Ba cations are accommodated at interstices between these chains. The trimers are twisted and experience buckling because of the monoclinic distortion and relatively large Ba cation size. This buckling causes tilting to the trimers with an angle of about 13° between the trimers long axes as shown in figure (4.3b) [76]. This alternative tilting makes the trimers form zigzag-shaped chains. The tilting of the trimers results in forming a two-dimensional (2D) layer in ab-plane, which consists of corner-sharing octahedra. These two distinct structures, 1D along c-axis and 2D in ab-plane, are reflected in observed anisotropy of transport and magnetic properties of this iridium oxide. The complex structure of this phase initiates two different interactions between the iridium ions; a direct exchange interaction for the face-sharing octahedra within the trimer, which is the $Ir-Ir$ bond, and an indirect exchange interaction for the corner-sharing octahedra between the trimers, this is the $Ir-O-Ir$ bond.

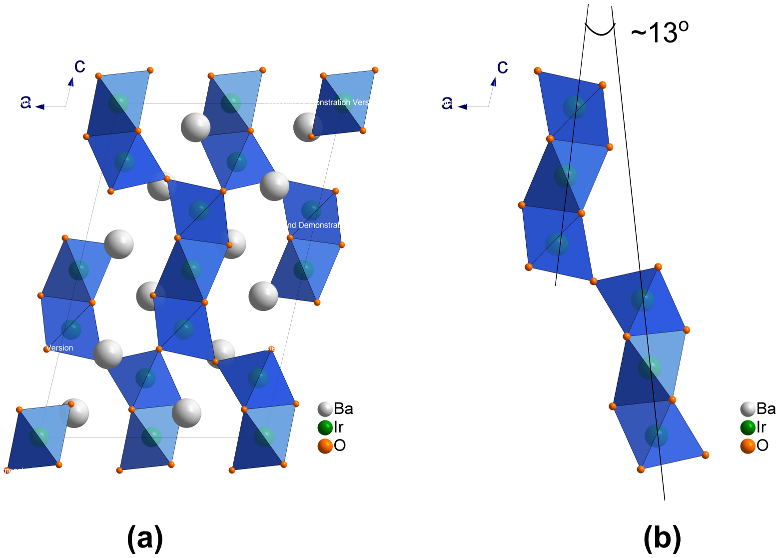

Figure 4.3: The hexagonal perovskite structure of $BaIrO_3$ system: (a) 9M layers unit cell, (b) trimer structure.

The $9M$ $BaIrO_3$ phase is not the only phase that belongs to the stoichiometric composition of $BaIrO_3$. A number of other polytypes phases have been reported to be exist. The $9M$ $BaIrO_3$ is the only phase that can be synthesized under an ambient pressure and relatively low temperature. The other reported phases are high temperature and/or high pressure (up to 10 GPa) phases. For example, $5H$ $BaIrO_3$ phase has been reported as a ferromagnetic metal that orders at 50 K [77]. $6H$ $BaIrO_3$ phase is a paramagnetic metal with quantum critical point (QCP) [78]. $6M$ $BaIrO_3$ is also reported as a Pauli paramagnetic metal[79]. These different polytypes phases emphasize the importance and criticality of the ratio of stacking of the octahedra within the unit cell.

4.2.2 Magnetic and Transport Properties of BaIrO$_3$

$BaIrO_3$ is a weak ferromagnetic insulator that orders at 183 K. The anisotropy of the $BaIrO_3$ structure; quasi 1D along the c-axis and 2D in ab-plane, is clearly reflected in the magnetization data as illustrated in the upper panel of figure (4.4). The figure shows the magnetization measurement on single-crystal samples of $BaIrO_3$ within a temperature range of 1.7 K to 330 K. This measurement was a field cooling (FC) measurement in a magnetic field of 0.01 T (100 Oe) which was parallel to the desired axis. The magnetization values of the left axis in the figure, are given in units of Bohr magneton per formula unit ($\mu_B/f.u$). The magnetization measurement reveals that the a-axis is the easy magnetic axis. The magnetization magnetic moments, at very low temperature of 1.7 K, differ by 15% between the two crystallographic directions with the a-axis is the higher value. Curie-Weiss fitting of the high temperature paramagnetic range, above 183 K, gives a small effective moment of about 0.13 ($\mu_B/f.u$); other similar iridate system also has shown this small value of an effective moment [17]. The calculated Curie-Weiss temperature is 175 K [16], which is comparable to the ordering temperature 183 K. The inset in figure (4.4) shows the hysteresis in the magnetization curve as a function of the applied magnetic field M(H), at the temperature 2 K. The field was swept from -14 T up to 14 T. The measurement shows that the measured saturated moment is about 0.039 ($\mu_B/f.u$) at $\mu_0 H \ = 14$ T, which is much lower than the expected value for $S = \frac{1}{2}$ of $Ir^{4+}(5d^5)$ system.

A reported muon spectroscopy study (μSR) by Brooks et al.[80] on samples of $BaIrO_3$ has confirmed that the small magnetic moment of Ir ion is mainly occurs because of $5d - 2p$ orbitals hybridization and a small exchange splitting in the 5d bands. With these conclusive results, the magnetic moment in $BaIrO_3$ originates from the polarization of Ir ion spins; these results correct the previous picture that attributes the weak ferromagnetism to a canted antiferromagnetic state. In another experimental work, Laguna-Marco et al. [81] have reported that the x-ray absorption spectroscopy (XAS) and x-ray magnetic circular dichroism ($XMCD$) studies have revealed a presence of a strong spin-orbit coupling in the ground state of the $BaIrO_3$. These studies have calculated the spin moment contribution and orbital moment contribution in the observed magnetic moment of the system, and have concluded that the contribution of orbital moment seems to exceed that of spin moment.

The lower panel of figure (4.4) illustrates the measured electrical resistivity within a temperature range from 1.8 K, the lowest temperature, to 325 K. The anisotropy in the resistivity measurement, below the transition temperature 183 K, reflects the quasi one-dimensional nature of the $BaIrO_3$ structure. It is clear from figure (4.4) that the c-axis conductivity is notably higher than that of the a-axis. The insulating behavior in both directions continues to persist in lower temperatures down to 1.8 K. The room temperature resistivity of the c-axis is 28 $m\Omega\ cm$ and it is 56.5 $m\Omega\ cm$ for the a-axis. Comparing the anisotropy in the resistivity along the crystallographic axes with another iridium compounds, like Sr_2IrO_4, shows that this anisotropy is not that large [17]. The transition in resistivity at $T_C = 183$ K, which is the same magnetic ordering temperature, is abrupt and the steady increase indicates a progressive localization of charge carriers. The inset of the lower panel of figure (4.4) shows the

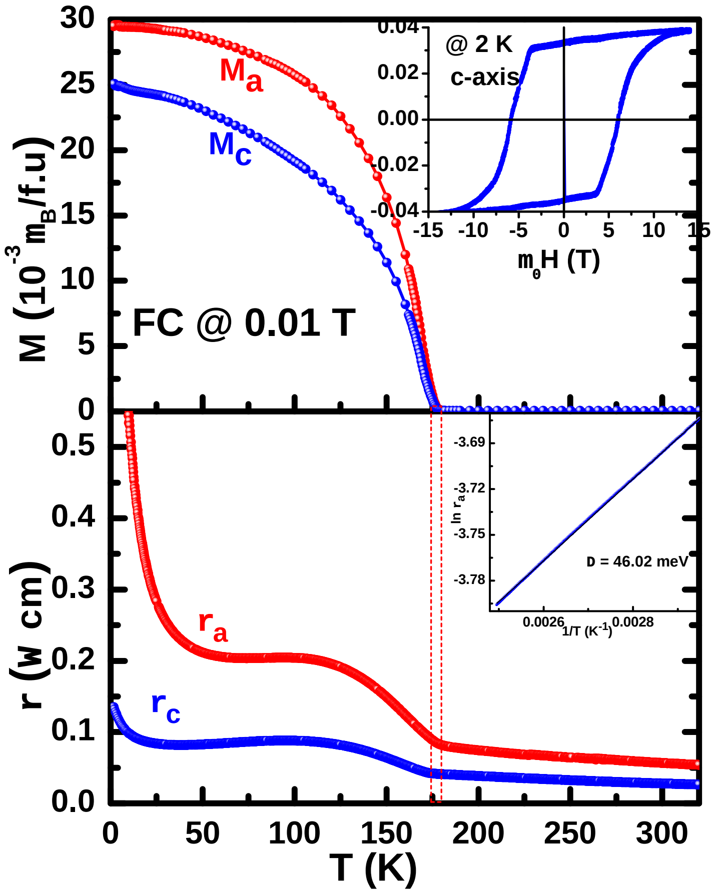

Figure 4.4: The magnetic and transport measurements of $BaIrO_3$. Upper panel shows the FC magnetization of the two crystallographic axes, and the inset shows the isothermal magnetization at 2 K. Lower panel shoes the electrical resistivity along the two axes as a function of temperature, and the inset is the activation law fitting and the gap energy ($46.02\ meV$).

result of an activation law fitting of the c-axis resistivity, for temperature range 300 – 400 K, this fitting gives an energy gap of 46 meV. This value of the insulating gap is small; any perturbation to the electronic configuration probably be able to eliminate this gap and tip the system to a metallic or a metallic-like state.

The observation of a charge-density wave (CDW) in $BaIrO_3$ below the ordering temperature, T_C = 183 K, raised an important question about the origin of such observation [16], especially the temperature dependence of a resistivity measurement shows a nonmetallic state for this system. Normally, CDW is associated with a metallic state in conventional systems. The formation of weak ferromagnetism at T_C= 183 K, nonmetallic state, and the observation of the CDW make this system of intensive interest for 5d TMOs research groups. Cao et al. introduced a new proposal based on the formation of band magnetism because of a small exchange splitting that creates CDW below T_C. This splitting is propped by a subtle lattice distortion and causes a gap at the Fermi surface. The later tight-binding band calculations provide a support for this proposal by showing a sharp peak for the density of state at the Fermi level. This sharp peak in the density of states sets the system on the verge of metallic state.

4.3 BaRuO$_3$ System

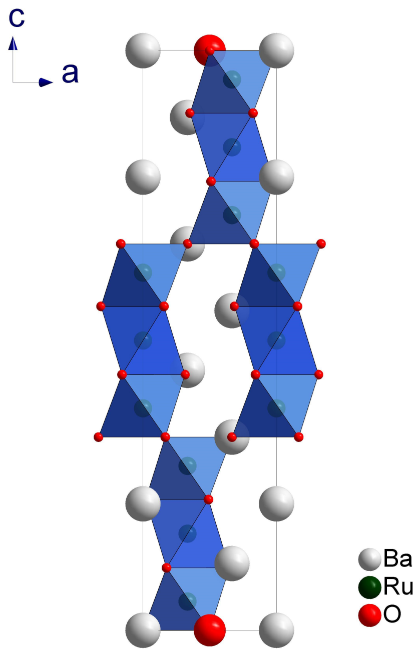

Figure 4.5: The crystal structure of the hexagonal perovskite $BaRuO_3$

4.3.1 Crystal Structure

The $BaRuO_3$ crystal structure, at room temperature, is similar to that of $BaIrO_3$, except for the buckling and twisting of trimers due to the monoclinic distortion. $BaRuO_3$ is a 9R hexagonal perovskite. The unit cell has the space group $R\bar{3}m$ symmetry. The Ru_3O_{12} trimers of $BaRuO_3$, formed by three face-sharing RuO_6 octahedra along c-axis, and are identical to those of $BaIrO_3$, as shown in figure (4.5). The trimers of $BaRuO_3$ are vertex-linked as one-dimensional chains along the c-axis. The lattice symmetry can be described by either a hexagonal unit cell or a rhombohedral unit cell. Sometimes ambiguities may arise because of choosing different unit cells to describe the same crystal structure. The lattice vectors are different in different unit cells, and the direction symbols and plane indices will also be different. So, in describing some crystal structure, the unit cell that used to describe the lattice should be specified, and the transformation relations that change the lattice symbols and plane indices to another unit cell can be stated. The trigonal symmetry system includes crystals with hexagonal lattice or rhombohedral lattice. The rhombohedral unit cell usually is not convenient to describe trigonal systems; instead, a larger (non-primitive) hexagonal unit cell is used. The transformation of the trigonal lattice with rhombohedral primitive unit cell ($a = b = c$ and $\alpha = \beta = \gamma$) to a hexagonal unit cell with ($\acute{a} = \acute{b} \neq \acute{c}$ and $\alpha = \beta = 90°$, and $\gamma = 120°$) is easily obtained using the transformation relations:

$$\acute{a} = a - b \tag{4.1}$$

$$\acute{b} = b - c \tag{4.2}$$

$$\acute{c} = a + b + c \tag{4.3}$$

And the transformation matrix has the form:

$$\begin{pmatrix} 1 & -1 & 0 \\ 0 & 1 & -1 \\ 1 & 1 & 1 \end{pmatrix}$$

Table 4.1: The crystal lattice information of both compounds, $BaIrO_3$ and $BaRuO_3$, M = Ir or Ru.

Compound	$BaIrO_3$	$BaRuO_3$
a(Å)	9.9935(2)	5.7366(1)
b(Å)	5.7352(1)	5.7366(1)
c(Å)	15.2376(3)	21.5933(6)
V (Å^3)	849.52(3)	615.40(3)
β (deg.)	103.4111(1)	-
M1-O (Å)	2.0016(61)	1.9730(12)
M3-O (Å)	2.0153(62)	1.9730(12)
M-O-M (deg.)	161.56(33)	180.0

As a comparison between the two structures, Table (4.1) summaries the crystal structure information of the two compounds.

4.3.2 Magnetic and Transport Properties of BaRuO$_3$

The magnetic properties of the isostructural compound $BaRuO_3$ are completely different from those of $BaIrO_3$. As shown in the upper panel of figure (4.6) , the magnetization measurement does not show any indication of magnetic ordering. The measurement was run from 300 K down to 1.7 K, and no magnetic ordering was observed. The small magnetization values and the paramagnetic behavior observed are

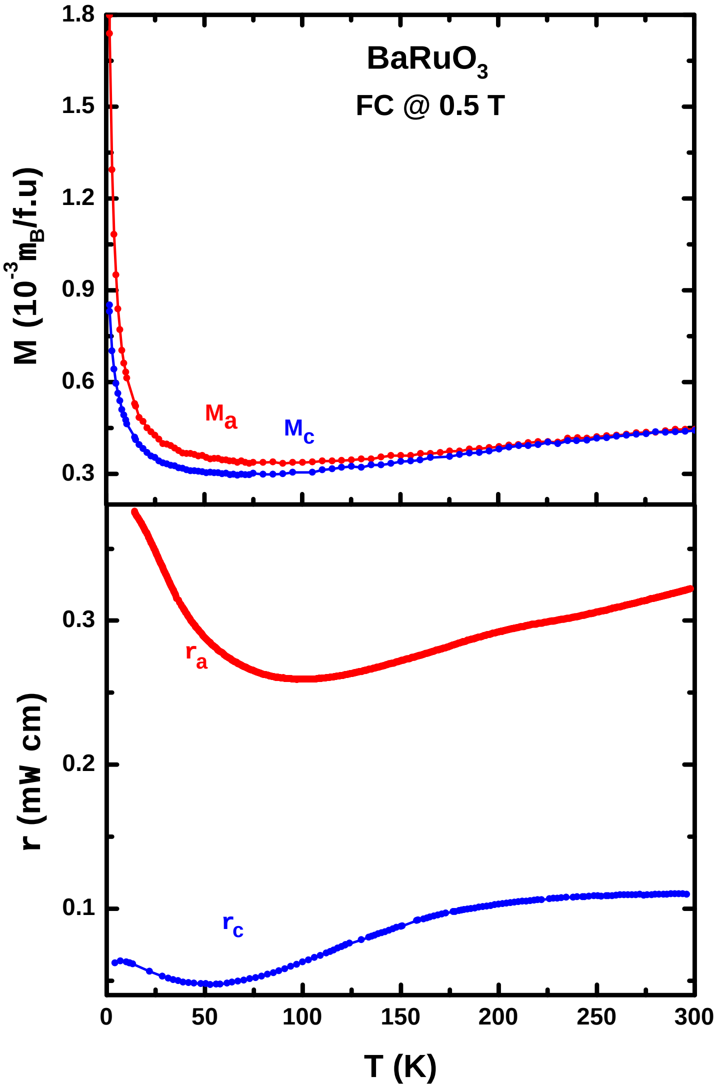

Figure 4.6: The magnetic and transport measurements of $BaRuO_3$. Upper panel shows the FC magnetization of the two crystallographic axes. Lower panel shoes the electrical resistivity along the two axes as a function of temperature, and the activation law fitting gives a gap energy of 2.0 meV (not shown).

indications of the full loss of the local moment of the Ru ion [82]. It is obvious that the magnetization is weakly temperature dependent for the both crystallographic directions. The magnetization anisotropy between the two crystallographic directions is modest, see the upper panel of figure (4.6). Along the a-axis, it decreases smoothly from 300 K down to around 100 K before it starts to increase. Along the c-axis, the decrease in magnetization continues down to 50 K before it rises. The decrease in magnetization as temperature decreases is an unusual behavior for a material based on magnetic ions. Also, this decreasing behavior of magnetization does not follow the Curie-Weiss law. The magnetization value at its minimum is about two-third of the room temperature magnetization. The average value of the magnetic susceptibility within this range is about $4 \times 10^{-4} emu/mole$. This value of susceptibility is due to the Pauli paramagnetism of the conduction electrons [82]. The free electron model corresponds this value of susceptibility to high density of states at the Fermi Level. If this the case, it should be reflected in the factor γ of the electronic contribution in heat capacity to be $\sim 30 mJ/molK^2$. In this work, the measured γ factor was $\sim 8 mJ/molK^2$, which indicates that the paramagnetic susceptibility of $BaRuO_3$ has enhanced by 3-4 times [82]. Below 100 K, the increase of a-axis magnetization is faster than that of the c-axis below 50 K. This divergence between the a- and c-axis, below the respected temperatures, is also reflected in the resistivity measurement, see the lower panel of figure (4.6). Within the whole range of temperatures, the magnetic anisotropy of the $BaRuO_3$ crystal directions is less profound than that observed in $BaIrO_3$.

The electrical resistivity measurement is shown in the lower panel of figure (4.6) for the temperature range from 1.8 K, as the lowest temperature, up to 300 K. The anisotropy in this measurement is clear for the indicated axes; the a-axis resistivity behavior of $BaRuO_3$ shows a metallic behavior with the temperature decreasing down to 100 K. This is the same temperature where the upturn in the magnetization was occurred, see the upper panel in figure (4.6). Then, a crossover to a different behavior was shown as temperature goes below the 100 K. This crossover shows an increase in the resistivity with the temperature decreasing, which is an indication of the emergence of an insulating state.

The c-axis resistivity shows a clear difference from that of the a-axis; it maintains a metallic behavior all the way down to 50 K; consistent with the magnetization measurement. Below this temperature, the resistivity seems to take an upturn. Low temperature resistivity measurements on the same phase for other single-crystal and polycrystalline samples confirmed this upturn in both directions [82].

Figure (4.7) shows a comparison picture of the distinct magnetic and transport properties of the two compounds. Note the different scales between the right and left axes for magnetization. Also, the resistivity measurements are extended over a wider range of temperatures; from 12 K as the lowest temperature to 750 K.

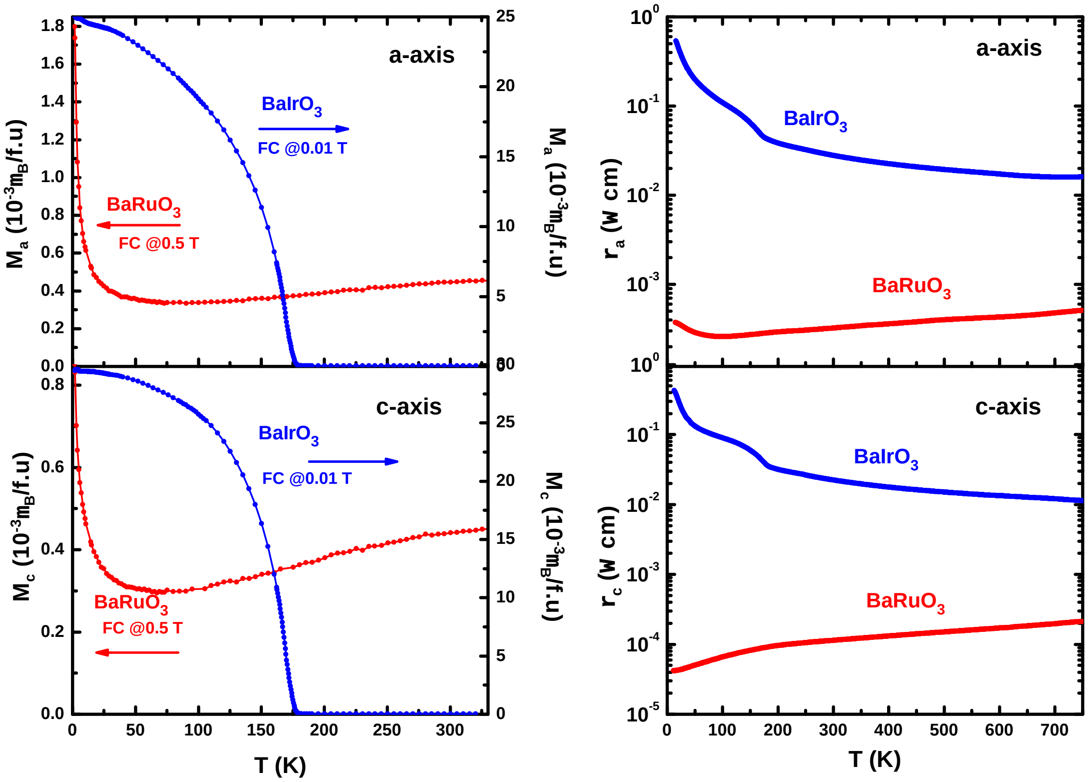

Figure 4.7: A comparison picture of the magnetic and transport properties of $BaIrO_3$ and $BaRuO_3$; the left panel is the magnetic properties of the a-axis (up), and the c-axis (down), the right panel is the high-temperature electrical resistivity measurements of the a-axis (up), and the c-axis (down).

4.4 $\mathbf{BaIr_{1\text{-}x}Ru_xO_3}$ System

The $BaIr_{1-x}Ru_xO_3$ system was made by a systematic chemical B-site substitution for the Ir^{4+} ion by Ru^{4+} ion, within a wide range of substitution, $0 \leqslant x \leqslant 1$. The lowest concentration of x = 0.015 exhibits very distinct magnetic, transport, and thermodynamic properties that can not be fitted with the trend was shown by the higher concentrations. Even though, the EDX result of this concentration confirms the accuracy of the doping level and the consistency of the 1:1 ratio of Ba:(Ir+Ru). The higher levels of doping, until x = 0.82, show a systematic change in the system behavior. The magnetic, transport, and thermodynamic properties of these higher concentration systems indicate a rich physics area worthy of investigation. A phase diagram for the different states that were observed through the course of the measurements under the systematic substitution of Ru can be constructed as a function of the ruthenium concentration x. This phase diagram summarizes the main findings of the study.

4.4.1 The Lowest Concentration x = 0.015 of the $BaIr_{1-x}Ru_xO_3$ System

The lowest concentration of x = 0.015 shows a distinct magnetic behavior that is different from the other concentrations as shown in panel (a) of figure (4.8). This behavior is intrinsic and repeatable feature and also was shown in the transport behavior. The magnetization measurement shows a magnetic ordering at T = 110 K, with similar behaviors for both crystal directions. The Curie-Weiss law fitting gave the value of -40.6 K for the Curie-Weiss temperature θ_{CW} and an effective magnetic moment of $\mu_{eff} = 0.45\mu_B/f.u$, which are different from those reported for the parent compound $BaIrO_3$ ($\theta_{CW} = 175K,\ \mu_{eff} = 0.13\mu_B/f.u$). The isothermal magnetization is also shown in figure (4.8). The saturated moment μ_S is vastly reduced for this smallest concentration ($\mu_S = 0.01\mu_B/f.u$) as can be seen in the inset of panel (a) of figure (4.8).

The other behavior curves clearly show that the insulating gap has been vastly minimized by this low percentage of Ru substitution (x = 0.015), as shown in figure (4.8). As mentioned before, the electrical resistivity for this concentration is different from those were observed in the other low concentration measurements, as shown in figure (4.16). The x = 0.015 case shows a different anisotropy feature as the c-axis resistivity is higher than the a-axis resistivity and the ratio of $\frac{\rho_a}{\rho_c}$ at the room temperature is about 0.8, while all the other concentrations show an opposite anisotropy. Another observation in this lowest concentration is the steep decrease in the resistivity as the temperature decreases, before it takes the upturn. This upturn occurs at 55 K for the a-axis resistivity and at 30 K for the c-axis resistivity. The decrease in resistivity ($\frac{d\rho}{dT} > 0$) confirms the metallic behavior of the system with this concentration. An activation law fit:

$$\rho(T) \sim \exp(\frac{\Delta}{2k_BT}), \tag{4.4}$$

where Δ is the energy gap and k_B is Boltzmann's constant; gives a very small insulating gap in this concentration of about 0.23 meV.

The low temperature heat capacity C(T) measurement for the x = 0.015 is very similar to the parent compound and is different from the rest concentrations. The electronic contribution term gives γ to be increased from $\sim 1\ mJ/mol\ K^2$ for the $BaIrO_3$ to 8.75 $mJ/mol\ K^2$ for x = 0.015, the fitting of $\frac{C(T)}{T} \propto T^2$ is shown in the inset of figure (4.8) panel (d).

Also, the thermoelectric power measurement of the lowest concentration shows a distinct behavior that is different from the rest concentration. This system shows a minima valley feature within the wide range of temperatures 50-600 K. It means that the system has behaved as a metallic from the high temperature down to 250 K, then the system changes its behavior to an insulating behavior at very low temperatures. This minimum occurs at 250 K for both directions, S_a has its minimum of 35 $\mu V/K$, while the c-axis has the value of 28 $\mu V/K$ as its minimum. It is possible that at this range, there is a kind of rebalancing between the two types of charge carriers; that is the electrons and the holes. Another observation in this system is the anisotropy, it

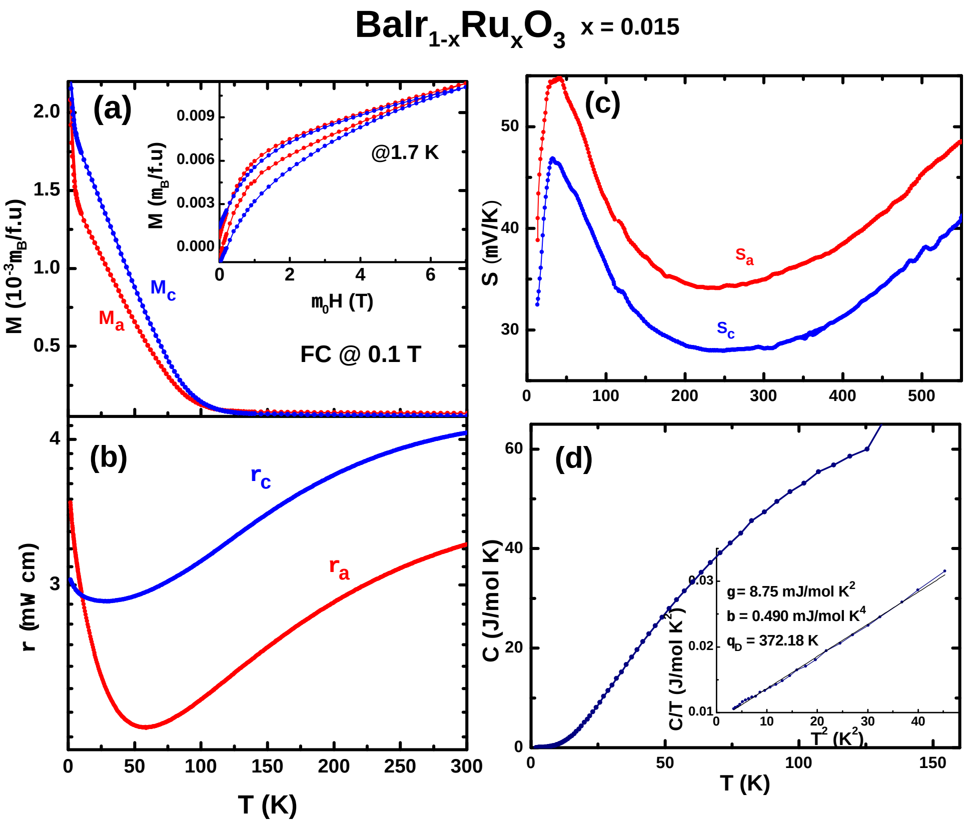

Figure 4.8: The distinct behavior of the lowest concentration of x = 0.015 along its two crystallographic axes; the a-axis (red curve) and the c-axis (blue carve): (a) the field cooling (FC) magnetization measurements at 0.1 T ,and the inset shoes the isothermal magnetization of this system at 1.7 K; (b) the resistivity measurement along the two crystallographic axes; (c) the Seebeck coefficient measurement; and (d) shows the low temperature heat capacity measurement of this concentration and the inset illustrates the isothermal magnetization measurements at T = 1.7 K

is opposite to the anisotropy in the higher concentrations, here $S_a > S_c$. In addition, there is a sharp peak at very low temperatures and which is centered at 40 K. The peak's values are 55 $\mu V/K$ and 47 $\mu V/K$ for S_a and S_c, respectively.

4.4.2 Crystal Structure of $BaIr_{1-x}Ru_xO_3$

As mentioned before, the parent compound of this system is the hexagonal perovskite $BaIrO_3$. The crystal structure experiences a monoclinic distortion, and the unit cell has characterized with the space group $C2/m$ [76]. The important structural features of $BaIrO_3$ are the twisting and buckling of the trimers because of this monoclinic distortion. This buckling causes tilting to the trimers with an angle of about 13° between the trimers' long axes . The lattice parameters and other crystal structure information of the parent compound are listed in table (4.1). For the $BaIr_{1-x}Ru_xO_3$

system, single-crystal x-ray diffraction measurements were performed on high quality single-crystal samples. The SEM images in figure (4.9) show a few examples of single-crystal samples with a uniform shape and a large size. Two different concentrations of the system $BaIr_{1-x}Ru_xO_3$ were used as representative members for this system: a low concentration sample of $x = 0.10$ and a high concentration one of $x = 0.63$. The two concentrations were found to have a similar crystal structure to the parent compound, which means the crystal structure was preserved for the doped system up to high levels of doping. For the low level of doping, x = 0.10, the extracted information indicates that the substitution of the Ru^{4+} ion (ionic radius = 0.620 Å) for the Ir^{4+} ion (ionic radius = 0.625 Å) generates changes to the lattice parameters and the structure characterizations. These changes have affected the related transport and thermodynamic performance of the system. The observed changes in the crystal structure under this low level of substitution include:

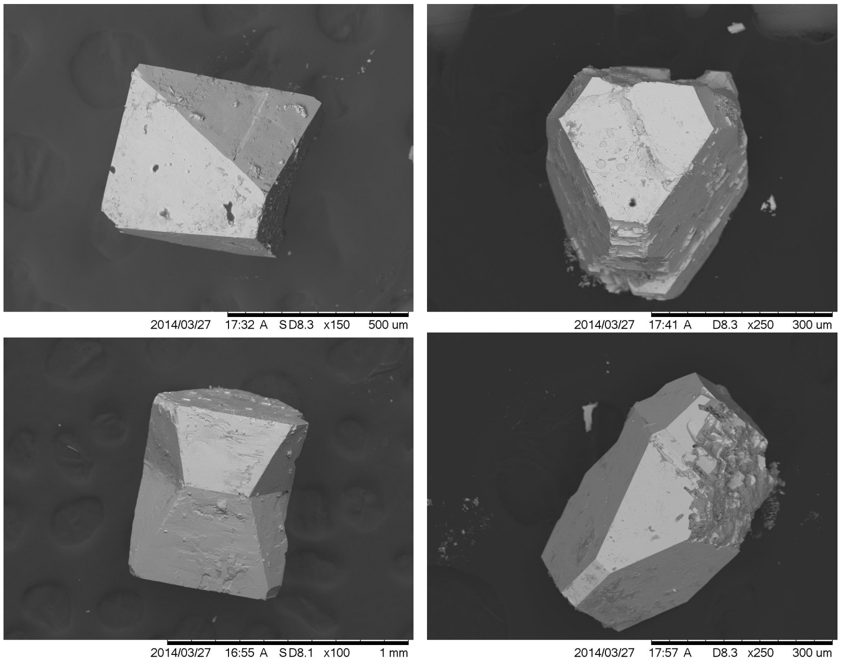

Figure 4.9: SEM images of samples of the system $BaIr_{1-x}Ru_xO_3$ with different concentrations

- The lattice parameters a, b, and c have changed under this low substitution. The a-axis was shrunk by 0.1% from 9.9935 Å to 9.9839 Å. The c-axis was also shrunk by a higher percentage of 0.83% from 15.2376 Å to 15.1107 Å. In contrast, the b-axis was expanded by a very small percentage of 0.044% from 5.7352 Å to 5.7377 Å. The angle β was reduced from 103.4111° to 103.3402°.

- The unit cell volume of this concentration is very close to that of the parent compound, the decrease in the volume was less than 1%. This change in the unit cell volume, as well as the lattice parameters, is expected because of the smaller size of the Ru^{4+} ion.

- The change has also affected the bonds length and angles. For example, the bond Ir1-O1 was contracted by less than 0.1 from 2.0315 Å to 2.0297 Å. The related bond angle, Ir1-O1-Ir3 was increased by 0.84% from 156.269° to 157.579°.

For the higher concentration, x = 0.63, the changes in the crystal structure were bigger and more profound. These changes include the following observations:

- The lattice parameters a, b, and c, were also changed for this system. The a-axis was shrunk by 0.5% from 9.9935 Å to 9.9440 Å, and the c-axis was decreased by a higher percentage of 2.8% from 15.2376 Å to 14.8102 Å. The b-axis was expanded by a smaller percentage compared to the change in a- and c-axis. It changed from 5.7352 Å to 5.7429 Å and the percentage change is 0.13%. The angle β also was reduced for this high concentration from 103.4111° to 102.8574°.
- The unit cell volume for this concentration was reduced by about 3%. This reduction in the unit cell volume is bigger than the lower concentration. The change in the unit cell volume and the lattice parameters did not affect the crystal structure symmetry; the doped system still has the space group $C2/m$ symmetry.
- The change in the crystal structure because of doping, also affected the bonds length and angles. The Ir3-O2 bond was contracted by a factor of 2.1%, from 2.0153 Å to 1.9731 Å. The change in the bonds length and angles is faster within the high concentration regime. The related bond angle Ir3-O2-Ir1 was increased by 7.9% from 161.560° to 174.296°. The change in the bonds length and angles has a direct effect on the shape of octahedra and their deformation.

Table 4.2: The crystal lattice information of two different concentrations, $x = 0.10$ and $x = 0.63$, along with the two ends compounds, $BaIrO_3$ and $BaRuO_3$

Compound	$BaIrO_3$	x = 0.10	x = 0.63	$BaRuO_3$
a(Å)	9.9935(2)	9.9839(2)	9.9440(2)	5.7366(1)
b(Å)	5.7352(1)	5.7377(1)	5.7429(1)	5.7366(1)
c(Å)	15.2376(3)	15.1107(4)	14.8102(4)	21.5933(6)
V (Å^3)	849.52(3)	842.25(3)	824.57(3)	615.40(3)
β (deg.)	103.4111(1)	103.3402(9)	102.8574(9)	-
M1-O (Å)	2.0016(61)	1.9918(21)	1.9897(32)	1.9730(12)
M3-O (Å)	2.0153(62)	2.0132(24)	1.9731(22)	1.9730(12)
M-O-M (deg.)	161.56(33)	163.678(41)	174.296(25)	180.0

The overall picture of the crystal structure changes, within the two investigated ranges, is shown in figure (4.10). This picture presents the systematic change in:

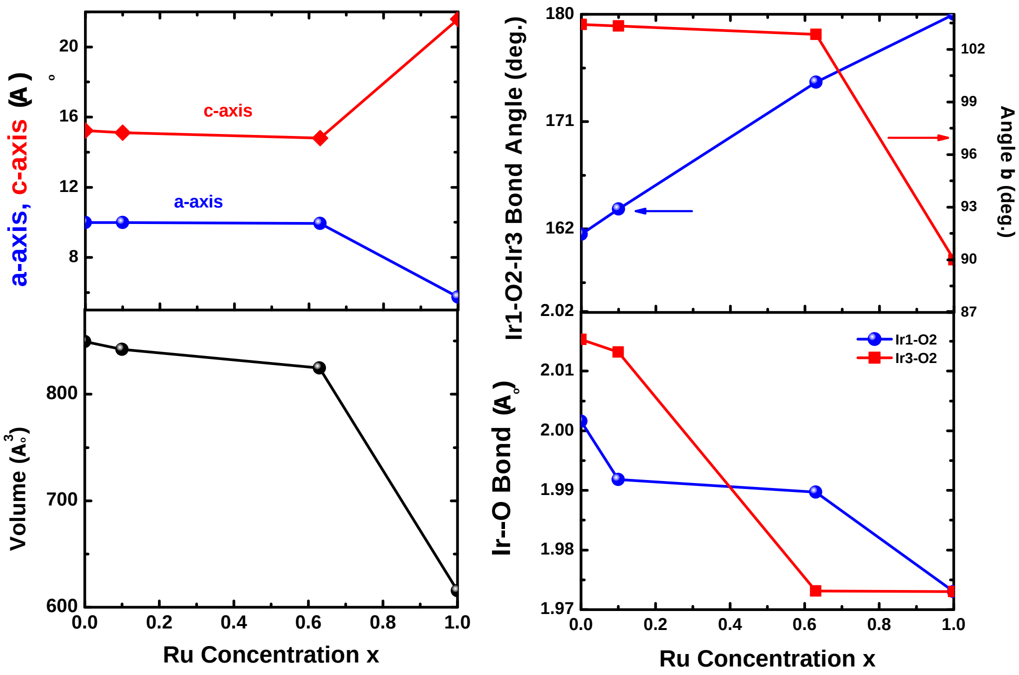

Figure 4.10: Crystal structure changes of the system $BaIr_{1-x}Ru_xO_3$ as a function the concentration; upper left panel is the lattice parameters change; lower left panel is the change of the unit cell volume; right upper panel is the change in the Ir-O-Ir bond angle and the angle β; right lower panel is the change in the bonds' length.

the lattice parameters a, c, and the angle β, and the unit cell volume (V). Also, it shows the change in the length of the bonds $Ir1 - O2$ and $Ir3 - O2$ and the bond angle $Ir - O2 - Ir3$. Table (4.2) lists the crystal structure comparison between the two concentrations, and also shows the crystal information of the two end compounds, $BaIrO_3$ and $BaRuO_3$.

The other important observation under the effect of Ru doping was the huge decrease in the angle confined between the trimer's axes along the c-axis. This angle was 13.153° in the case of the parent compound $BaIrO_3$, and was reduced to 5.414° in the case of x = 0.63. These changes in the bonds length and angles, as well as the trimer's angle, are the main factors that impact the magnetic, thermodynamic, and transport properties of the $BaIr_{1-x}Ru_xO_3$ system.

For the chemical composition analysis of the samples, we run the energy dispersive x-ray (EDX) spectroscopy measurement. The obtained results confirmed the accuracy and uniformity of the 1:1 ratio of Ba to Ir, or Ba to Ir+Ru(Rh). These results also determined the Ru or Rh doping levels in these samples.

4.4.3 Magnetic Properties of $BaIr_{1-x}Ru_xO_3$

The direct effect of the Ru doping on the physical properties of the parent compound $BaIrO_3$ is obviously systematic, as can be seen from the magnetic susceptibility

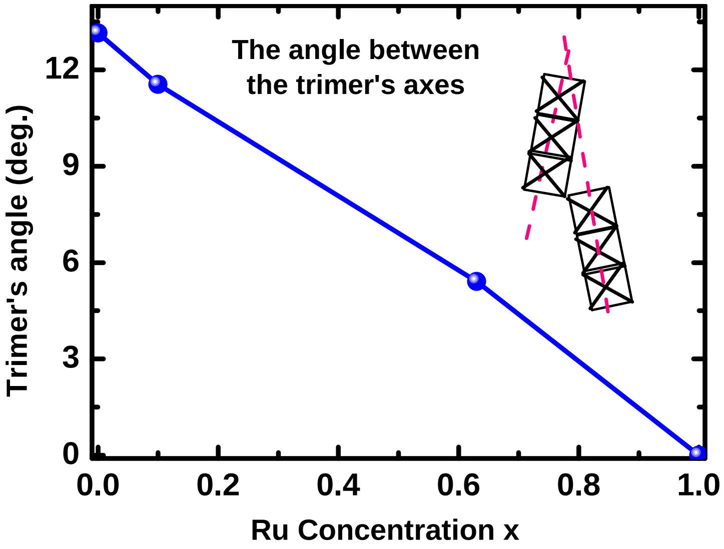

Figure 4.11: The change in the angle between the trimer's axes under the effect of Ru doping

measurement results. In the $BaIr_{1-x}Ru_xO_3$ system, increasing the Ru doping has systematically suppressed the high temperature magnetic ordering. The transition temperature T_c was lowered from 183 K for the parent compound $BaIrO_3$ $(x = 0)$ down to zero for the high concentration $x = 0.41$ and beyond as shown in figures (4.12). The magnetic susceptibility measurement $\chi(T)$ was run within a temperature range of 1.7 K to 300 K. The isothermal magnetization M(H) was measured at two different temperatures, the lowest temperature T = 1.7 K and at T = 80 K, which is below the ordering temperature for all the law concentrations; the field was swept from 0 T up to 7 T and then back to 0 T. The main features and observations as a result of increasing the concentration x include the following points:

- The magnetic anisotropy of the crystallographic axes was reduced because of the Ru doping, as shown in the magnetization curves of the parent compound x = 0.0 and the doped system of x = 0.10 in figure (4.13). The reduction of the anisotropy is a direct result of the weakened SOI; in addition to the suppression of the magnetic ordering. So, the increasing of the Ru doping concentration results in decreased anisotropy.

- From the isothermal magnetization measurement, the saturated moment μ_S is very small, and it increases as x increases, which is shown in figure (4.14), but it is still below the saturated moment of the parent compound $BaIrO_3$ ($\mu_S = 0.039\ \mu_B/f.u$), even with a concentration of x = 0.15 ($\mu_S = 0.029\ \mu_B/f.u$).

- As the ratio c/a decreases, as can be seen in table (4.2) , the relative strength of the SOI and tetragonal CFE also changes because the tetragonal CFE is enhanced and encourages a spin alignment along the c-axis [72].

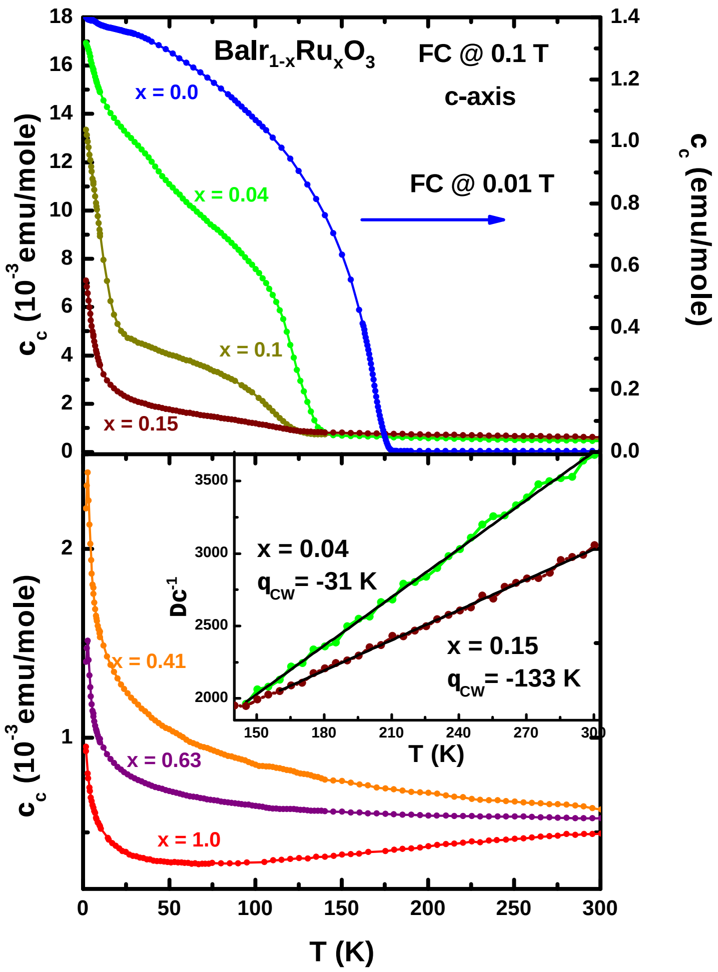

Figure 4.12: The magnetic susceptibility measurements of the $BaIr_{1-x}Ru_xO_3$ system; upper panel for x $\leqslant$ 0.15, lower panel for x $\geqslant$ 0.41. The inset in the lower panel shows the Curie-Weiss fitting for x = 0.04 and x = 0.15, and Curie-Weiss temperatures θ_{CW} are indicated

The magnetic susceptibility data, over the temperature range of 160-300 K, was fitted using the Curie-Weiss (CW) law:

$$\chi = \chi_0 + \frac{C}{\theta_{CW} + T} \tag{4.5}$$

Here, χ_0 is the temperature-independent susceptibility, θ_{CW} is the Curie-Weiss temperature and C is the Curie-Weiss constant. The non-linear fitting of CW law yields the χ_0 which was used to do the linear fitting of the modified CW law:

$$(\Delta\chi)^{-1} = \frac{\theta_{CW} + T}{C} \tag{4.6}$$

This relation was plotted for the temperature T versus $(\Delta\chi)^{-1}$, and the values of

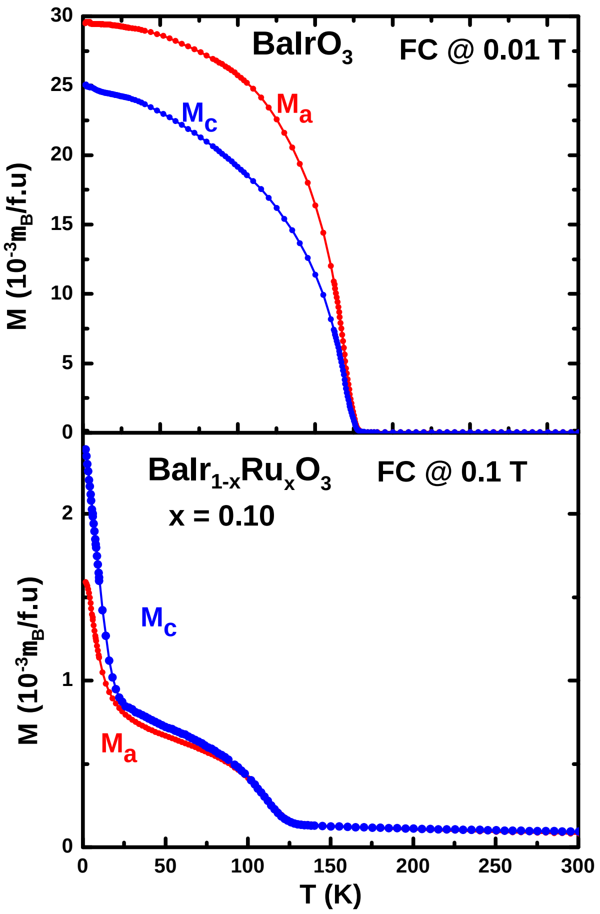

Figure 4.13: The magnetization measurements of the a-axis (red curve) and c-axis (blue carve) for the parent compound $BaIrO_3$ (upper panel), and for x = 0.10 (lower panel). This shows how the anisotropy reduced under the Ru doping.

θ_{CW} and C were extracted from the linear fitting. Here, θ_{CW} is the intercept of the line with the temperature axis, and C is the slope of this straight line. This linear fitting is shown in the inset of the lower panel of figure (4.12) for the concentrations x = 0.04 and 0.15. The change of Curie-Weiss temperature θ_{CW} is significant within the measured range of the concentrations; this reflects the rapid decrease of T_c, which becomes zero at x = 0.41. The Ru doping changes the θ_{CW} sign from positive for the parent compound (θ_{CW} = 175 K for x = 0.0) to negative values through the whole range of doping (x = 0.015, 0.04, 0.10, 0.15, 0.41 and 0.63). The sign change of θ_{CW} from positive to negative is an indicator of a change in the exchange coupling from ferromagnetic (FM), which is the pure compound state, to antiferromagnetic (AFM) for the doped system.

The increase in the absolute value of θ_{CW} is an indication of the increase in the antiferromagnetic coupling. $\mid \theta_{CW} \mid$ increases from $\sim$ 31 K (for x = 0.04) to $\sim$ 166 K, which is the largest, for x = 0.63. For x = 0.15, the Curie-Weiss temperature

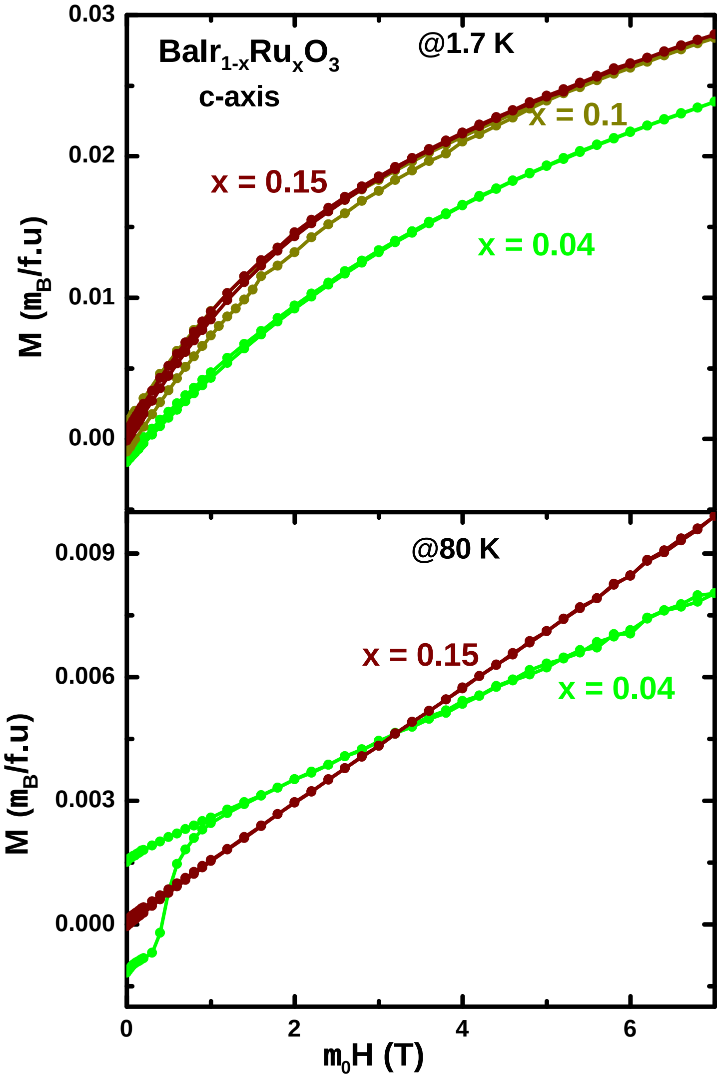

Figure 4.14: The isothermal magnetization measurements for x = 0.04, 0.10, and 0.15 of Ru concentrations of the $BaIr_{1-x}Ru_xO_3$ system; the upper panel at the lowest temperature T = 1.7 K, and the lower panel at T = 80 K.

was θ_{CW} = -133 K. The large absolute value of θ_{CW} = 133 K is a reflection of the increase in the antiferromagnetic coupling as x increases. The factor $f = (\frac{\theta_{CW}}{T_c} = \frac{133}{128} \sim 1)$ for x = 0.15 eliminates the existence of spins frustration in this system for x < 0.15. The higher concentration don't show any sign of a magnetic ordering down to 1.7 K. It is possible that both the disappearance of magnetic order at x = 0.41 and the increase in the strength of antiferromagnetic coupling as x increases; as reflected by θ_{CW}, are a consequence of atomic disorder among the Ru and Ir sites, and also the realization of spin frustrations in the system. For x = 0.63 the

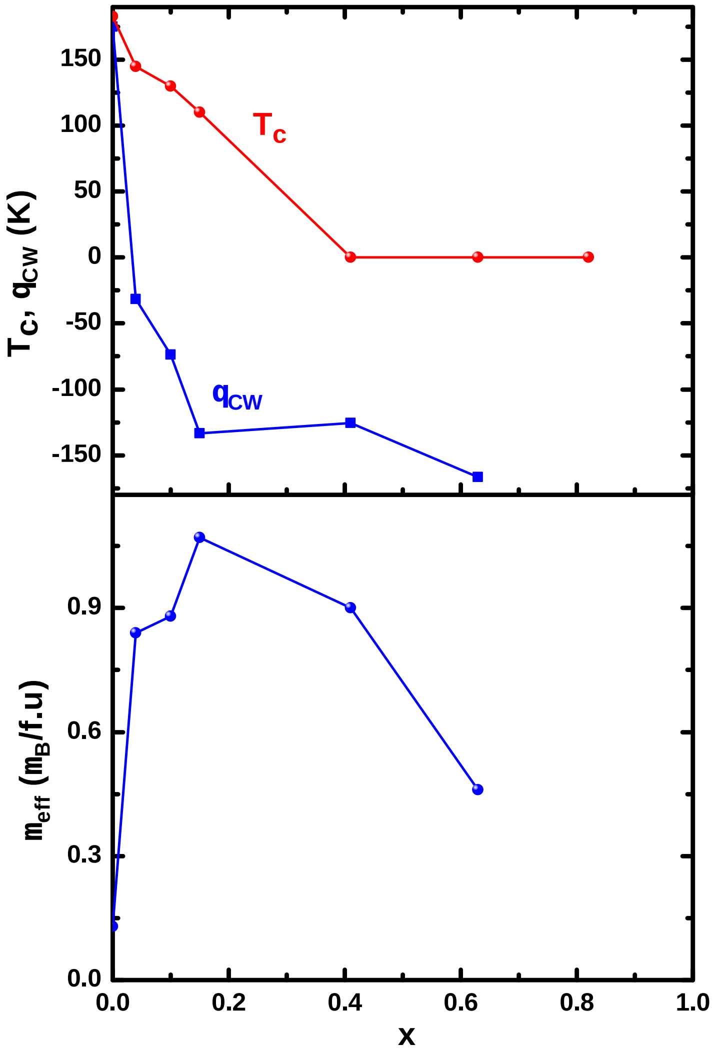

Figure 4.15: The change in the transition temperature T_C, Curie-Weiss temperature θ_{CW} (upper panel), and the effective magnetic moment μ_{eff} (lower pnel) of the $BaIr_{1-x}Ru_xO_3$ system

frustration measure factor $\dfrac{\theta_{CW}}{T_c}$ gives a value of ~ 118, which is high and supports the existence of a frustration state in the system. In addition, the influence of increasing the Ru concentration on the competing energies , such as the SOI, the non-cubic CFE, and the Hund's rule coupling, has also enhanced the competition between antiferromagnetic and ferromagnetic couplings.

The summary of the changes, that were observed in the magnetic properties of the $BaIr_{1-x}Ru_xO_3$ system, in terms of the transition temperature T$_C$, CW temperature θ_{CW}, and the effective magnetic moment μ_{eff}, under the Ru doping are pictured in figure (4.15).

4.4.4 Transport Properties of $BaIr_{1-x}Ru_xO_3$

As explained earlier, the low temperature insulating state in $BaIrO_3$ is a result of Mott localization in the frame of strong SOI regime. This gap opening is associated with the formation of charge density wave in this material [16] [83]. Ru doping effect is found to profoundly change the transport properties of the system; the change in the transport properties had been seen in other iridium systems under different doping situations [75][74]. The systematic substitution of the Ir ion by Ru changes the ground state of this system gradually from weakly-localized metallic state, for the very low levels of concentration, to paramagnet metallic state at higher levels of concentration, as can be seen in figure 4.16. The electrical resistivity measurements are performed for two different ranges of temperatures using two experimental settings. One is low temperature range from room temperature down to 1.8 K; for these measurements the transport properties option of the QD PPMS system was used. The other range is high temperature range, where the range extends from 12 K up to 750 K. In this setting, we utilize the high temperature interface option of the Displex

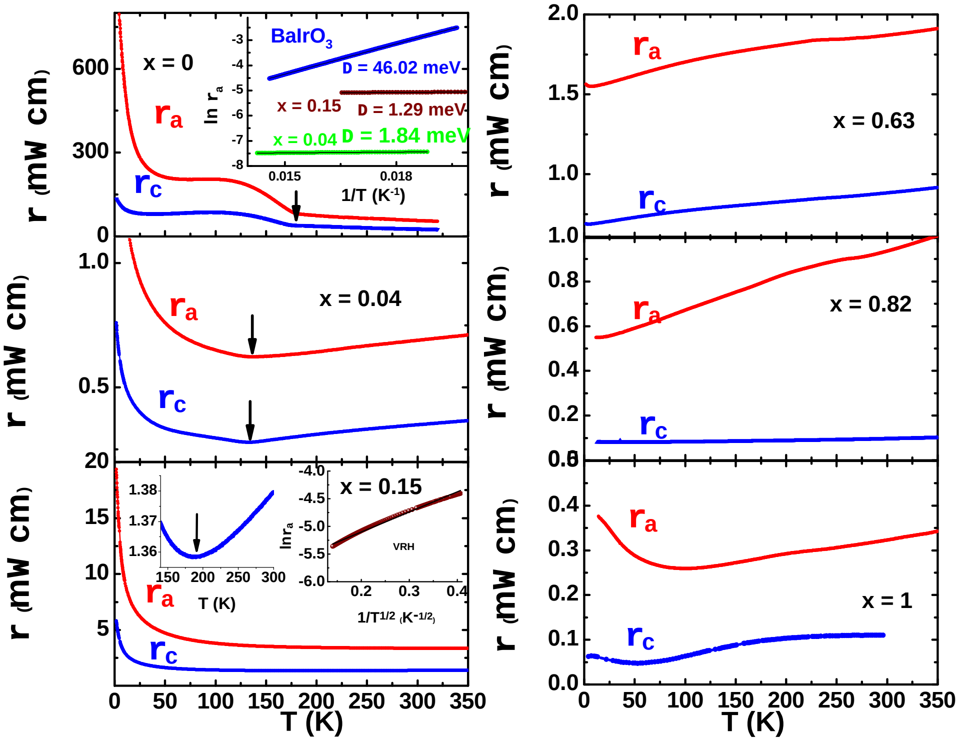

Figure 4.16: The electrical resistivity measurements of the $BaIr_{1-x}Ru_xO_3$ system; for x = 0, 0.04, 0.15. 0.63, 0.82, and 1.0. The inset in the upper right panel shows the activation energy law fitting with the gap energy values. The insets of the x = 0.15 panel; one (right) shows the variable range hoping (VRH) fitting for this concentration measurement, and the other (left) shows the metal-insulator transition temperature in this system. The vertical arrows indicate the metal-insulator transition temperature.

pneumatic closed cycle cryocooler (DE202), from Advanced Research Systems. The behavior curves at the low levels of concentration, $x \leq 0.15$, clearly show that the insulating gap has been greatly reduced, as shown in figure (4.16); similar to the case of the lowest concentration (x = 0.015). For these systems of low level of the Ru doping, the insulating gap was not fully closed as can be seen from the gap energy values obtained from the activation law fitting and is pictured in the inset of the upper right panel of figure (4.16). In addition, these low concentration systems exhibit a metal-insulator transition of remarkable behavior. Within the progressive increase of the Ru concentration at the low level of concentration ($x \leq 0.15$), the systems show a metallic behavior within a wide range of temperatures below the ambient temperature, then an upturn occurs at different low temperatures for different concentrations. In the case of x = 0.04, the resistivity continues to be lower in magnitude, lower than that of x=0.015, and the decrease in resistivity as temperature decreases is less steep than that of x =0.015, especially for the a-axis resistivity. As mentioned earlier, the anisotropy for this concentration and higher concentrations shows $\rho_a > \rho_c$; the ratio of $\frac{\rho_a}{\rho_c}$ at room temperature is about 2.0. The upturn for x = 0.04 concentration occurs at higher temperatures. The upturn in the a-axis resistivity starts at 135 K and it extends along wider valley. The c-axis upturn occurs at relatively a lower temperature, at 130 K, and it shows steeper upturn. The calculated insulating gap for this concentration is about 1.84 meV. Surprisingly, the next concentration, x = 0.15, shows noticeably a different behavior. First, the overall resistivity magnitude increases by more than 10 times; this increase was also observed in close concentration of x = 0.10, which shows an insulating state for both directions (not shown). Second, the a-axis resistivity shows a weak insulating behavior along a wide range of temperatures. Then, a sharp upturn that enhances the insulating state occurs at around 25 K. The other axis resistivity behavior, c-axis, barely shows a metallic characteristic as temperature goes down, and the upturn occurs at almost the same range as a-axis; the ratio of $\frac{\rho_a}{\rho_c}$ at room temperature is about 2.4. The activation law fitting deduces the insulating gap to be 1.29 meV, which is smaller than the previous one. The next measured concentration is x = 0.63; this concentration shows a persistent metallic behavior to the lowest temperature of 4 K, in which a very tiny upturn occurs. The anisotropy is consistent with the previous concentrations; the ratio of $\frac{\rho_a}{\rho_c}$ at the room temperature is about 2.1. In addition, the resistivity values are comparable to those measured in x = 0.04 samples. The highest concentration of doping was x = 0.82 and it shows a close analogy to the other end compound of the system, $BaRuO_3$. It shows a true paramagnet metallic state. The x = 0.82 system shows a continuous increase in resistivity as temperature increases. The resistivity behavior of the high concentration systems seems to be different from that observed in the low concentration systems. This difference is possibly attributed to the different mechanisms involved in the resistivity behavior. For the low concentrations the decrease in resistivity and, in turn, the emergence of a metallic behavior are connected to the minimization of the Mott insulating gap. At the same time, a small percentage of doping establishes a weak insulating state because of disorder. This disorder increases as the concen-

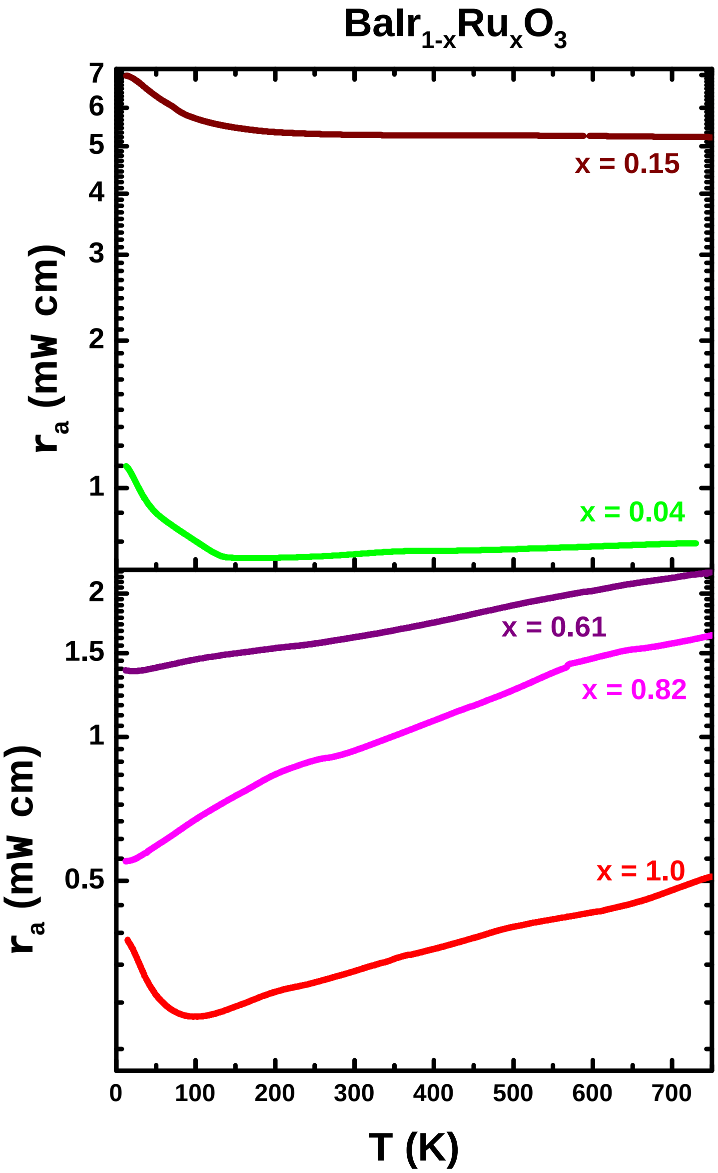

Figure 4.17: The high temperature electrical resistivity measurements of the $BaIr_{1-x}Ru_xO_3$ system, for x = 0.04, 0.15, 0.63, 0.82, and 1.0.

tration increases and becomes dominant at concentration levels between 10-15% of doping. The low temperature resistivity behavior within this range of doping follows the variable range hoping (VRH) fitting for $T^{\frac{1}{2}}$, as can be seen in the inset of the x= 0.15 resistivity curves in figure (4.16). At high level of concentration, and because the Ru doping is actually a hole doping, the increase in the charge carriers concentration, and in turn the density of states, overcomes the scattering due to the disorder state. In the other set of the high-temperature range of measurements, the lower range of the high-temperature range resistivity measurements (12 K up to 300 K) is very consistent with low temperature range measurements. In addition, interesting features are observed through the high temperature resistivity behavior. The high-temperature resistivity behavior for the lower level of doping is different from that was shown for the higher levels of doping. The high-temperature resistivity for the lower level of doping seems to be saturated at high temperatures, while the high level of doping shows a continuous increase in the resistivity as temperature goes higher to 750 K, these observations are illustrated in figure (4.17). The increase in resistivity as temperature increases is unusual behavior based on the conventional picture of the metallic behavior at high temperature regime. In a comparison with another iridates compound, Sr_2IrO_4, which is a single-layered perovskite structure. Under the effect of Ru substitution, the transport behavior of the system shows a well-established metallic state with x = 50% that persists to higher levels of doping. This metallic state is accompanied by a magnetic suppression at lower level of concentration, which is similar to what we have observed in the $BaIr_{1-x}Ru_xO_3$ system.

4.4.5 Heat Capacity Properties of $BaIr_{1-x}Ru_xO_3$

The specific heat or heat capacity measurement is a direct probe to study and investigate any bulk effects or transitions in the system, and it is a valuable source of information that can be extracted from its data analysis, such as the factor γ which is the electronic contribution of the heat capacity and Debby temperature θ_D. Figure (4.18) shows the heat capacity measurement of the $BaIr_{1-x}Ru_xO_3$ system; within the temperature range of 1.7 K to 70 K. The figure illustrates the temperature dependence of the heat capacity, C(T), and the data analysis for various Ru concentrations (x). The doped systems show obviously a different behavior from that was seen in the parent compound $BaIrO_3$, where the heat capacity measurement shows a step-like feature near the magnetic ordering temperature , $T_c = 183$ K. The change in the heat capacity (ΔC) near this temperature is about 2 J/mole K as measured by the relaxation method using QD PPMS[14]. The heat capacity at low temperatures shows different behaviors as a function of the doping level, see the inset of figure (4.18 a) .

There is an increase in the low temperature heat capacity values as the concentration increases within the low level of doping; from x = 0.04 to x = 0.15, as shown in the inset of panel a of figure (4.18). The low temperature measurements of the heat capacity can be analysed to assist the different contributions in the heat capacity values from the possible different mechanisms in the system. The relation of C(T), as a function of temperature, is defined as [84][85]:

$$C_{tot.}(T) = C_{ele.} + C_{phonon} + C_{magnon} \tag{4.7}$$

with the three different contributions; where $C_{ele.}$ represents the electronic contribution to the heat capacity (the Sommerfeld coefficient), C_{phonon} is the phonon contribution because of the lattice vibrations, and the C_{magnon} is magnon contribution, which is related to the existence of spin density wave (SDW). Each of the three contributions has different proportionality with temperature;

$$C_{ele} \propto \gamma T, \qquad C_{phonon} \propto \beta T^3, \ and \qquad C_{magnon} \propto \alpha T^{3/2} \tag{4.8}$$

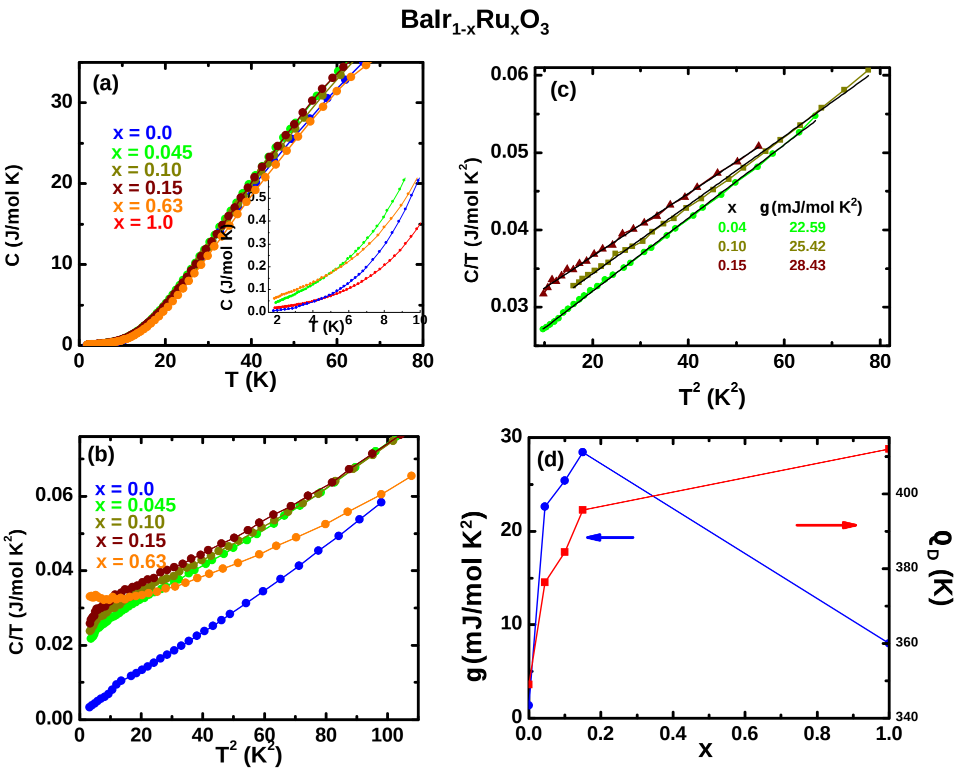

Figure 4.18: The heat capacity measurements C(T) of the $BaIr_{1-x}Ru_xO_3$ system and the post analysis; (a) the heat capacity measurements for x = 0.0, 0.04, 0.10, 0.15, 0.63, and 1.0. the inset shows the very low temperature measurements ($T < 10K$); (b) the C(T)/T behavior as a function of T^2 for the low temperature measurements ($T < 10K$); (c) The linear fitting of C(T) proportional to T^3 relation and the related γ obtained for x = 0.04, 0.10, and 0.15. (d) The phase diagram of γ and θ_D (Debby temperature) as a function of the concentration.

Assuming that the antiferromagnetic coupling is the dominant exchange interaction in these systems, the fitting of the low temperature heat capacity C(T) data, of the range 1.7 K < T < 10 K, should follow the form :

$$\frac{C(T)}{T} \sim \gamma + \beta T^2 \tag{4.9}$$

Plotting $\dfrac{C(T)}{T}$ as a function of T^2, and apply a linear fitting, which is pictured in the panel (c) of figure (4.18), then we can extract the needed information. The resulting straight line intercepts the y-axis at a value represents the coefficient (γ), which describes the electronic contribution in C(T). The other constant (β) which represents the slop, will provide an information about the phonon contribution and the lattice stiffness; these extracted informations are shown in figure (4.18) panel (d). The low range of concentrations of $x \leq 0.15$ show a noticeable change in the low temperature heat capacity by gradual increase in the heat capacity values as shown in the inset of panel (a) in figure (4.18).According to the fitting results, there is a substantial increase in the Sommerfeld coefficient γ within the low level of concentration. The increase in (γ) reaches $\sim 28mJ/molK^2$ for x = 0.15; compared to the small insulating value of $\sim 1mJ/molK^2$ for the parent compound (x =0.0). The concentrations have (γ) of $22.6mJ/molK^2$ and $25.4mJ/molK^2$ for x = 0.04 and 0.10 respectively. This increase in the electronic contribution term is an indication of an increase of the density of states at the Fermi level, $N(E_F)$. As x reaches 0.41 and higher, there is turn back in the heat capacity measurements to smaller values, with a different behavior from that of the low concentrations. This change in the heat capacity behavior approaches the low value of the other end of the range (x = 1.0); for the $BaRuO_3$ system. The overall picture of the Ru doping effects on the heat capacity measurements and the different fitting forms are pictured in figure (4.18).

4.4.6 Thermoelectric Power Properties of $BaIr_{1-x}Ru_xO_3$

The Seebeck coefficient S(T) , or the thermoelectric power (TEP), measurement was performed within a wide temperature range, from lowest temperature of 15 K to 600 K. Over this range, the parent compound has shown an insulating behavior. This insulating behavior is characterized by a slow increase in the Seebeck coefficient as temperature decreases. Near the transition temperature, 183 K, the slow increase is interrupted by a sharp upturn. The increase in the TEP value becomes precipitate as temperature continues to decrease; this is an indication that the charge carriers, which are holes in this case, are diminishing and an insulating gap opens. At 80 K the TEP reaches its maximum and then starts to decrease as temperature decreases. The difference in the maximum values of both crystallographic directions confirms the anisotropy in magnitude for both directions. The $S(T)$ of the c-axis has higher values than the a-axis. This is consistent with transport properties, where $\rho_c(T)$ shows higher resistivity values than $\rho_a(T)$ as illustrated in figure (4.16). The peak of $S_c(T)$ at 80 K reaches $240\mu V/K$ as shown in upper left panel of figure (4.19). The other axis $S_a(T)$ has its maximum peak of $220\mu V/K$ at almost the same temperature. Below the temperature of the maximum peak, the TEP behavior starts to decrease at a fast rate. The steep decrease below 80 K is an indication of the eruption in the density of states at this range. At the lowest temperature of 15 K, S(T) reads a value of about $150\mu V/K$.

With the Ru substitution, the emergence of a metallic state within the low range of doping, x $<$ 0.15, is confirmed by the huge reduction of S(T) magnitude. This drop in the S(T) magnitude was by tens fold of magnitude for the different low range of doping systems, as can be seen from the different panels of figure (4.19) . It is obvious that the S(T) behavior of $BaIr_{1-x}Ru_xO_3$ system is completely different from that of the parent compound (x = 0). For most of the doped system, the peak shape behavior is changed in these doped systems by a smoothly continuous drop in S(T). This drop continues all the way down to 15 K, where S(T) is just a few $\mu V/K$. The low Seebeck values are characteristics of metallic state. Within the doped systems of x $>$ 0.15, the anisotropy becomes less differential between the two directions. Both a- and c-axis TEP follow the same behavior with a small difference in magnitude

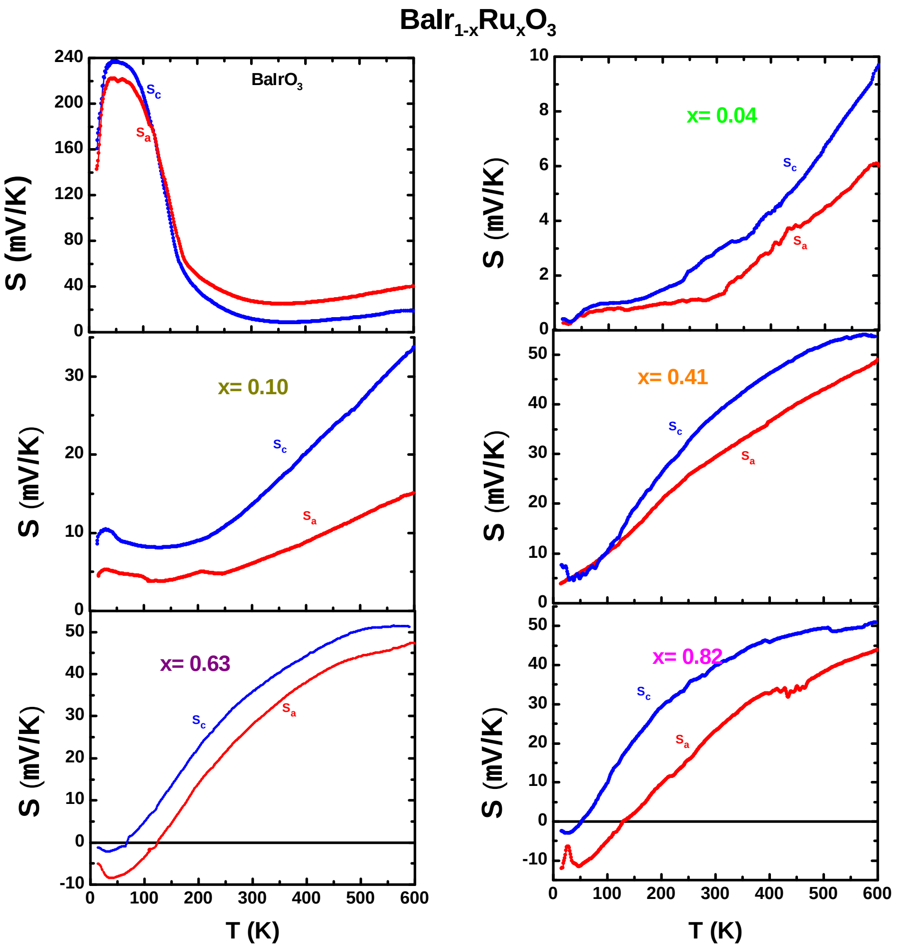

Figure 4.19: The thermoelectric power measurements S(T) of the $BaIr_{1-x}Ru_xO_3$ system; for x = 0.0, 0.04, 0.10, 0.41, 0.63, and 0.82.

of a few $\mu V/K$. These concentrations show $S_c(T)$ is always higher than $S_a(T)$. At lower temperatures, T < 200 K, samples with low concentration level of doping, x = 0.04 and x = 0.10, show weak dependence of S(T) with temperature, all the way down to 15 K. The anisotropy in magnitude becomes less as temperature decreases. At the very low temperature, there is a sign of small anomaly in some of the low concentration samples, for example x = 0.10. These anomalies are sample dependent. The higher concentrations, x = 0.63 and x = 0.82, keep the decreasing in S(T) as temperature decreases, and both become negative values when temperature goes below 130 K. The crossover between positive and negative values of S(T) is a signal for the competition between the charge carriers types, which are holes for the S(T) positive values and are electrons for the negative values.

As a comparison between all the concentrations, figure (4.19) shows the TEP behavior and its differences for the two ranges of concentrations. Within the low concentration range, the increase in the concentration from x = 0.0 to x = 0.04 causes a huge decrease in TEP. Then, TEP start to increase for the next concentrations, x = 0.10 and x = 0.15, which is identical to the resistivity measurements within this range of doping. The comparison also emphasizes that the high concentration samples are more close to the metallic behavior; this is consistent with other transport measurements.

4.5 Phase Diagram

The findings of this study about the evolution of the ground state in the system $BaIr_{1-x}Ru_xO_3$, under the systematic doping of Ru, can be summarized in the phase diagram (4.20). The rich T-x phase diagram of $BaIr_{1-x}Ru_xO_3$ features three major effects: (1) Light Ru doping ($0 \leq x \leq 0.15$), effectively reduces the SOI and prompts simultaneous and precipitous drop in both the electrical resistivity $\rho(T)$ and the magnetic ordering temperature T_C. These results indicate that the Ru concentration does provide a degree of control over the splitting between the $J_{eff} = \frac{1}{2}$ and $J_{eff} = \frac{3}{2}$ bands. At low temperature, T<50 K, a localized insulating state persists because of the partial elimination of the Mott insulating gap. (2) Near the concentration of x = 0.15 a remarkable disorder state established and the Anderson localization mechanism is dominant in this case. (2) Higher Rh doping ($0.15 \leq x \leq 0.82$), increases the doped charge carriers density and a true metallic state is realized accompanied by enhanced paramagnetic state . Figure (4.20) shows a phase diagram for $BaIr_{1-x}Ru_xO_3$, which was generated based on the alloying data presented above. The initial Ru doping effectively reduces the SOI, and in turn the splitting between the $J_{eff} = \frac{1}{2}$ and $J_{eff} = \frac{3}{2}$ bands. The doping also alters the relative strength of the SOI and the tetragonal CFE that dictates the magnetic state and affects the band gap near E_F. In addition, the Ru doping also enhances the Hund's rule coupling that competes with the SOI, and prevents the formation of the $J_{eff} = \frac{1}{2}$ state [86]. These SOI-induced changes account for the simultaneous precipitate decrease in $\rho(T)$, and T_C which vanishes at x = 0.41. As x increases further, the Ru hole doping overcomes any disorder and derives the system to be metallic. Each Ru atom adds one hole, giving a rise to a higher density of states near E_F and hence supporting a more robust metallic state in this system. In addition, the SOI may no longer be strong enough to support the $J_{eff} = \frac{1}{2}$ insulating state, and the Hund's rule coupling is enhanced.

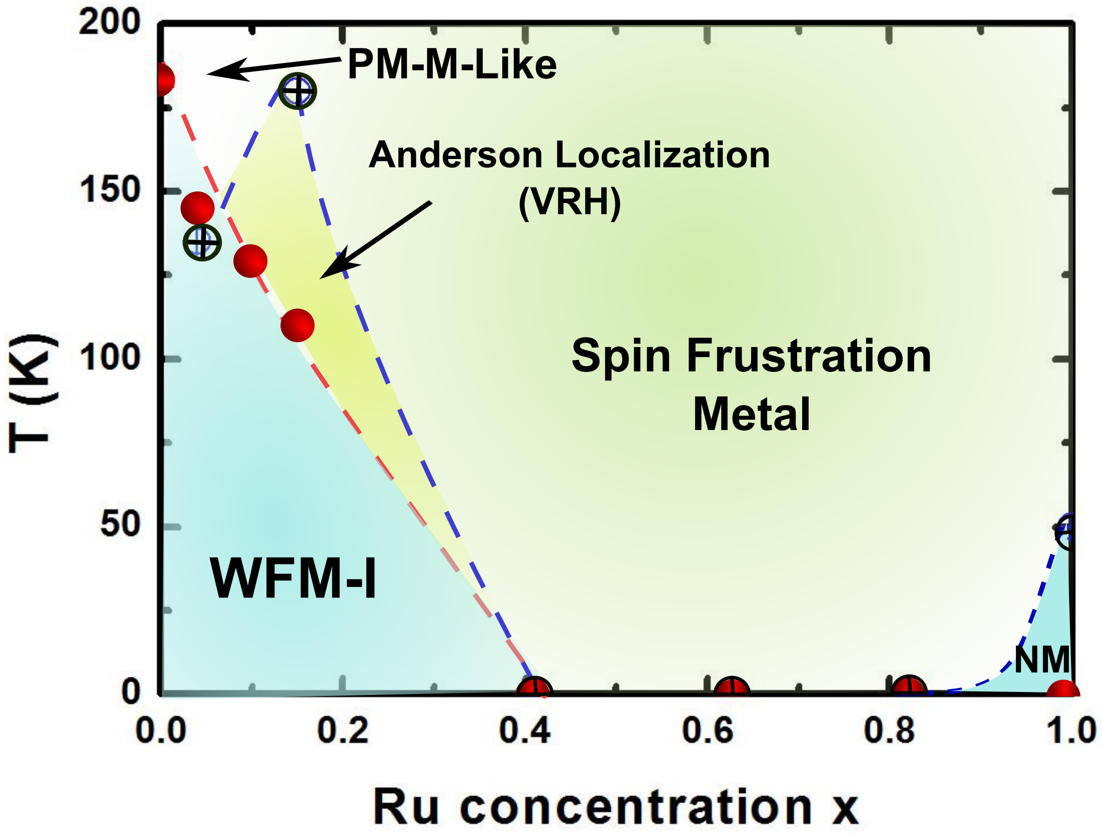

Figure 4.20: The phase diagram of the $BaIr_{1-x}Ru_xO_3$ system; WFM-I means weak ferromagnetic insulating state, VRH is variable range hoping, PM-M-Like is paramagnet metallic-like state, and I means insulating state. The red and black circles are data points.

4.6 $\mathbf{BaIr_{1\text{-}x}Rh_xO_3}$ System

The $BaIr_{1-x}Rh_xO_3$ system was made by a systematic chemical substitution for the Ir^{4+} ion by the Rh^{4+} ion. In this system, the investigated range of doping was a low level of concentration of $0 < x < 0.1$. The magnetic, transport, and thermodynamic properties of this system show similar behaviors to the system $BaIr_{1-x}Ru_xO_3$ in some aspects and differences in other aspects. The main difference between the two systems is that the Ru doping is a charge carrier doping, while Rh doping is isoelectronic doping.

4.6.1 Magnetic Properties of $BaIr_{1-x}Rh_xO_3$

The magnetic properties of the $BaIr_{1-x}Rh_xO_3$ system show similar behaviors to those were seen in $BaIr_{1-x}Ru_xO_3$ within the low range of concentration. This means that the Rh doping has an effect on the system similar to that of Ru. The increase of Rh doping, within this range from $x = 0.03$ to $x = 0.10$, systematically suppressed the high temperature magnetic ordering of the parent compound $BaIrO_3$. The transition temperature T_C decreased from 183 K for $x = 0$, to 160 K for the lowest concentration $x = 0.03$, and then down to 110 K for $x = 0.10$, as shown in figures 4.21. The suppression also affected the magnetization M(T) magnitude, where it decreases as x increases. These M(T) measurements were run within the temperature range of 1.7 K to 300 K. The main features and observations as a result of this low level of doping can be summarized in the following points:

- The difference in size of the ionic radius of Ir^{4+} (0.625Å) and Rh^{4+} (0.600Å) affects the $\frac{c}{a}$ ratio of the lattice parameters, which affects the relative strength of the SOI and tetragonal CFE that alters the exchange interactions.

- The Curie-Weiss fitting also gives comparable values for Curie-Weiss temperature (θ_{CW}) and the effective moment (μ_{eff}) to those obtained in the case low level of Ru doping. Here, the Curie-Weiss temperature is also negative and it is -43.75 K for x = 0.10, as shown in the inset of figure (4.21). Compared to the same level of doping of Ru substitution, (θ_{CW}) was -73 K, which indicates that the antiferromagnetic coupling in the $BaIr_{1-x}Rh_xO_3$ system is weaker.

- The very low temperature feature that was observed in the magnetization of $BaIr_{1-x}Ru_xO_3$ is also shown in this system magnetization; it occurs at T < 20 K and for both concentrations, x = 0.03 and x = 0.10.

The isothermal magnetization measurements; figure 4.21, still show very low saturation moment, and also are comparable to those were observed in the case of the Ru doping system. As was the case in the Ru doping system, the influence of increasing the Ru concentration on the competing energies, such as the SOI, the non-cubic CFE, and the Hund's rule coupling, has also enhanced the competition between antiferromagnetic and ferromagnetic couplings, which was reflected in the change of the sign of Curie-Weiss temperature (θ_{CW}) from positive to negative, and also the possibility of realizing a frustration state in the high concentration systems.

4.6.2 Transport Properties of $BaIr_{1-x}Rh_xO_3$

The transport properties of this system are completely different from those of the $BaIr_{1-x}Ru_xO_3$ system. In the $BaIr_{1-x}Rh_xO_3$ system, the Rh doping was not able to switch the ground state of the system to be metallic within this low range of doping. The system has preserved the insulating state along a wide range of temperatures. These resistivity measurements were run from 12 K, the lowest temperature, to 750 K. Within this wide range, there was a small drop in the resistivity values at the high temperatures range, T > 300, as shown in figure (4.22). The resistivity increases slowly as temperature decreases at the high temperature range. At lower temperatures, the resistivity values start to increase faster as temperature decreases. The sharp turn up in the resistivity measurements at lower temperatures occurs at around 100 K for x = 0.055 and at around 150 K for x = 0.10, as shown in figure (4.23). The low temperature range shows higher values for the resistivity, especially

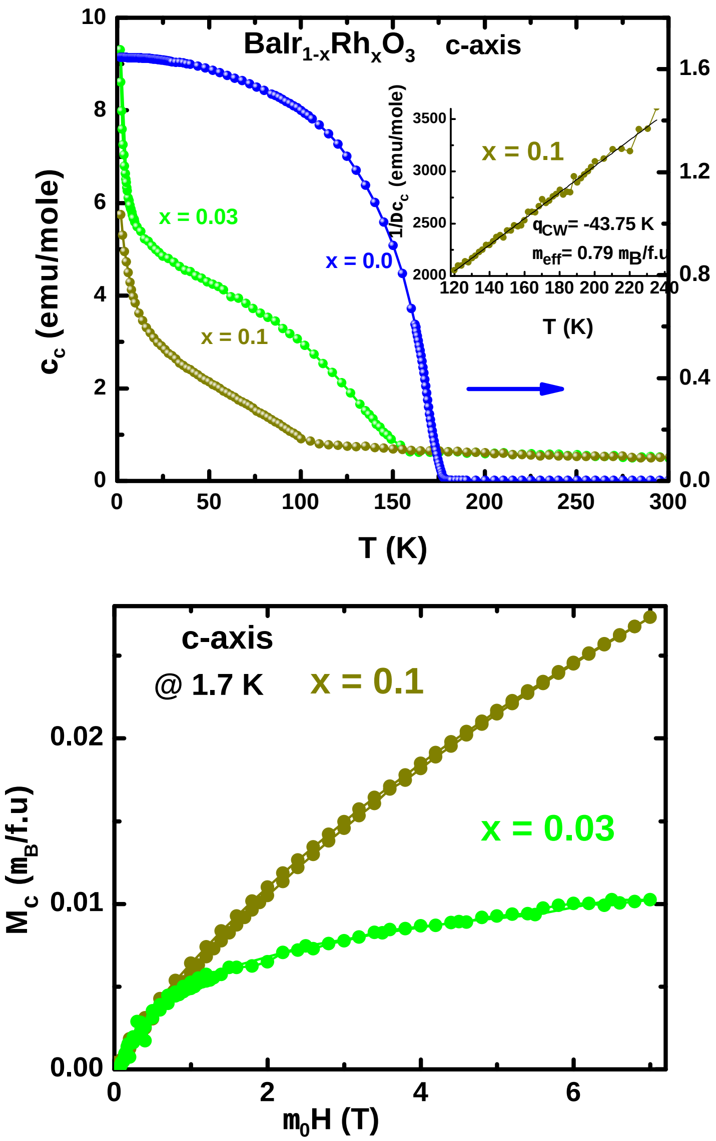

Figure 4.21: The magnetic susceptibility measurements of the low range of doping of the $BaIr_{1-x}Rh_xO_3$ system (upper panel); for x = 0.03 and 0.10, along with parent compound $BaIrO_3$. The inset shows the Curie-Weiss fitting for x = 0.10, with the effective moment μ_{eff} and Curie-Weiss temperaturesθ_{CW} are indicated. The lower panel shows the isothermal magnetization M(H) measurement, at 1.7 K, for the indicated concentrations.

below 100 K for x = 0.055 and below 50 K for x = 0.10. The anisotropy in the resistivity seems to be decreasing as the concentration increases from x = 0.055 to x = 0.10. The activation law fitting gives insulating gap energies of 85 meV for x = 0.055 and 67 meV for x = 0.10, see the inset of the activation law fitting in figure (4.23). Both of these values for the gaps are higher than the value obtained for the parent compound of 46 meV.

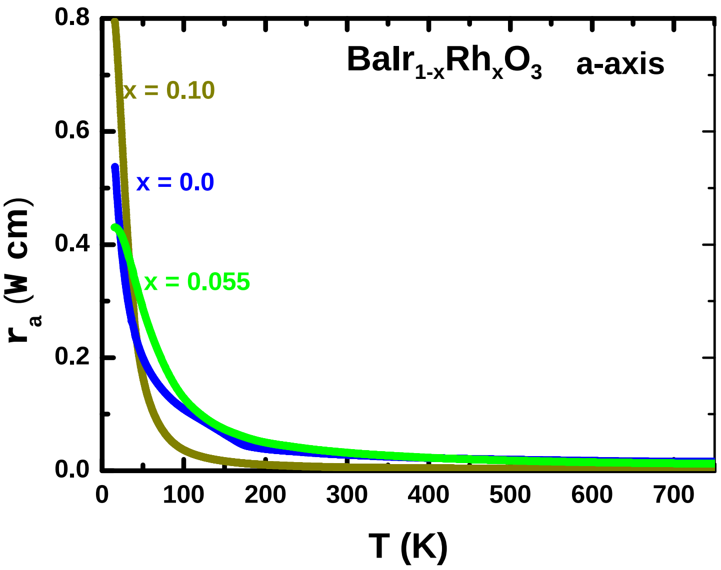

Figure 4.22: A comparison of the electrical resistivity of the low concentrations of doping of the $BaIr_{1-x}Rh_xO_3$ system and the parent compound $BaIrO_3$

The VRH within this low doping level confirms the weak localization state because of Anderson localization. This insulating state is a result of the increasing disorder among the magnetic sites in the system. Figure (4.24) shows the VRH fitting for both concentrations. For a comparison with the other iridates system $Sr_2Ir_{1-x}Rh_xO_4$, which belongs to the RP series $Sr_{n+1}Ir_nO_{3n+1}$. Under the effect of the Rh substitution, the resistivity behavior shows a metallic-like state with very low concentrations of x = 0.07, and a clear metallic state was established at higher concentrations that were still less than x = 0.24. The higher concentrations of x > 0.24 were affected by disorder localization because of the scattered distribution of the Ir/Rh ion in the system. As a result, the higher levels of doping, x > 0.24, retains the insulating state in the system.

4.6.3 Heat Capacity Properties of $BaIr_{1-x}Rh_xO_3$

The heat capacity measurement of the temperature range of 1.8 K to 20 K is shown in figure 4.25. It shows the low temperature dependence of the heat capacity C(T) for the low concentration levels of Rh doping; for x = 0.02, x = 0.055, and x = 0.10 and in addition to the parent compound $BaIrO_3$. The Rh doping effect on the $BaIr_{1-x}Rh_xO_3$ system is very similar to the Ru doping system. The fitting of the heat capacity C(T) data of this low concentration level of doping is shown in the inset of figure 4.25. The fitting to (T ^{3}) behavior has showed an enhancement in the electronic term contribution in the heat capacity. This increase in (γ) reaches 30.6 mJ/mole K^2 for x = 0.055, compared to the small insulating value of 1 mJ/mole K^2 for the parent compound (x =0.0). The lowest concentration has enhanced (γ) of 6.3 mJ/mole K^2 which is comparable to the value found for the lowest concentration in

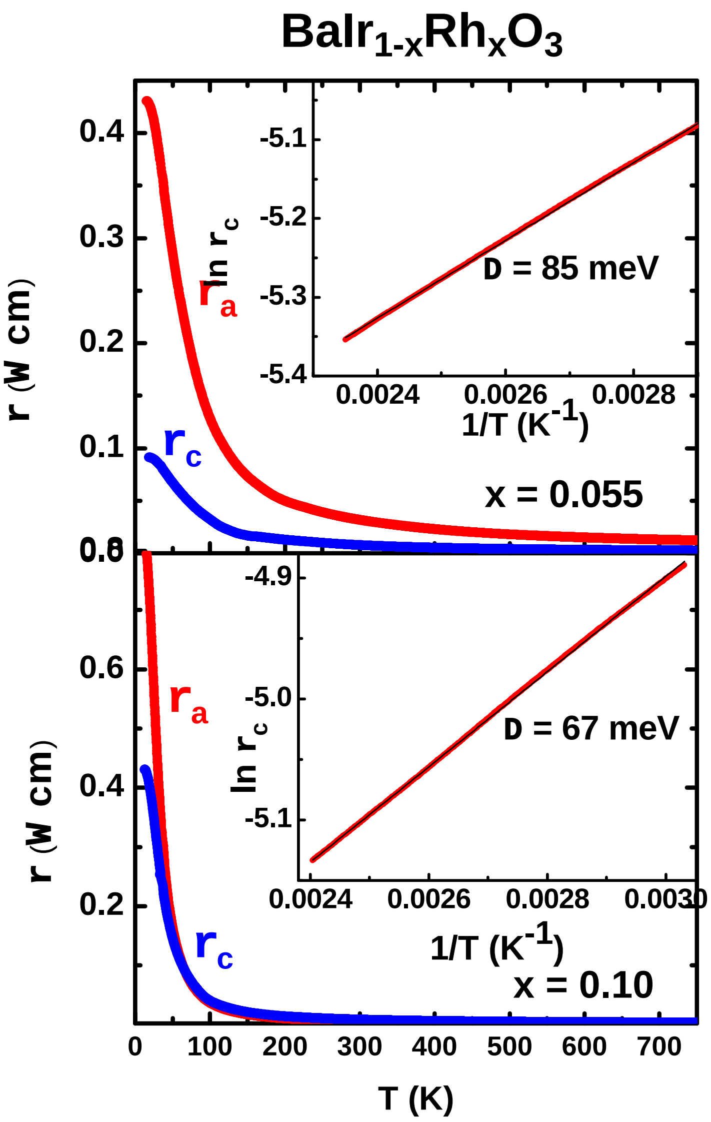

Figure 4.23: The electrical resistivity measurements of the low concentrations of doping of the $BaIr_{1-x}Rh_xO_3$ system; for x = 0, 0.055 (upper panel), 0.10 (lower panel). The insets show the activation energy law fitting with the energy gap values; for x = 0.055 the gap is 85 meV and for x =0.10 it is 67 meV.

the case of $BaIr_{1-x}Ru_xO_3$ system. For x = 0.10 the electronic contribution factor was calculated to be 22.6 mJ/mole K^2.

4.6.4 Thermoelectric Power Properties of $BaIr_{1-x}Rh_xO_3$

It is obvious that the general S(T) behavior of the $BaIr_{1-x}Rh_xO_3$ system is the same as that observed in the $BaIr_{1-x}Ru_xO_3$ system within the low level of doping, as shown in figure (4.26). The S(T) measurements show a metallic behavior, even

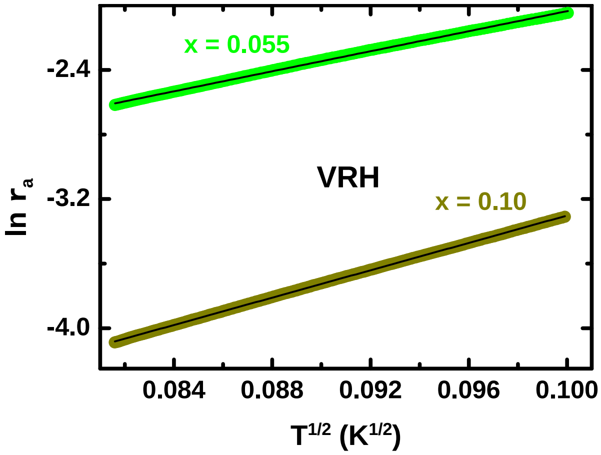

Figure 4.24: The variable range hoping (VRH) fit of the two concentrations; x = 0.055 and x = 0.10 for the $BaIr_{1-x}Rh_xO_3$. It is an evidence of the disorder localization in this system.

though the transport behavior is consistent with an insulating state. As was the case with Ru doped system, the S(T) shows a continuous drop all the way down to 15 K, where S(T) is just a small $\mu V/K$,. The S(T) of x = 0.10 has lower values than those of x = 0.055, which is similar to the other system where the TEP decreases as x increases. In both concentrations, x = 0.055 and x = 0.10, the anisotropy also becomes less differential between the two crystallographic directions and the anisotropy diminishes as x increases. Both a- and c-axis TEP follow the same behavior with a small difference in magnitude of a small $\mu V/K$. These two concentrations show that $S_c(T)$ is always higher than $S_a(T)$ for T < 150 K as illustrated in the upper and lower panels of figure (). The anisotropy in magnitude becomes less and less as temperature decreases. Here, also a small anomaly is shown at the very low temperature.

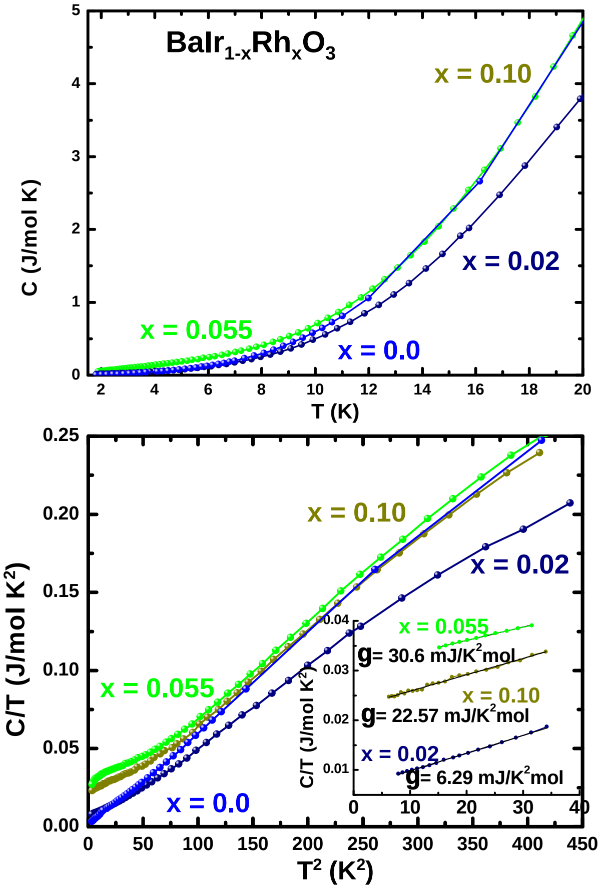

Figure 4.25: The low temperature heat capacity measurements of low concentration of doping of the $BaIr_{1-x}Rh_xO_3$ system. The parent compound $BaIrO_3$ is shown for a comparison.

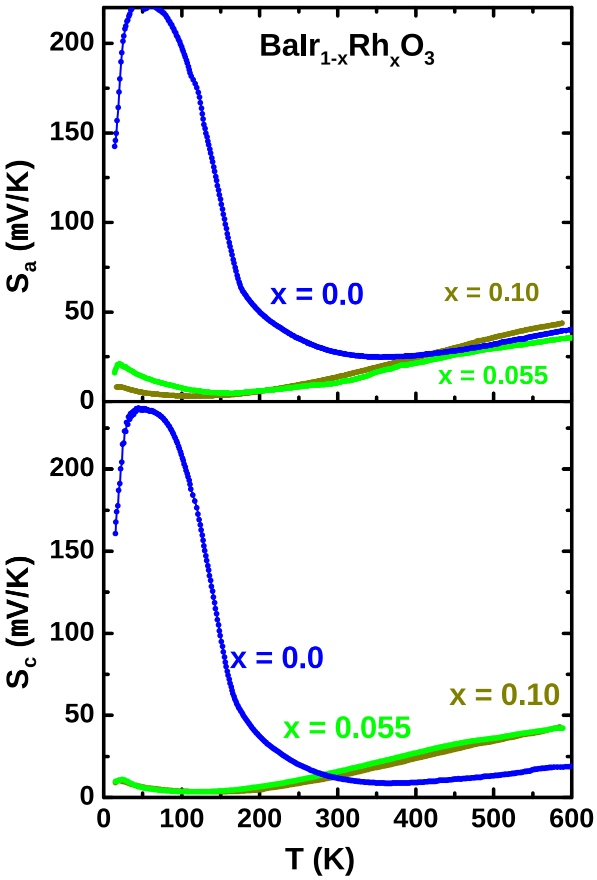

Figure 4.26: The thermoelectric power (TEP) measurements of low concentration of doping of the $BaIr_{1-x}Rh_xO_3$ system. The parent compound $BaIrO_3$ is shown for a comparison. the Upper panel is the a- axis measurements andthe lower panel is the c-axis measurements

Chapter 5 CONCLUDING REMARKS

5.1 Conclusion

In this study, we have applied a number of experimental techniques to investigate the properties of the $BaIrO_3$ system under a systematic chemical substitution of two different magnetic ions; Ru^{4+} in one case and Rh^{4+} in other case for the seek of a comparison. The obtained results reveal the critical dependence of the ground state on the concentration of the doping. These results showed that there are two distinct ranges of doping; the low level of doping for $x < 0.15$ and the higher level of doping for $x > 0.41$. The crystal structure was preserved within these two different ranges, as was confirmed by the x-ray results. The Ru doping has resulted in a systematic change in the lattice parameters and the bonds lengths and angles. The low concentration level of the Ru doping has suppressed the magnetic ordering and derived the system to a metallic-like state. Higher levels of Ru doping clearly have established a true enhanced paramagnet metallic state. The change in the sign of Curie-Weiss temperature θ_{CW} from the positive value 175 K, for the parent compound, to negative values as x increases is an indication of a competition between ferromagnetic (FM) and antiferromagnetic (AFM) exchange interactions in the doped systems. The reduction in the electrical resistivity is a reflection of the weakened of SOI and the reduction in the insulating gap opening. The persistent non-metallic state below 50 K indicates that the insulting gap was reduced, but not fully eliminated. The thermoelectric power measurements of the doped systems clearly support the transport properties, and show the switch from the insulating behavior of the parent compound to a metallic state as x increases.

The other system of the low range of the Rh doping shows very similar behavior in terms of the magnetic properties. The magnetic suppression was also enhanced with the increase of x. The competition between the FM and AFM coupling is also observed in terms of the sign change of Curie-Weiss temperature. The transport properties of the Rh doped system were completely different from those observed in the system of the Ru doping. In the Rh doped system, a persistent insulating state behavior was observed within this low range of doping. This persistent insulating state is a result of the alternate of the magnetic ion sites between Ir and Rh that increases a disorder state in the system. In other words, the insulating state extant in this region is evidently the consequence of Anderson localization, which was confirmed by the variable range hoping fitting for the low temperature resistivity measurements. On the other hand, the TEP measurement for this system was shown a similar behavior to that observed in the Ru doping case, even though their transport behaviors are different within this low level of doping. The TEP behavior of the Rh doped system is very consistent with a metallic behavior; TEP decreases as temperature decrases. In summary, tuning the composition of $BaIr_{1-x}M_xO_3$ (M = Ru or Rh), within the low range of doping, has a direct control over the electronic state of the system. In the case of Ru doping, the metallic-like state was switch to an insulating behavior at low temperature range, and the magnetic order suppression increases as x increases. In the case of the Rh low concentration doping, there was an energy level mismatch between the Rh and Ir sites, which makes the hopping of the charge carriers between an octahedron containing a Rh ion and one with an Ir ion more difficult as x increases. The random distribution of the Rh and Ir ions gives a rise to the Anderson localization that establishes an insulating state.

5.2 Remarks

Indeed TMOs are still a fertile area for interesting research and discoveries. The interesting properties and characteristics of TMOs are attributed to the interactions between the d-electrons with their host environment. In 4d and 5d TMOs, there is a competition between the electron degrees of freedom that control the resulting ground state. The interactions include (e-e) Coulomb interaction, spin-spin interaction, crystal field effect, and spin-orbit interaction. Iridates, as a class of heavy TMOs, do not support the conventional picture of strongly correlated electron systems, because of the comparable scale of the different interaction energies that set a new balance for these energies. This new balance of competing energies is the key in understanding many of exotic properties of perovskite iridates. $BaIrO_3$ is classified as a spin-orbit interaction induced Mott insulator [24]. The influence of the SOI, on the system's ground stste, is strongly related to other interactions and degrees of freedom, and also to the detailed band structure around the Fermi surface E_F [72] [73].

The interplay between electronic, orbital, and lattice degrees of freedom continues to be of a wide interest and attraction. The new balance of the related energies in iridates has opened a new direction in this field, i.e., SOI degree of freedom. A number of projects in our lab, as well as in other places around the world, have been conducting for shading more light on this area of 5d heavy TMOs and the physics of spin-orbit interaction in these materials. The current studies in our lab fall into two directions; one is the synthesis of new iridium based compounds, include oxides and chalcogenides etc.. The other direction is to extend the chemical doping to include other different chemical elements in different sites of the structure. The later strategy is directed to conduct conclusive studies about the interaction and physics of 3d-4d, 3d-5d, and 4d-5d heavy TMOs.

At this point, the iridates' journey is already started and there are many questions and concerns need to be addressed. 5d heavy TMOs, and specifically iridates, are promising area for excitement in physics and discovery.

Bibliography

[1] P. A. Cox, *Transition Metal Oxides: An Introduction to their Electronic Structure and Properties.* International Series of Monographs on Chemistry, Oxford University Press, reprint ed., June 1995.

[2] M. Nic, J. Jirat, and B. Kosata, eds., *Compendium of Chemical Terminology.* International Union of Pure and Applied Chemistry (IUPAC), 2006.

[3] T. H. Geballe and J. K. Hulm, "Superconductivity – the state that came in from the cold," *Science*, vol. 239, no. 4838, pp. 367–375, 1988.

[4] R. Pazik, D. Kaczorowski, D. Hreniak, W. Strek, and W. Lojkowski, "Synthesis, structure and magnetic properties of $BaTiO_3$ nanoceramics," *Chemical Physics Letters*, vol. 452, pp. 144–147, 2008.

[5] J. B. Goodenough, "Metallic oxides," *Progress in Solid State Chemistry*, vol. 5, p. 145, 1971.

[6] M. Shepard, S. McCall, G. Cao, and J. E. Crow, "Thermodynamic properties of perovskite $AMnO_{3-x}$, ($A =$ Ca, Sr, and Ba) single crystals," *Journal of Applied Physics*, vol. 81, 1997.

[7] M. C. Shapiro, S. C. Riggs, M. B. Stone, C. R. de la Cruz, S. Chi, A. A. Podlesnyak, and I. R. Fisher, "Structure and magnetic properties of the pyrochlore iridate $Y_2Ir_2O_7$," *Phys. Rev. B*, vol. 85, p. 214434, 2012.

[8] O. Chauvet, L. Forro, I. Kos, and M. Miljak, "Magnetic properties of the anatase phase of TiO_2," *Solid State Communications*, vol. 93, pp. 667–669, 1995.

[9] G. Kotliar and D. Vollhardt, "Strongly correlated materials: Insights from dynamical mean-field theory.," *Physics Today*, vol. 57, no. 3, pp. 53 – 59, 2004.

[10] A. Sutton, *Electronic Structure of Materials.* Oxford Science Publications, Clarendon Press, illustrated, reprint ed., 1993.

[11] Y. Tokura, "Correlated electrons: Science to technology," *JSAP International*, vol. 2, p. 12, 2000.

[12] N. W. Ashcroft and N. D. Mermin, *Solid State Physics.* Science: Physics, Brooks Cole, 1 ed., January 1976.

[13] S. Blundell, *Magnetism in Condensed Matter*, vol. 4 of *Oxford master series in condensed matter physics.* Oxford University Press, Dec. 2001.

[14] O. Korneta, *A systematic study of transport, magnetic, and thermal properties of layered Iridates.* PhD thesis, University of Kentucky, 2012.

[15] C. N. R. Rao and B. Raveau, *Transition Metal Oxides: Structure, Properties, and Synthesis of Ceramic Oxides.* John Wiley & Sons, 2nd ed., 1998.

[16] G. Cao, J. Crow, R. Guertin, P. Henning, C. Homes, M. Strongin, D. Basov, and E. Lochner, "Charge density wave formation accompanying ferromagnetic ordering in quasi-one-dimensional $BaIrO_3$," *Solid State Commun.*, vol. 113, no. 11, pp. 657 – 662, 2000.

[17] G. Cao, J. Bolivar, S. McCall, J. E. Crow, and R. P. Guertin, "Weak ferromagnetism, metal-to-nonmetal transition, and negative differential resistivity in single-crystal Sr_2IrO_4," *Phys. Rev. B*, vol. 57, pp. R11039–R11042, May 1998.

[18] G. Cao, V. Durairaj, S. Chikara, D. E. De Long, S. Parkin, and P. Schlottmann, "Non-fermi-liquid behavior in nearly ferromagnetic $SrIrO_3$ single crystals," *Phys. Rev. B*, vol. 76, p. 100402, 2007.

[19] G. Cao, Y. Xin, C. S. Alexander, J. E. Crow, P. Schlottmann, M. K. Crawford, R. L. Harlow, and W. Marshall, "Anomalous magnetic and transport behavior in the magnetic insulator $Sr_3Ir_2O_7$," *Phys. Rev. B*, vol. 66, p. 214412, Dec 2002.

[20] A. Powell, P. Battle, and J. Gore, "Structure of Sr_4IrO_6 by time-of-flight neutron powder diffraction," *Acta Crystallographica*, vol. C49, pp. 852–854, 1993.

[21] S. Zhao, J. M. Mackie, D. E. MacLaughlin, O. O. Bernal, J. J. Ishikawa, Y. Ohta, and S. Nakatsuji, "Magnetic transition, long-range order, and moment fluctuations in the pyrochlore iridate $eu_2ir_2o_7$," *Phys. Rev. B*, vol. 83, p. 180402, 2011.

[22] Y. Singh and P. Gegenwart, "Antiferromagnetic mott insulating state in single crystals of the honeycomb lattice material na_2iro_3," *Phys. Rev. B*, vol. 82, p. 064412, 2010.

[23] S. N. Ruddlesden and P. Popper, "New compounds of the K_2NiF_4 type," *Acta Crystallographica*, vol. 10, pp. 538–539, Aug 1957.

[24] S. Chikara, O. Korneta, W. P. Crummett, L. E. DeLong, P. Schlottmann, and G. Cao, "Giant magnetoelectric effect in the $J_{\mathrm{eff}} = \frac{1}{2}$ Mott insulator Sr_2IrO_4," *Phys. Rev. B*, vol. 80, p. 140407, Oct 2009.

[25] G. Cao and L. Delong, eds., *Frontiers of 4d- and 5d-Transition Metal Oxides.* World Scientific, 2013.

[26] C. Kittel, *Introduction to solid state physics.* Wiley, 7th ed., 1996.

[27] B. Pamplin, *Crystal growth*, vol. 16 of *International series on the science of the solid state.* Pergamon Press, 2nd ed., 1980.

[28] C. Hammond, *The basics of crystallography and diffraction.* IUCr texts on crystallography, Oxford University Press, 3 ed., June 2009.

[29] D. Brandon and W. Kaplan, *Microstructural Characterization of Materials.* Quantitative software engineering series, John Wiley & Sons, 2008.

[30] Scintag Inc. USA, Cupertino, CA 95014, *Scintag X1. Technical Manual*, 1999.

[31] c. Noce, A. Veechione, M. Cuoco, and A. Romano, eds., *Ruthenate and Rutheno-Cuprate Materials.* Springer, 2003.

[32] L. Lévy, *Magnetism and superconductivity.* Texts and monographs in physics, Springer, 2000.

[33] H. Kramers, "L'interaction entre les atomes magnétogènes dans un cristal paramagnétique," *Physica*, vol. 1, pp. 182 – 192, 1934.

[34] J. Kanamori, "Superexchange interaction and symmetry properties of electron orbitals," *J. Phys. Chem. Solids*, vol. 10, pp. 87–98, July 1959.

[35] T. N. Casselman and F. Keffer, "Right-angled superexchange," *Phys. Rev. Lett.*, vol. 4, pp. 498–500, May 1960.

[36] N. F. Mott, "The basis of the electron theory of metals, with special reference to the transition metals," *Proceedings of the Physical Society. Section A*, vol. 62, no. 7, p. 416, 1949.

[37] K. M. Shen and J. S. Davis, "Cuprate high-T_C superconductors," *Materials Today*, vol. 11, no. 9, pp. 14 – 21, 2008.

[38] P. W. Anderson, "Absence of diffusion in certain random lattices," *Phys. Rev.*, vol. 109, pp. 1492–1505, Mar 1958.

[39] P. W. Anderson, "Localized magnetic states in metals," *Phys. Rev.*, vol. 124, pp. 41–53, Oct 1961.

[40] J. C. Slater, "Magnetic effects and the hartree-fock equation," *Phys. Rev.*, vol. 82, pp. 538–541, May 1951.

[41] F. Gebhard, *The Mott metal-insulator transition: models and methods*, vol. 137 of *Springer Tracts in Modern Physics.* Springer, illustrated ed., 1997.

[42] J. Hubbard, "Electron correlations in narrow energy bands," *Proceedings of the Royal Society of London. Series A. Mathematical and Physical Sciences*, vol. 276, no. 1365, pp. 238–257, 1963.

[43] P. Bhattacharya, R. Fornari, and H. Kamimura, eds., *Comprehensive Semiconductor Science and Technology, Volume 1.* Elsevier, 2011.

[44] D. Smith and R. Jenkins, "The powder diffraction file: Past, present, and future," *J. Res. Natl. Inst. Stand. Technol.*, vol. 101, pp. 259–271, May 1996.

[45] S. Parkin and H. Hope, "Macromolecular cryocrystallography: Cooling, mounting, storage and transportation of crystals," *J. Appl. Crystallogr.*, vol. 31, pp. 945–953, Dec 1998.

[46] Hampton Research, Aliso Viejo, CA 92656-3317 U.S.A., *Paratone-N User Guide/Certificate of Analysis*, 2008.

[47] G. M. Sheldrick, "A short history of SHELX," *Acta Cryst. A*, vol. 64, pp. 112–122, Jan 2008.

[48] G. M. Sheldrick, "SADABS. version 2.03," 1996. University of Göttingen, Germany.

[49] J. Goldstein, ed., *Scanning electron microscopy and X-ray microanalysis: a text for biologists, materials scientists, and geologists.* New York: Plenum Press, 2nd ed., 1981.

[50] K. H. J. Buschow, ed., *Concise Encyclopedia of Magnetic and Superconducting Materials.* Elsevier Science, 2nd ed., March 2006.

[51] Quantum Design, San Diego, CA, *Magnetic Property Measurement System MPMS XL. Hardware Reference Manual.*, 2000.

[52] M. Tinkham, *Introduction to Superconductivity.* Krieger Pub Co, 1975.

[53] F. Bassani, G. L. Liedl, and P. Wyder, eds., *Encyclopedia Dictionary of Condensed Matter Physic*, vol. I. Academic Press, September 2005.

[54] E. du Trémolet de Lacheisserie, D. Gignoux, and M. Schlenker, eds., *Magnetism: Materials and applications*, vol. II. Springer, 1st ed., October 2004.

[55] D. R. Lide, ed., *CRC handbook of chemistry and physics: a ready-reference book of chemical and physical data.* CRC Handbook of Chemistry and Physics, CRC Press, 85th ed., 2004.

[56] "7031 varnish (phenolic butvar resin)." Material Safety Data Sheet, General Electric Co. Schenectady, NY, 1985.

[57] "EPO-TEK® H20E." Material Safety Data Sheet, Epoxy Technology Inc., Billerica, MA, September 2010.

[58] "Dotite XC-12 (carbon containing conductive paste)." Material Safety Data Sheet, Fujikura Kasei Co. Ltd., Tokyo, Japan, 2010.

[59] "Ceramabond™ 865 (high-temperature ceramic adhesive)." Aremco Products Inc., Valley Cottage, NY. Material Safety Data Sheet, February 2009.

[60] Linear Research Inc., San Diego, CA, *LR-700 AC Resistance Bridge User's Manual*, v1.3 ed., 1996.

[61] Keithley Instruments, Inc., Cleveland, OH, *Model 6220 DC Current Source. Reference Manual*, June 2005.

[62] Advanced Research Systems, Allentown, PA, *DE202 Technical manual*, 2003.

[63] Lake Shore Cryotronics, Inc., Westerville, Ohio, USA, *Lake Shore Model 331 temperature controller. Users manual.*, 1.9 ed., May 2009.

[64] Quantum Design, San Diego, CA, *Physical Property Measurement System PPMS. Hardware Reference Manual.*, 3rd ed., 2000.

[65] J. S. Hwang, K. J. Lin, and C. Tien, "Measurement of heat capacity by fitting the whole temperature response of a heat-pulse calorimeter," *Rev. Sci. Instrum.*, vol. 68, pp. 94 – 101, June 1997.

[66] "Apiezon® N, cryogenic high vacuum grease." Technical Data Sheet, M&I Materials, Manchester, United Kingdom, August 2005.

[67] "Apiezon® H, high temperature vacuum grease." Technical Data Sheet, M&I Materials, Manchester, United Kingdom, August 2005.

[68] J. J. Randall and R. Ward, "The preparation of some ternary oxides of the platinum metals," *J. Am. Chem. Soc.*, vol. 81, no. 11, pp. 2629–2631, 1959.

[69] J. G. Dickson, L. Katz, and R. Ward, "Compounds with the hexagonal barium titanate structure," *J. Am. Chem. Soc.*, vol. 83, no. 14, pp. 3026–3029, 1961.

[70] P. Donohue, L. Katz, and R. Ward, "The modification of structures of ternary oxides by cation substitution. ii. substitution of various cations for ruthenium in barium ruthenium oxide," *Inorg. Chem.*, vol. 5, no. 3, pp. 339–342, 1966.

[71] B. J. Kim, H. Jin, S. J. Moon, J.-Y. Kim, B.-G. Park, C. S. Leem, J. Yu, T. W. Noh, C. Kim, S.-J. Oh, J.-H. Park, V. Durairaj, G. Cao, and E. Rotenberg, "Novel $J_{\text{eff}} = 1/2$ Mott state induced by relativistic spin-orbit coupling in Sr_2IrO_4," *Phys. Rev. Lett.*, vol. 101, p. 076402, Aug 2008.

[72] G. Jackeli and G. Khaliullin, "Mott insulators in the strong spin-orbit coupling limit: From Heisenberg to a Quantum Compass and Kitaev models," *Phys. Rev. Lett.*, vol. 102, p. 017205, Jan 2009.

[73] F. Ye, S. Chi, B. C. Chakoumakos, J. A. Fernandez-Baca, T. Qi, and G. Cao, "The magnetic and crystal structures of Sr_2IrO_4: A neutron diffraction study," *arXiv(1302.2890)*, 2013.

[74] T. F. Qi, O. B. Korneta, L. Li, K. Butrouna, V. S. Cao, X. Wan, P. Pchlottmann, R. K. Kaul, and G. Cao, "Spin-orbit tuned metal-isulator transition in single-crystal $Sr_2Ir_{1-x}Rh_xO_4$ ($0 \leq x \leq 1$)," *Phys. Rev. B*, vol. 86, p. 125105, 2012.

[75] O. B. Korneta, S. Chikara, S. Parkin, L. E. De Long, P. Schlottmann, and G. Cao, "Pressure-induced insulating state in $Ba_{1-x}R_xIrO_3$ (r=gd,eu) single crystals," *Phys. Rev. B*, vol. 81, p. 045101, 2010.

[76] A. Powell and P. Battle, "A time-of-flight powder neutron diffraction study of non-stoichiometry in barium iridate $BaIrO_{3-\delta}$," *J. Alloys Compd.*, vol. 232, no. 1-2, pp. 147 – 153, 1996.

[77] B. Chamberland, "A study on the $BaIrO_3$ system," *Journal of the Less Common Metals*, vol. 171, no. 2, pp. 377 – 394, 1991.

[78] J.-G. Cheng, J. A. Alonso, E. Suard, J.-S. Zhou, and J. B. Goodenough, "A new perovskite polytype in the high-pressure sequence of $BaIrO_3$," *J. Am. Chem. Soc.*, vol. 131, no. 21, pp. 7461–7469, 2009.

[79] J. Zhao, L. Yang, Y. Yu, F. Li, R. Yu, and C. Jin, "Structural and physical properties of the 6M $BaIrO_3$: A new metallic iridate synthesized under high pressure," *Inorg. Chem.*, vol. 48, no. 10, pp. 4290–4294, 2009.

[80] M. L. Brooks, S. J. Blundell, T. Lancaster, W. Hayes, F. L. Pratt, P. P. C. Frampton, and P. D. Battle, "Unconventional magnetic properties of the weakly ferromagnetic metal $BaIO_3$," *Phys. Rev. B*, vol. 71, p. 220411, Jun 2005.

[81] M. A. Laguna-Marco, D. Haskel, N. Souza-Neto, J. C. Lang, V. V. Krishnamurthy, S. Chikara, G. Cao, and M. van Veenendaal, "Orbital magnetism and spin-orbit effects in the electronic structure of $BaIrO_3$," *Phys. Rev. Lett.*, vol. 105, p. 216407, Nov 2010.

[82] J. T. Rijssenbeek, R. Jin, Y. Zadorozhny, Y. Liu, B. Batlogg, and R. J. Cava, "Electrical and magnetic properties of the two crystallographic forms of $BaRuO_3$," *Physical Review B: Condensed Matter and Materials Physics*, vol. 59, p. 4561, 1999.

[83] K. Maiti, R. S. Singh, V. R. R. Medicherla, S. Rayaprol, and E. V. Sampathkumaran, "Origin of charge density wave formation in insulators from a high resolution photoemission study of $BaIrO_3$," *Phys. Rev. Lett.*, vol. 95, p. 016404, Jun 2005.

[84] R. P. W. Scott, *Thermal Analysis.* Physical Chemistry Resources, Library4science LLC, 2003. http://physicalchemistryresources.com.

[85] D. Lowndes, L. Finegold, R. N. Rogers, and B. Morosin, "Specific heat of three magnetic linear-chain antiferromagnets," *Phys. Rev.*, vol. 186, pp. 515–521, Oct. 1969.

[86] H. Watanabe, T. Shirakawa, and S. Yunoki, "Microscopic study of a spin-orbit-induced mott insulator in ir oxides," *Phys. Rev. Lett.*, vol. 105, p. 216410, 2010.

VITA

KAMAL H. BUTROUNA.

Contact Information

Department of Physics and Astronomy
177 Chemistry-Physics Building
University of Kentucky
505 Rose Street
Lexington, Kentucky 40506 USA
Tel.: (859) 218-1297
Email: kamal.but@uky.edu

Education

- Doctoral degree in experimental condensed matter physics,
  University of Kentucky (Spring 2014)
  Thesis title: A Systematic Transport and Thermodynamic Study of Heavy Transition Metal Oxides with Hexagonal Structure
  Co-Directors: Dr. Gang Cao and Dr. Lance DeLong

- Master of Science degree in physics - experimental condensed matter physics,
  University of Kentucky (Spring 2012)
  Qualification Talk: Drastic Impact of Sr Substitution on The Exotic Insulating state in single-crystal $BaIrO_3$: The Magnetic and Physical Properties.
  Supervisor: Dr. Gang Cao

- Master of Science degree in physics - laser material processing,
  University of Tripoli (Spring 2001)
  Thesis title: Composite Formation on Surfaces of Hypereutectic Al-Si Alloys by SiC and Cr Using Ruby Laser.
  Co-Directors: Dr. Madani Dakhil and Dr. Kamal Salib

- Bachelor of Science degree in physics, University of Tripoli (spring 1992)

Employment

- 1995-1999 Research Assistant at Post Graduate Center for Electro-Optics, (Tripoli-Libya).

- 1999-2000 Research Assistant at Renewable Energy and Water Desalination Research Center (Tripoli- Libya).

- 2000-2003 Teaching Assistant, University of Tripoli (Tripoli – Libya).

- 2003-2007 Instructor of Physics at Aljabel Algharbi University (Garian- Libya).

- 2008-current Graduate student of physics – experimental condensed matter physics - at University of Kentucky (Lexington, KY).

- 2013 Research Assistant, in Dr. Cao's group University of Kentucky (Lexington, KY).

- Fall 2013-Spring 2014 Teaching Assistant, Department of Physics and Astronomy, University of Kentucky (Lexington, KY).

Professional and Qualifications Certificates:

- Certificate on operation of high power Nd:YAG lasers from Post Graduate Center for Electro-Optics, (Tripoli- Libya)-1996.

- Certificate on design and print of Textbooks from the National Board of Research and Development (Tripoli- Libya)-2002.

- Certificate of Completion of the workshop on magnetic structure determination from neutron diffraction data, Neutron Science, Oak Ridge National Lab September 17-20, 2012.

Computer Skills:

- Programming with C++, FORTRAN, and LabView (intermediate)

- Microsoft Office, Corel Draw, and Photoshop, Ink Scape, Origin, teXstudio.

Lab Skills:

- Operation and maintenance of high power Nd:YAG laser systems.

- Use of Quantum Design (QD) Instruments (PPMS and MPMS) for magnetic, thermal and transportation measurements. Also the thermogravimetric analyzer (TGA), Advanced Research Systems (ARS) closed cycle cryocooler with high temperature station interface.
  Sample characterization: XRD, EDX, TEM.

- Making Samples: Casting alloys (vertical Furnaces), polycrystals (solid state reaction) and single-crystals using optical floating zone furnace.

Scholarships

- 2008-2012 Scholarship from the ministry of higher education in Libya, for a doctoral degree in USA

Publications

- K. Z. Salib, M. A. Dakhil, M. M. Rakhes, K. H. Butrouna, and A. M. Wahra, "Improving the wear resistance of Al-12%Si alloy by laser-assisted impregnation with SiC particles", 4th Arab Congress on Material Science (ACMS-IV), Tripoli-Libya, 26-28 September 2005.

- T. F. Qi, O. B. Korneta, L. Li, K. Butrouna, V. S. Cao, X. Wan, P. Schlottmann, R. K. Kaul, and G. Cao, “Spin-orbit tuned metal-insulator transitions in single-crystal $Sr_2Ir_{1-x}Rh - xO_4$ (0 < x < 1)”, Physical Review B, volume,86, pp 125105, 2012.

- L. Li, T.F. Qi, L. S. Lin, X. X. Wu, X. T. Zhang, K. Butrouna, V. S. Cao, Y. H. Zhang, Jiangping Hu, P. Schlottmann, L. E. Delong, G.Cao, " superconductivity and strong on-Fermi-liquid behaviour in single-crystal Ir_3Te_8", arXiv:1301.4135v2, 2013.

Professional Membership

- 2008-current Member of America Physical Society (APS)
- 2012-current Member of American Solar Energy Society (ASES).

Interests

- Reading: History, International Cultures, fiction
- Sports: Soccer, biking, hiking.